DISSERTATION

LANDSLIDE RESPONSE TO CLIMATE CHANGE IN DENALI NATIONAL PARK, ALASKA, AND OTHER PERMAFROST REGIONS

Submitted by

Annette Patton

Department of Geosciences

In partial fulfillment of the requirements

For the Degree of Doctor of Philosophy

Colorado State University

Fort Collins, Colorado

Summer 2019

Doctoral Committee:

Advisor: Sara Rathburn

Ellen Wohl
John Singleton
Jeffrey Niemann

ABSTRACT

LANDSLIDE RESPONSE TO CLIMATE CHANGE IN DENALI NATIONAL PARK, ALASKA, AND OTHER PERMAFROST REGIONS

Rapid permafrost thaw in the high-latitude and high-elevation areas increases hillslope susceptibility to landsliding by altering geotechnical properties of hillslope materials, including reduced cohesion and increased hydraulic connectivity. The overarching goal of this study is to improve the understanding of geomorphic controls on landslide initiation at high latitudes.

In this dissertation, I present a literature review, surficial mapping and a landslide inventory, and site-specific landslide monitoring to evaluate landslide processes in permafrost regions. Following an introduction to landslides in permafrost regions (Chapter 1), the second chapter synthesizes the fundamental processes that will increase landslide frequency and magnitude in permafrost regions in the coming decades with observational and analytical studies that document landslide regimes in high latitudes and elevations. In Chapter 2, I synthesize the available literature to address five questions of practical importance, which can be used to evaluate fundamental knowledge of landslide processes and inform land management decisions to mitigate geohazards and environmental impacts. I also evaluate potential implications of increased landslide activity on local nutrient and sediment connectivity, atmospheric carbon feedbacks, and hazards to people and infrastructure. Based on the existing literature, I conclude that after permafrost thaws, landslides will be driven primarily by atmospheric input of moisture and freeze-thaw fracturing rather than responding to disconnected and perched groundwater, melting permafrost ice, and a plane of weakness between ground ice and the active layer. The

transition between perennially frozen and seasonally thawed equilibrium states is likely to increase landslide frequency and magnitude, alter dominant failure styles, and mobilize carbon over timescales ranging from seasons to centuries. While a substantial body of literature exists on case studies of landslides in permafrost regions, no extensive review exists as a compilation of previous work. Last, I suggest three key areas for future research to produce primary data and analysis that will fill gaps in the existing understanding of landslide regimes in permafrost regions. These suggestions include 1) expand the geographic extent of English-language research on landslides in permafrost; 2) maintain or initiate long-term monitoring projects and aerial data collection; and 3) quantify the net effect on the terrestrial carbon budget.

As described in Chapter 3, I conducted surficial geologic mapping and a comprehensive landslide inventory of the Denali National Park road corridor to identify geomorphic controls on landslide initiation in the Alaska Range, which include lithology, slope angle, and thawing ice-rich permafrost. Landslides occur on all slope aspects, primarily at high elevations (>1050 m) where topographic relief is greatest. The majority (84%) of inventoried landslides are < 1 km^2 in area and occurred most frequently on slopes with a bimodal distribution of slope angles, with peaks at ~18° and 28°. A disproportionate number of landslides occurred in unconsolidated sediments (glacial deposits and relict landslide deposits) and in felsic volcanic rocks. Weathering of feldspar within volcanic rocks and subsequent interactions with groundwater produced clay minerals. The presence of clay minerals may promote landslide initiation by impeding groundwater conductivity and reducing rock shear strength. I also found that landslides preferentially initiated within permafrost, where modeled mean decadal ground temperature is approximately -0.2 °C and active layer thickness is approximately 1 m. Landslides that initiated within permafrost occurred on slope angles ~7° lower than landslides on seasonally thawed

hillslopes. Shallow-angle landslides (<20° slopes) in permafrost demonstrate that permafrost/ice thaw is an important triggering mechanism in the study region. Melting permafrost reduces shear strength by lowering cohesion and friction values along ice boundaries. Increased permafrost degradation associated with climate change will make this and other high-relief areas more susceptible to shallow-angle landslides.

The fourth chapter documents the development of landslides in rapidly thawing permafrost regions. To evaluate the impact of landslide age, morphology, and permafrost condition on landslide development, I conducted repeat terrestrial laser scan (TLS) surveys of three shallow-angle landslides that initiated in discontinuous permafrost in Denali National Park, including two landslides that initiated in the last 3 years (Stony Pass Slide and Ptarmigan Active Layer Detachment), and one landslide that initiated 20-50 years ago (Eielson Active Layer Detachment). I used Geomorphic Change Detection to quantify topographic deformation over a one-year study period. I also measured depth to permafrost at the Stony Pass Slide and used 2D ground-penetrating radar (GPR) to identify the permafrost surface in the landslide and adjacent undisturbed slopes. TLS differencing indicates that the two young landslides are still mobile, with maximum elevation loss of 0.8 m and 1.0 m at the landslide scarps, respectively. The older landslide appears topographically stable, which indicates that shallow-angle landslides achieved stability within several decades under previous climate conditions. Visual analysis of GPR data and measured depth to permafrost indicate that permafrost is present at 0.4-1.9 m depth in the undisturbed portions of the slope adjacent to the Stony Pass landslide. No permafrost was measured within the interior of the landslide, however. I interpret the results to suggest initial landslide failure over shallow, thawing permafrost. The observed lack of identifiable permafrost within the slide area therefore indicates that permafrost has thawed faster within the landslide

than within undisturbed portions of the hillslope, which is consistent with ground surface disturbance increasing heat flux from the atmosphere to the subsurface. I postulate that a positive feedback loop exists between permafrost thaw and landslide development.

ACKNOWLEDGEMENTS

One of the most humbling aspects of completing this dissertation is the fact that this project has confronted me with the reality that I have to ask for help. Despite the frequent use of the word "I" throughout this dissertation, my research, like any good science, relied upon the support and collaboration of numerous others. I would like to thank all of those who have helped me complete this research through emotional, physical, or analytic support.

First, I thank you to my advisor Sara. Sara has gone above and beyond the call of professional advising and has mentored me through both academic and personal hurdles. She pushed me when I needed it, encouraged me when my confidence flagged, advised me when I was out of my depth, listened when I had something to say, and always left her door open. Sara, you have helped me grow as a scientist and as a citizen of our world. I am so grateful for the opportunity to learn from you and with you. Thank you.

Thank you also to my committee, who pushed me to learn and grow. Ellen Wohl, John Singleton, and Jeffrey Niemann, you have provided valuable and insightful feedback throughout this project. I am so grateful for your enthusiastic support and your expertise. Thank you to Dan McGrath, the GPR expert who shared his knowledge and his sweat to measure permafrost depth and process the GPR data discussed in Chapter 4.

Thank you to Denny Capps, Denali National Park and Preserve geology whiz and the person who allowed this project to happen at all. Thank you for your logistic support, your time, and your thoughtful discussion. I sincerely hope that these results will prove useful to you and your colleagues in Denali. I would also like to thank several other park staff and geoscientists at DNP, CSU, and the USGS who have provided technical support or contributed to the major ideas

expressed in this paper, including Michael Frothingham, Cal Ruleman, Mauro Soldati and an anonymous reviewer at Geomorphology, Russell Rosenberg, Nick Virgil, Sawyer Finley, Jim Finley, Jerry Maglaughlin, John Ridley, Randall Bonnell, Chris Allen ("Dorm Mom"), Georgette Flanigan ("Mother of Dorms"), and Britta Schroeder.

Thank you to the community at CSU, including Dan Scott and Katherine Lininger, my academic big siblings who showed good research habits, accepted me as a peer, and introduced me to a citation manager. I would also like to specifically thank Krista Garrett, my best friend and the person I followed to CSU. Krista, you prevented me from giving up on grad school when it was hard, showed me how to be disciplined with my time, and taught me to write emails like a 35-year-old man. May we always be samies!

Finally, thank you to my family, including the family I've chosen (Papa, Ryan, Copper, Juniper, Steve, and Michelle) and those I was stuck with from the beginning. Hey, Uncle David, I need to be picked up at the Denver airport. Fancy driving my car to Colorado again? Ryan Brown, you are the best pack mule, survey technician, and bear bait a geomorphologist could ask for. I am so grateful to know you and for the fact that you let me drag you to Alaska. Chapters 3 and 4 would not exist without your field help and your software-savvy engineering brain. I love you all very much.

This project was funded by several generous organizations including Colorado State University, Denali National Park and Preserve, the EDMAP National Mapping Initiative (Award No. G18AC00093), the Geological Society of America, the Quaternary Geology and Geomorphology Division of GSA, and the Sigma Xi Research Society.

DEDICATION

I dedicate this dissertation to my family, who inspired my curiosity and supported my passions. To my parents, Kent and Julie Weiss, who made me both earnest and stubborn; to my sister, Rebecca Anderson, who made me resilient; to Copper and Juniper, emotional support team extraordinaire, and to my fiancé, Ryan Brown, who agreed to join me on this wild adventure.

TABLE OF CONTENTS

LIST OF TABLES

LIST OF FIGURES

1. INTRODUCTION

Landslides are a type of mass movement that rapidly transport material downslope. Multiple types of landslide are classified according to the dominant material (rock, unconsolidated sediment, etc.), degree of internal deformation, failure plane geometry, and speed (Varnes, 1978; Cruden and Varnes, 1996; Hungr et al., 2014). Key mass movement studies note the distinction between "slides," where cohesive masses of material move along a discrete slip plane, and "flows," where internal deformation allows for partially fluid movement (Iverson et al., 1997). The term "landslide," however, is widely used to refer to a range of movement styles, including both true slides as well as flows and rockfall (Varnes, 1978; Hungr et al., 2014). The term "landslide" in this work refers to any slide or flow that maintains contact with the bed.

Landslides are a crucial component of landscape development and maintenance and are capable of significant geomorphic work by reshaping topography, delivering sediment and nutrients to surface water, and removing vegetation (Schuster and Highland, 2007; Hilton et al., 2008; Goode et al., 2012). In mountainous environments, landscape-scale erosion by landslides drives topographic expression and the denudation of landscapes (Stock and Dietrich, 2006; Anderson et al., 2015). In fact, landslides are one of the dominant mechanisms of geomorphic adjustment following the development of steep hillslopes by glaciation (Ballantyne, 2002b, 2002a) or tectonic uplift (Roering et al., 2015).

At the most fundamental level, landslide initiation occurs when gravitational forces overcome a threshold of stability determined by the slope angle, amount of material, pore pressure, internal friction and cohesion (Lu and Godt, 2008; Griffiths et al., 2011). Using this framework, landslides may occur where thresholds of slope angle and available material are met

(Dietrich and Dorn, 1984; Parker et al., 2016), and landslides are triggered by increases in driving forces (e.g. pore pressure) or a loss of resisting forces (e.g. cohesion and friction). Landslide triggers therefore include rain or snowmelt, which increase soil saturation (Godt and Coe, 2007; Iverson et al., 2011; Borga et al., 2014; Sidle and Bogaard, 2016), and seismic activity, which can reduce cohesion and increase local shear stress (e.g. Kargel et al., 2016; Higman et al., 2018). Fire can also increase slope susceptibility by removing vegetation and altering infiltration rates (Nyman et al., 2013).

Landslides in permafrost regions are unique in some of the geomorphic processes that contribute to slope susceptibility and landslide triggering. The presence of permafrost reduces groundwater conductivity and connectivity (Walvoord and Kurylyk, 2016b), saturation of the active layer (Shan, Guo, Wang, et al., 2014), and reduced cohesion and friction along ice-rich permafrost surfaces (Zimmerman and Haeberli, 1992). Climate change is rapidly thawing permafrost at high latitudes and high elevations (Slater and Lawrence, 2013; Blunden and Arndt, 2017). The instantaneous thaw of ice-rich permafrost and the transition to freeze-thaw systems may fundamentally alter landslide regimes in permafrost regions.

The ability to monitor permafrost loss across large and remote areas is inherently difficult and observed loss of permafrost is limited by the period of record (Walvoord and Kurylyk, 2016b). In some cases, remotely sensed imagery (airborne or satellite data) can also be used to estimate soil moisture, ground temperature, and ground deformation (e.g. van der Sluijs et al., 2018; Lara et al., 2019; Zhao et al., 2019; Zwieback et al., 2019). For example, researchers in China mapped permafrost distribution at different time windows with an ~90% accuracy using mean decadal air temperature, topography, and land coverage (NDVI) data (Zhao et al., 2019). Repeat thermal surveys can measure the radiant temperature of the ground surface to monitor

permafrost stability at smaller scales (van der Sluijs et al., 2018). Despite the increased availability of remote datasets, understanding the fundamental processes governing hillslope response to permafrost thaw is crucial for predictions of landslide hazards and sediment dynamics in upcoming decades. As patterns of landslide occurrence change, improved understanding of landslides in permafrost regions is more important than ever.

Climate change has resulted in rapid changes to key processes that influence landslide initiation, including generating periods of rapid snowmelt when air temperatures rise and increasing the frequency of high-intensity rainfall (e.g. Gariano and Guzzetti, 2016). The study of landslide process is therefore even more critical as land managers try to predict the effect of changing landslide regimes on sediment and nutrient budgets and human safety.

In addition to the effect on the natural landscape, landslides also pose significant hazards to people and infrastructure. Between 1993 and 2002, over 40,000 recorded deaths resulted from landslides worldwide (Alexander, 2005; Crozier, 2013). Rapidly mobile landslides or large-magnitude landslide swarms are particularly damaging to human safety and infrastructure (e.g. Iverson et al., 2015; Kargel et al., 2016). Although low population density lowers the traditional estimate of "risk" in many permafrost regions, interior Alaska and other remote high-latitude regions are vulnerable to landslides and other natural disasters, as access to emergency services is limited and infrastructure is sparse (Cutter et al., 2003; Cutter and Finch, 2008).

The overarching goal of this study is to improve the understanding of geomorphic controls on landslide initiation at high latitudes. The research questions, hypotheses, and methodology were developed in cooperation with Denali National Park administrators to address gaps in the fundamental knowledge of landslide processes and to answer practical management questions in the context of climate change. The fundamental results are therefore easily

applicable to land management decisions and hazard mitigation. The three main chapters are organized according to the spatial scale of investigation.

Chapter 2 provides a review of the response of landslide regimes to climate change in permafrost regions around the globe. Objectives of this chapter are to use mechanistic knowledge of landslide processes and existing observational studies to predict how permafrost thaw will change landslide regimes. Specific questions addressed in Chapter 2 include:

1. Will changing permafrost conditions alter the dominant styles of slope failure on a scale that is significant for geomorphic systems, ecosystems, and land managers?
2. Will an increase in landslide frequency be accompanied by an increase in mass movement magnitude?
3. What is the timescale of adjustment, i.e. will high-relief systems adjust to a new equilibrium state on human timescales?
4. What is the degree to which anthropogenic activity exacerbates permafrost-related slope instability? What are the most effective methods for slope stabilization?
5. What is the net influence of mass movements and thermokarst features on terrestrial carbon budgets? Will increased landslide frequency and potential changes in failure style result in a net release or sequestration of soil carbon?

Chapter 3 evaluates spatial distribution and controls on landslide initiation at a regional scale in the Denali National Park road corridor. Hypotheses tested in this chapter include:

1. A disproportionate number of landslides initiate in felsic volcanic rocks.
2. A disproportionate number of landslides initiate in permafrost.
3. Landslides will be non-randomly distributed according to topographic variables including slope angle, aspect, and slope convergence.

Chapter 4 investigates site-specific landslide disturbance at a local scale by evaluating the development of three shallow-seated, shallow-angle landslides over time. Hypotheses tested in this chapter include:

1. Landslides will demonstrate observable displacement over the course of the 2-year study.
2. Older landslides will exhibit greater topographic stability over the course of the 2-year study.
3. The active layer is thicker within an active landslide than it is in the proximal undisturbed slope.

2. LANDSLIDE RESPONSE TO CLIMATE CHANGE IN PERMAFROST REGIONS[1]

2.1 INTRODUCTION

Changing climate, including increased average temperature and changing weather patterns, is particularly pronounced at high latitudes (ACIA, 2004; Intergovermental Panel on Climate Change (IPCC), 2013, 2014; Blunden and Arndt, 2017; Francis et al., 2017). Arctic and subarctic average yearly temperatures have increased at 2-4 times the rate of global averages in the last several decades, and are likely to continue warming at faster rates in the coming century (Masson-Delmotte et al., 2006; Screen et al., 2012; Alexeev and Jackson, 2013; Snyder, 2016; Intergovermental Panel on Climate Change (IPCC), 2013). Many of the defining conditions of alpine and high-latitude tundra environments, including the presence of permafrost and permafrost ice, are likely to experience dramatic changes as average temperatures continue to rise (Harris et al., 2009; Christiansen et al., 2010; Romanovsky et al., 2010; Farbrot et al., 2013; Slater and Lawrence, 2013; Westermann et al., 2013; Gisnås et al., 2017; Westermann et al., 2017; Blunden and Arndt, 2017). One such change includes an increase in hillslope soil erosion and landslides in permafrost areas with sufficient topographic relief (Gooseff et al., 2009; Shan et al., 2014a). In this review, I analyze the influence of permafrost thaw on landslide processes and geomorphic implications of changing landslide regimes in permafrost regions (Fig. 2.1). In addition, I synthesize existing knowledge and identify paths forward based on pertinent research questions that have yet to be addressed.

As used throughout this review, the term "permafrost" refers to ground (soil, sediment, or rock) that remains below 0º C for at least two consecutive years (Dobinski, 2011). The term

[1] Chapter published as Patton, A. I., Rathburn, S. L., Capps, D. M., 2019, Landslide response to climate change in permafrost regions, *Geomorphology, v. 340 p. 116-128.*

"landslide" is used to refer to the types of slope movements in the classification scheme developed by Varnes and Cruden (Varnes, 1978; Cruden and Varnes, 1996) and updated by Hungr et al. (2014), including planar block slides, rotational slides, debris slides and avalanches, flows of various materials, and rockfall. In this review, I focus the discussion on flows and slides, which maintain contact with the bed during downslope transport (Cruden and Varnes, 1996; Hungr et al., 2014), and landslides in permafrost regions where seasonal gradients between frozen and thawed substrate influence slope failure processes (Leibman, 1995; Lewkowicz and Harris, 2005b; Lewkowicz, 2007; Blais-Stevens, Kremer, et al., 2015). In recent literature describing the effects of permafrost degradation (e.g. Bowden et al., 2008; Gooseff et al., 2009; Dugan et al., 2012; Lafrenière and Lamoureux, 2013; Hong et al., 2014), the term "thermokarst features" often includes various types of landslides. In these cases, thermokarst subsidence occurs on hillslopes and includes a component of downslope movement. The term "cryogenic landslide" is also used in the literature to specify landslides that occur due to ice-related processes (e.g. Leibman, 1995; Leibman et al., 2014).

To evaluate the direct effect of permafrost thaw on landslide regimes, I explore the literature on landslides in permafrost regions and the pertinent properties of permafrost that influence landslide mechanics. I include both high-elevation and high-latitude systems in this synthesis (Fig. 2.2) because many of the processes discussed are similar in both types of permafrost. Much of the available literature focuses geographically either in highly sensitive permafrost regions (e.g. northern Alaska) or where population density is high (e.g. the European Alps) (Fig. 2.3). After introducing this literature, I organize the discussion according to five pertinent questions related to the type, frequency, magnitude, and timescale of expected change to landslide patterns in permafrost regions, as well the ecological impacts of changing landslide

occurrence. Most pertinent to this review are the hydrologic and physical effects of permafrost thaw and the loss of permafrost ice, described below, as these processes directly influence the shear strength of slope materials by varying pore pressure, cohesion, and internal friction, with a net effect of reducing shear strength of both bedrock, soil, and sediment.

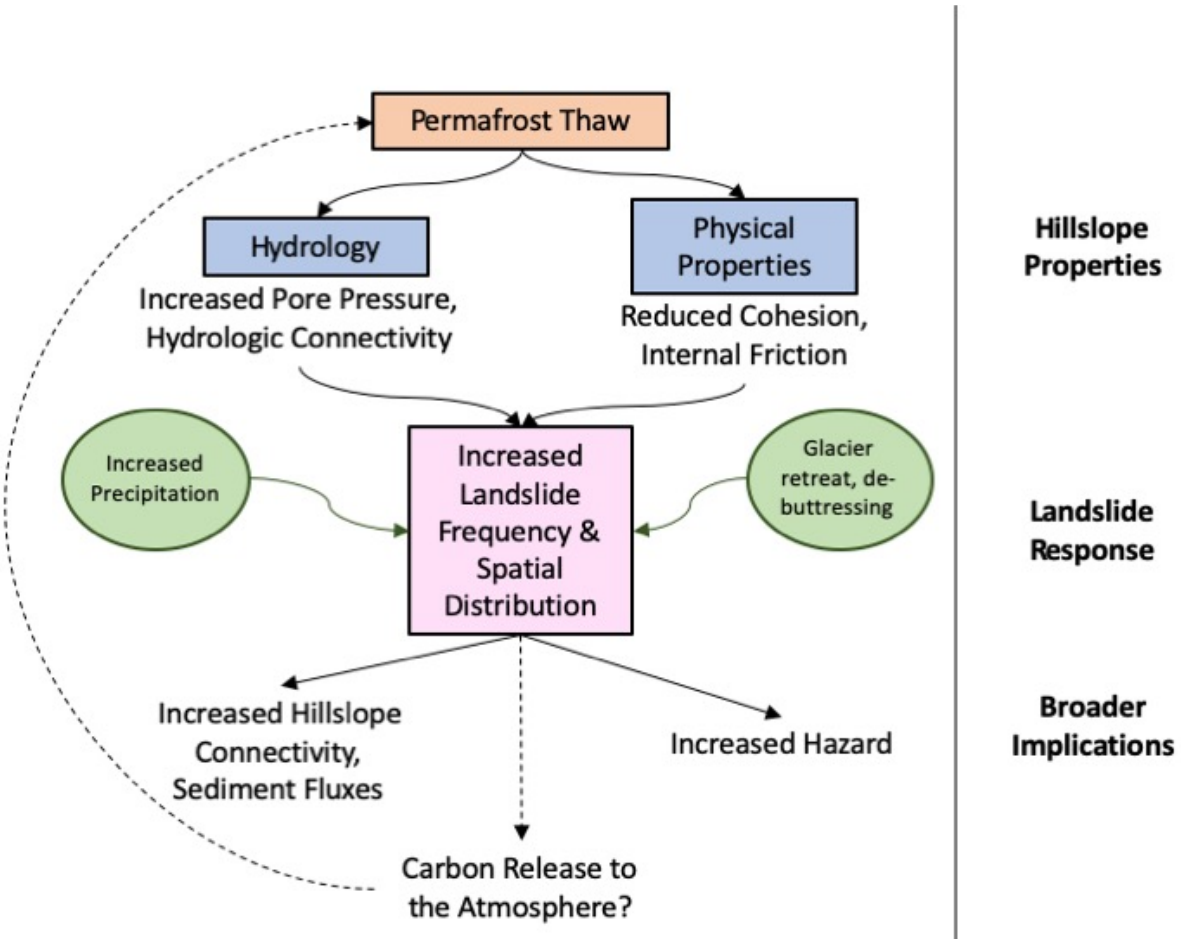

Figure. 2.1. Conceptual model of landslide response showing known effects of permafrost thaw in high-relief permafrost terrain, and some of the implications for geomorphic, ecological, and human systems. Dashed lines indicate uncertainty regarding the direction or magnitude of response.

2.1.1 Landslides in a changing climate

Landslide process and climate patterns are closely linked (Soldati et al., 2004), with evidence for this correlation throughout the geologic record and apparent in modern observation.

Correlative studies indicate that climate variables are controls on landslide process (Borgatti and Soldati, 2010; Gariano and Guzzetti, 2016; Moreiras, 2017; Matthews et al., 2018). Glacier retreat at the end of the last glaciation and increase in precipitation in the mid-Holocene both correlate with periods of increased landslide occurrence in Europe (Soldati et al., 2004; Borgatti and Soldati, 2010), and dates of Holocene rockslides in Norway correlate with periods of high temperature (Matthews et al., 2018). In fact, even when accounting for other factors (anthropogenic activity, seismicity, and changes in vegetation), changes in landslide frequency may serve as effective proxies to indicate climate change in past and present records (Soldati et al., 2004; Borgatti and Soldati, 2010; Leibman et al., 2014).

As human activity increases average global temperature, changing climate conclusively impacts slope stability and typical patterns of landslide occurrence (Gariano and Guzzetti, 2016). This poses a serious challenge for landslide practitioners and land managers, as landslide hazard forecasting is already difficult in a static climate and even more challenging in a changing climate (Coe and Godt, 2012). The specific impacts of climate change on landslide frequency, spatial distribution, and magnitude are poorly understood (Gariano and Guzzetti, 2016), particularly because climate predictions typically provide average conditions across regional spatial scales, while landslide hazards forecasting usually focuses on extreme weather at smaller scales (Coe and Godt, 2012). Although this review focuses on the effects of permafrost thaw on landsliding, it is important to note the diverse effects of climate on landslide occurrence.

In general, changing precipitation patterns increase subsurface saturation and pore pressure; as average temperatures rise, total precipitation is also likely to increase, as well as the frequency of high-intensity rainfall events at northern high latitudes (Orlowsky and Seneviratne, 2012; Kharin et al., 2013). Similarly, melting snow and ground ice (Huggel et al., 2010; Daanen

et al., 2012) can increase local pore pressure in response to daily or seasonal fluctuations in temperature. Where rainwater or meltwater persists in the subsurface, increased pore water pressure and reduced shear strength increase the likelihood of slope failure. Landslide initiation commonly occurs when threshold values of cumulative rainfall and intensity are met (Dhakal and Sidle, 2004) during atmospheric events (e.g. Eisbacher and Clague, 1984; Coe et al., 2014; Pavlova et al., 2014; Parker et al., 2016; Patton et al., 2018). Changing precipitation patterns and rapid snow/ice melt are therefore likely to increase the frequency and magnitude of large landslides irrespective of the presence of permafrost (Huggel et al., 2012; Stoffel and Huggel, 2012). Changes in vegetation, soil, and land use that relate to climate may also influence patterns of landsliding, although multi-directional feedback processes introduce complex changes in slope stability, and are therefore difficult to evaluate (Gariano and Guzzetti, 2016).

Glacier retreat as climates warm also reduces lateral support of over-steepened valley walls (Ballantyne, 2002a, 2002b) and can reduce slope stability by de-buttressing steep hillslopes (Lane et al., 2016), initiating the propagation of stress-release fractures, and contributing to steep hillslopes through crustal rebound (Evans and Clague, 1994; Deline et al., 2015; Moreiras, 2017). Paraglacial adjustment after glacier retreat therefore includes a period of heightened landslide activity (Ballantyne, 2002a; Soldati et al., 2004; Klaar et al., 2014). Destabilization of recently glaciated hillslopes in response to modern climate change has already been observed in the European Alps, Canada and Alaska following the retreat of valley glaciers (Haeberli et al., 1997; Huggel et al., 2012; Stoffel and Huggel, 2012). These effects of meltwater, atmospheric water input, and glacier retreat on landslide occurrence can be seen in both permafrost and seasonally thawed systems.

Although I briefly consider the effects of permafrost degradation on rockfall in the discussion of the impact of permafrost thaw on mechanical properties of the subsurface, the link between permafrost thaw and increased rockfall rates is well established in the literature (e.g. Gruber and Haeberli, 2007; Harris et al., 2009; Allen and Huggel, 2013; Draebing et al., 2017; Ravanel et al., 2017). Readers are directed to an existing review of the effects of climate change on rockfall for further discussion on this topic (Gruber and Haeberli, 2007).

2.2 GLOBAL PERMAFROST THAW

Warming average temperatures have already begun to cause widespread permafrost thaw around the globe and particularly at high latitudes (Slater and Lawrence, 2013; Blunden and Arndt, 2017). While forecasts of permafrost extent in the coming century are highly variable (Fig. 2.2), even the most conservative models predict permafrost loss in discontinuous zones by 2099 (Slater and Lawrence, 2013). Regional monitoring efforts confirm that permafrost is near 0° C across large areas in northern Europe, Iceland, Greenland (Harris et al., 2009; Christiansen et al., 2010; Farbrot et al., 2013; Westermann et al., 2013; Gisnås et al., 2017), the European Alps (Harris et al., 2009), Alaska (Osterkamp et al., 2009; Panda et al., 2014; Pastick et al., 2015), Siberia (Romanovsky et al., 2010; Westermann et al., 2017), northeastern China (Jin et al., 2000; Wei et al., 2011; Shan et al., 2014b; Wang et al., 2015), the Tibetan Plateau (Blunden and Arndt, 2017), and South America and the Antarctic Peninsula (Rabassa, 2010; Blunden and Arndt, 2017). In many areas, monitoring efforts have already observed loss of large areas of permafrost (Osterkamp et al., 2009; Shan et al., 2015; Gisnås et al., 2017), and loss of permafrost is expected to continue as average temperatures increase.

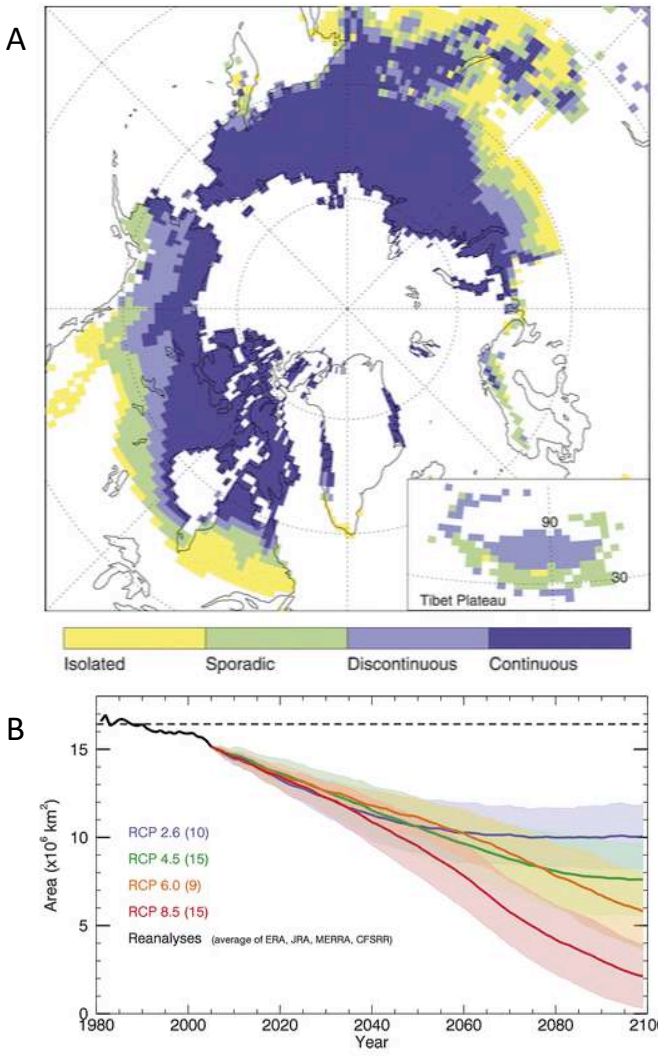

Figure. 2.2. Figures from Slater and Lawrence (2013) A) showing the estimates of permafrost extent (as of 2013) of continuous-isolated permafrost regions in the northern arctic and subarctic and B) demonstrating the variable projected change in permafrost area (x10^6 km^2) based on climate change until the year 2100. Although permafrost is most rapidly thawing in arctic regions (Blunden and Arndt, 2017), both alpine and high-latitude permafrost regions are subject to permafrost degradation as climate changes. ©American Meteorological Society. Used with permission

The greatest observed increase in permafrost temperatures is in northern Alaska, Canada, and western Siberia (Blunden and Arndt, 2017). In Alaska, where permafrost accounts for approximately 38% of the total land area, it is likely that ~40-60% of permafrost will be lost by the end of the century (Pastick et al., 2015). The ability to monitor permafrost loss across large

and remote areas is inherently difficult and observed loss of permafrost is limited by the period of record (Walvoord and Kurylyk, 2016b). Therefore, understanding the fundamental processes governing hillslope response to permafrost thaw is particularly important for predictions of landslide hazards and sediment dynamics.

2.2.1 Hydrologic implications of permafrost thaw

Due to its low hydraulic conductivity (K), permafrost controls the storage and movement of groundwater and can result in complex hydrologic systems (Bring et al., 2016; Walvoord and Kurylyk, 2016b). In contrast to typical temperate groundwater systems, permafrost regions are often characterized by a vadose zone in which all pore space is occupied by ice, resulting in a near-impermeable boundary. Where this is the case, the active layer (seasonally unfrozen) may act as a shallow perched aquifer, controlling runoff and surface water response to precipitation and snowmelt (Yamazaki et al., 2006; Koch et al., 2013; Esper Angillieri and Perucca, 2015; Bring et al., 2016). Increased pore pressure in a saturated active layer can reduce stability and initiate downslope movement at variable time scales (Zimmerman and Haeberli, 1992; Rist and Phillips, 2005; Oliva and Ruiz-Fernández, 2015; Shan et al., 2015). Ice-rich permafrost boundaries therefore create highly saturated, low friction sliding surfaces (Zimmerman and Haeberli, 1992; Wang et al., 2014; Shan et al., 2015). Aquifers within unfrozen zones of permafrost (taliks) and below the permafrost boundary are typically disconnected from the surface aquifer in the active layer. In cases where the permafrost layer includes unsaturated frozen material, groundwater may continue to flow through macropores until the infiltrating water freezes (Walvoord and Kurylyk, 2016b). In discontinuous permafrost systems, groundwater hydrology is particularly complex, with high variability in groundwater depth and subsurface flow rates.

As the active layer thickness increases in the initial stages of permafrost thaw, a larger portion of the subsurface becomes characterized by seasonal groundwater flow, with substantial influence on the local hydrologic system (Walvoord and Kurylyk, 2016b). In discontinuous permafrost systems, loss of permafrost typically results in an increase in baseflow. This is in part due to meltwater from permafrost ice producing short-term pulses in groundwater saturation and local streamflow (Li et al., 2015; Shan et al., 2015), although this effect is temporally limited. Changes to the hydrologic structure of the subsurface have a longer-lasting effect on groundwater dynamics, particularly where loss of impermeable, ice-rich permafrost opens vertical and lateral pathways for groundwater flow (Wei et al., 2011). Additionally, topographic response to loss of ground-ice alters local groundwater storage, runoff, and routing (Gooseff et al., 2009; Connon et al., 2014). Talik "breakthroughs", or connection to other groundwater aquifers during permafrost thaw, also facilitate exchange of water, nutrients, and heat between systems, with advection potentially increasing the rate of nearby permafrost thaw (Rowland et al., 2011; Wei et al., 2011; Walvoord and Kurylyk, 2016b). The overall effect of permafrost thaw through time is therefore a temporary input of liquid water, increasing pore water pressure (Huggel et al., 2010; Shan et al., 2015). In the years following permafrost ice melt, permafrost thaw results in an increase in hydrologic connectivity within the groundwater system and between groundwater and surface water (Connon et al., 2014), such that average subsurface pore pressure may decrease (Shan et al., 2015) and groundwater hydrology is more responsive to atmospheric conditions and regional aquifers.

2.2.2 Implications for physical properties of near-surface materials

Bedrock, soil, and sediment in permafrost experience predictable changes in physical properties as they transition to temperatures > 0º C. Thresholds of cohesion, friction, and related processes are most significant in ice-rich permafrost, where loss of ice changes the fundamental behavior of the slope. For example, soil and sediment experience a significant loss of cohesion as ice warms, particularly in the transition from frozen to unfrozen conditions (Haeberli et al., 1997; Fischer et al., 2013; Krautblatter et al., 2013; Guo et al., 2014). Experimental data indicate that freeze-thaw transitions may reduce soil cohesion by 50-75% (Guo et al., 2014). Increased ice temperatures and the transition from ice to water also reduces the coefficient of friction along ice surfaces (Rist, 2008; Huggel, 2009) and the internal friction angle of various materials (Guo et al., 2014; Li et al., 2014). Increased air and ground temperature therefore typically reduce shear strength of subsurface materials (Huggel et al., 2010, 2012, 2013; Stoffel et al., 2014; Ferrero et al., 2014). In fact, compressive and tensile strength of water-saturated bedrock may decrease by up to 50% when temperatures rise above 0º C due to the dramatic loss of cohesion (Krautblatter et al., 2013). This loss of shear strength of near-surface materials on a hillslope lowers the critical stresses required for slope failure to occur. Furthermore, volume loss and surface subsidence due to melting ground ice can generate steep topography at multiple scales, reducing lateral support for upslope material.

Unsurprisingly, variation in shear strength varies spatially and temporally (Blikra et al., 2012; Draebing et al., 2014, 2017). Spatial variability in ground temperatures and rock strength varies with factors including aspect (Magnin et al., 2015) and snow characteristics (Geertsema, 2012; Draebing et al., 2014; Magnin et al., 2015; Draebing et al., 2017). Snowpacks that persist through the summer can insulate permafrost from warm air and help maintain low temperatures

(Draebing et al., 2017), while deep winter snowpack can generate the opposite effect by insulating permafrost from cold air temperatures (Slater and Lawrence, 2013; Addison et al., 2016). Shear strength also varies temporally, on both seasonal and multiannual scales. Seasonal variation in subsurface temperature, snow cover, and liquid water content (Shan et al., 2015) contribute to lower rock strength in early summer and autumn (Hasler et al., 2012; Blikra and Christiansen, 2014; Draebing et al., 2014; Oliva and Ruiz-Fernández, 2015). As average air temperatures rise over longer timescales (multiannual-multidecadal), permafrost thaw will mechanically destabilize bedrock and other slope materials (Krautblatter et al., 2013; Draebing et al., 2017). Furthermore, the process of hillslope disturbance during landsliding facilitates heat flux into a hillslope, creating a feedback mechanism and promoting loss of shear strength and landslide propagation (Oliva and Ruiz-Fernández, 2015).

In addition to the intrinsic material properties altered by warming ground temperatures and loss of ice (Zimmerman and Haeberli, 1992), the transition from perennially frozen to seasonally frozen ground accelerates the effect of freeze-thaw processes in both bedrock and unconsolidated material (Haeberli et al., 1997). The freeze-thaw process increases the degree of fracturing in the near surface and generates planes of weakness for landslide failure to occur. Freeze-thaw activity and increased fracture density may also increase rockfall rates (Ballantyne, 2002b; Hales and Roering, 2007) and the supply of unconsolidated material that is susceptible to landslide failure. Furthermore, freeze-thaw cycles are characterized by greater variability of subsurface temperature and moisture content, which results in substantial fluctuations of shear strength (cohesion and friction angle) and drives opportunity for landslide initiation (Guo et al., 2014).

2.2.3 Changing fire regimes: compounding climate change effects

In addition to increasing global temperature, climate change is likely to alter fire regimes in permafrost regions (Hu et al., 2010; Higuera et al., 2011). Fire-driven permafrost degradation, active layer thickening, and thermokarst subsidence is likely to trigger landslides at an increasing rate as arctic fires become more frequent (Huscroft et al., 2004; Jones et al., 2015). Particularly on steep hillslopes, post-disturbance changes in vegetation prevent recovery of pre-fire permafrost conditions, such that active layer thickening persists over the long term (Racine et al., 2004; Rocha et al., 2012). On the Seward Peninsula of Alaska, the active layer remained thick or permafrost remained entirely degraded for at least 24 years after the initial disturbance (Racine et al., 2004). Fire regimes therefore accelerate the impacts of climate change in controlling slope stability by altering vegetation communities and increasing active layer depth. Where active layer thickness controls landslide occurrence (discussed in the following sections), fire-induced active layer thickening may also increase landslide frequency and magnitude.

2.3 QUESTIONS TO ADDRESS

In a review of the major contributions in the English-language literature that address the influence of permafrost degradation on landslide activity (Table 1), I identify relevant topics to organize discussion of the state of knowledge about landslides in permafrost terrain. Some of these topics have been addressed and others, particularly Question 5, still offer opportunity to produce fundamental data and analysis. The geographic distribution of these major studies is clustered in North America and the European Alps (Fig. 2.3), with a few studies from China, Norway, and Russia. Additional research on this topic has been described in other languages and could be incorporated into the English-language literature through international collaboration.

Based on a mechanistic understanding of changing hydrologic and physical properties in regions of permafrost thaw, as well as the contributions outlined in Table 1, this review paper synthesizes the hydrologic and physical processes of permafrost thaw to summarize and predict the response of landsliding due to ongoing permafrost degradation. These responses will be addressed according to the following questions:

1. Will changing permafrost conditions alter the dominant styles of slope failure on a scale that is significant for geomorphic systems, ecosystems, and land managers?
2. Will an increase in landslide frequency be accompanied by an increase in mass movement magnitude?
3. What is the timescale of adjustment, i.e. will high-relief systems adjust to a new equilibrium state on human timescales?
4. What is the degree to which anthropogenic activity exacerbates permafrost-related slope instability? What are the most effective methods for slope stabilization?
5. What is the net influence of mass movements and thermokarst features on terrestrial carbon budgets? Will increased landslide frequency and potential changes in failure style result in a net release or sequestration of soil carbon?

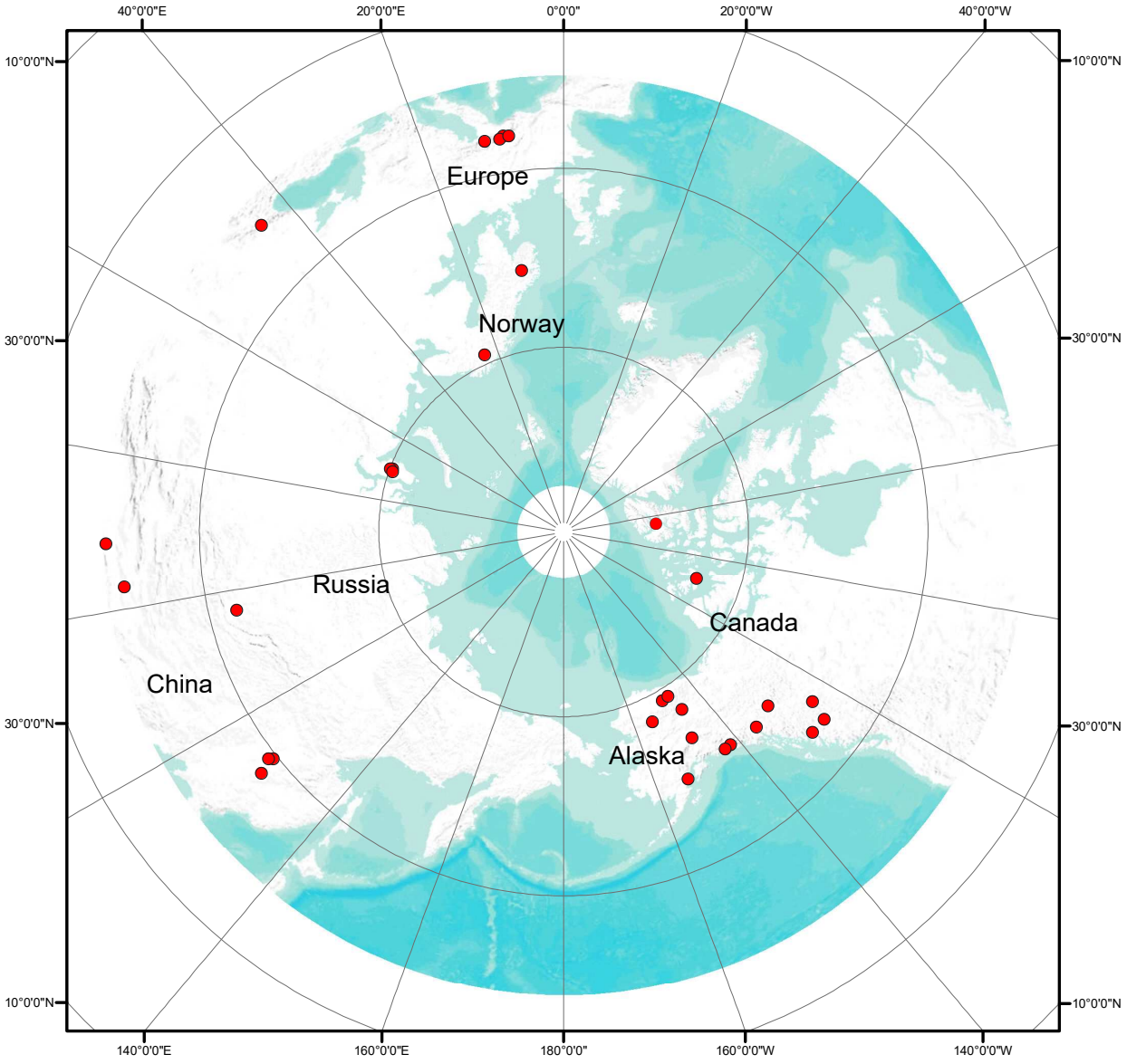

Figure. 2.3. Spatial distribution of major studies, as listed in Table 1A, that contribute to the understanding of the influence of permafrost thaw on hillslope processes. Not pictured are two studies from New Zealand and the Antarctic Peninsula (Table 1).

Table 2.1. Summary of the major contributions to the literature of permafrost and landslides (English language only). Studies listed in section A are shown in Figure 3.

Author	Year	Contribution	Location of study
A. Landslide research in permafrost terrain: ***Risk assessments, landslide/subsidence inventories, and mechanistic/morphologic evaluations***			
Blais-Stevens et al.	2015	Map thaw slump susceptibility and discuss likely future trends	Yukon-AK Highway
Blikra et al., Blikra and Chrisiansen	2012, 2014	Monitor rockslide displacement to document seasonal variation	Norway
Bowden et al.	2008	Measure sediment and nutrient delivery from thermokarst features	North Slope, AK
Capps et al.	2017	Conduct a geohazards risk assessment in a region of discontinuous permafrost	Denali, AK
Daanen et al.	2012	Evaluate, measure, and analyze frozen debris lobe movement	Brooks Range, AK
Fischer et al.	2013	Evaluate slope failure after glacier retreat, permafrost thaw, and temperature anomalies	European Alps
Geertsema et al.	2006	Overview of 38 catastrophic landslides that may have been triggered by climate change including permafrost thaw	British Columbia, Canada
Gooseff et al.	2009	Summarize effects of hillslope thermokarst	Northern AK
Hong et al.	2014	Model regions of Alaska susceptible to thaw settlement hazards	Alaska
Huggel	2009, 2010	Document slope failure due to thermal perturbations	Alaska, New Zealand, European Alps
Huscroft et al.	2004	Describe five examples of permafrost-driven landslides in the Yukon Territory	Canada
Jones et al.	2015	Monitoring of ground surface subsidence following fire	Northern AK
Khak and Kozyreva	2012	Catalogue the effects of anthropogenic activity on geomorphology, including landsliding and permafrost thaw	Eastern Siberia, Russia
Leibman	1995	Characterize cryogenic landslides	Yamal Peninsula, Russia
Lewkowicz	2007	Describe dynamics of active-layer detachments	Ellesmere Island, Canada
Matthews et al.	2018	Develop a chronology of rock slope failure during the Holocene to evaluate controlling mechanisms	Jotunheimen, Norway
Oliva and Ruiz-Fernández	2015	Landslide inventory and evaluation of triggering mechanisms, including changes to technical properties after permafrost thaw	Antarctic Peninsula
Pautler et al.	2010	Demonstrate that active layer detachments stimulate microbial activity	Melville Island, Nunavut, Canada
Shan et al.	2014, 2015	Detailed monitoring of landslide displacement, soil saturation, and long-term climate trends	Lesser Khingan Range, China
Shan et al. (eds);	2014	Technical publication on landslides in cold regions that discusses many of the issues presented in this review, with notable chapters cited throughout this paper, including those by: Wang et al., Li et al., Hatanaka et al., Guo et al., Leibman et al., Ferrero et al., Khomutov and Leibman	Contributions discuss landslides in China, Japan, Russia, and Europe

Zimmerman and Haeberli	1992	Evaluate a debris flows in the Alps to discuss the impacts of climate change on landslide occurrence, including the mechanisms by which permafrost thaw can reduce slope stability and trigger landslides	Swiss Alps
B. Selected reviews of landslide response to climate change			
Borgatti and Soldati	2010, 2013	Evaluate relationships between hillslope processes and climate change	N/A (Global)
Gariano et al.	2016	In-depth review of general landslide response to climate change	N/A (Global)
Haeberli et al.	1997	Review slope stability issues related to glacier shrinkage and permafrost degradation	European Alps
Stoffel et al.	2012, 2014	Review the impacts of climate change on mass movements	European Alps
Soldati et al.	2004	Evaluate climate controls on landsliding since the Last Glacial Maximum	Italian Dolomites
C. Selected global permafrost monitoring and evaluation			
Blunden and Arndt (eds.)	2017	Describe the state of global climate in the year 2016, including global permafrost distribution	N/A (Global)
Francis et al.	2017	Present new perspectives on amplified climate change at high latitudes	High Latitudes
Romanovsky et al.	2010	Discuss the state of polar permafrost between 2007-2009	High Latitudes
Slater and Lawrence,	2013	Evaluate multiple models of present and future permafrost extent	N/A (Global)
D. Selected reviews of permafrost hydrology, mechanical properties and nutrient cycling			
Connon et al.	2004	Measure changes to hydrologic connectivity in a region of permafrost thaw	NWT, Canada
Draebing et al.	2014, 2017	Model the influence of changing climate and snowpack on rock strength	Swiss Alps
Keiler et al.	2010	Analyze the effects of extreme weather in the European Alps, with a discussion of hazard implications	Eastern European Alps
Krautblatter et al.	2013	Present a physical model describing the mechanical properties of permafrost bedrock	N/A
Lafrenière and Lamoureux	2013	Document that high lacustrine solute loads reflect thermal perturbation and rainfall	Melville Island, Nunavut, Canada
Rowland et al.	2011	Model talik development under varying groundwater flow conditions	Seward Peninsula, AK
Schuur et al.	2008	Thawing permafrost may release a significant pool of C to the atmosphere	N/A (global)
Schuur et al.	2009	Determine that thawing permafrost releases old (Pleistocene) carbon	Healy, AK
Vinson et al.	2009	Describe geoengineering methods to mitigate thaw instability	Denali, AK
Walvoord and Kurylyk	2016	In-depth review of the hydrologic impacts of thawing permafrost	N/A

2.3.1 Question 1: Will changing permafrost conditions alter the dominant styles of slope failure on a scale that is significant for geomorphic systems, ecosystems, and land managers?

Landslides pose a persistent management concern worldwide, and mitigation efforts often rely upon predicting areas that are likely to experience failure using historic accounts or inventory data (Eisbacher and Clague, 1984). Changes to the current landslide regime hinder the ability of land managers to predict areas of greatest risk and plan for possible outcomes (Coe and Godt, 2012), as managers may no longer rely on historical landslide patterns to predict timing, style, magnitude, and location of landslides. Landslide studies in high-latitude regions indicate that permafrost thaw is likely to alter landslide regimes, by both increasing the frequency of landslides in general and increasing the rate of particular styles of landslides.

For example, active layer detachments (ALDs, Fig. 2.4E) may become more frequent relative to other styles of landslide failure (Blais-Stevens, Kremer, et al., 2015), particularly during an adjustment period as the active layer thickens (Huscroft et al., 2004) and melting permafrost ice allows for slip along saturated, low-cohesion surfaces (Shan et al., 2015). Because ALDs may occur even on very shallow hillslopes (Leibman, 1995; Lewkowicz and Harris, 2005b; Lewkowicz, 2007), increased ALD occurrence expands the area of landslide hazard beyond the high-angle slopes typically considered in risk management. A landslide risk assessment conducted in Denali National Park, Alaska found that slope angle ranked only 10th in predictive ability relative to other variables (Capps et al., 2017). Variables that ranked higher included precipitation, active layer thickness, and mean ground temperature, highlighting the importance of climatic and substrate characteristics in dictating landslide occurrence in high-latitude regions. Monitoring efforts in northeastern China similarly find that landslides driven by permafrost thaw typically occur on low-angle hillslopes (Shan et al., 2014b). As permafrost

systems give way to seasonal freeze-thaw conditions after this adjustment period (Gruber and Haeberli, 2007; McColl, 2012), shallow-seated ALDs may become less frequent and precipitation-driven landslides, translational block failures, and deep-seated failure of overloaded hillslopes are likely to become the dominant failure styles.

Additionally, loss of bedrock shear strength due to ice loss (Krautblatter et al., 2013; Gariano and Guzzetti, 2016) and the transition to freeze-thaw processes (Haeberli et al., 1997; Gruber et al., 2004; Gruber and Haeberli, 2007; Harris et al., 2009; McColl, 2012; Stoffel and Huggel, 2012) is likely to increase rockslide and rockfall susceptibility in bedrock slopes (Haeberli et al., 1997; Stoffel and Huggel, 2012; Huggel et al., 2013; Gariano and Guzzetti, 2016; Huggel et al., 2012). Chronologic analysis of rock slope failures in Norway throughout the Holocene indicates that increased frequency of rockslides correlates with periods of permafrost degradation (Fig. 2.4A) (Matthews et al., 2018). Loss of permafrost following modern changes in climate may therefore initiate rockslide development and motion (Blikra et al., 2012; Matthews et al., 2018). Increased erosion rates due to rockfall may also increase the availability of unconsolidated sediment that may be mobilized in subsequent landslides (Stoffel et al., 2014).

2.3.2 Question 2: Will an increase in landslide frequency be accompanied by an increase in mass movement magnitude?

The magnitude of landslides is likely to increase, due to increased sediment delivery to source areas and increased frequency of high-intensity rainfall (Geertsema et al., 2006; Stoffel et al., 2014). As permafrost thaws, increased hydrologic connectivity within local and regional groundwater systems generates groundwater hydrology that is more responsive to atmospheric conditions at depth (Huggel et al., 2010). Such changes may lower thresholds of cumulative

rainfall and/or rainfall intensity required to initiate slope failure, allowing for larger landslides to occur during relatively frequent storms. Because the presence of permafrost limits the regressive erosion of propagating landslides and typically constrains failure depth to the shallow active layer (Zimmerman and Haeberli, 1992; Deline et al., 2015), loss of permafrost increases the availability of loose material and increases the potential for deep-seated landslides (Zimmerman and Haeberli, 1992; Harris et al., 2009).

Large-magnitude mass movements in the European Alps and New Zealand have already been causally linked to extreme high temperatures (Huggel, 2009; Huggel et al., 2010; Keiler et al., 2010; Allen and Huggel, 2013), indicating that atmospheric conditions may increase failure magnitude on a scale of days to seasons. Based on spatial distribution and preceding temperatures, several catastrophic landslides in British Columbia also appear to have been conditioned or triggered by degrading permafrost, and limited data suggest that the frequency of large (>0.5 M m^3) landslides is increasing (Geertsema et al., 2006). Thermally-induced slope failures have been linked to increased runoff and groundwater saturation due to melting snow and ice (Huggel et al., 2010; Hatanaka et al., 2014; Shan et al., 2015), increased frequency of extreme rainfall events (Keiler et al., 2010), and de-buttressing of steep slopes after glacier retreat (Evans and Clague, 1994; Haeberli et al., 1997; Borgatti and Soldati, 2013; Moreiras, 2017). Ice-rich landslides may also be characterized by longer runout distances and higher velocities, as melting ice and snow at the base of a landslide increases mobility (Lipovsky et al., 2008).

Deep-seated slope failures responding to permafrost thaw may take place over a longer timeframe (decades or longer) as the active layer deepens or permafrost thaws completely (Gruber et al., 2004; Keiler et al., 2010). Climatic conditions that reduce slope stability on short,

days to months timescales (runoff, snowmelt, glacial retreat) and long, years to decades timescales (glacial retreat, permafrost thaw) will undoubtedly interact to increase the likelihood of large-magnitude slope failures across high-relief areas (Evans and Clague, 1994; Haeberli et al., 1997; Geertsema et al., 2006; Huggel et al., 2010; Borgatti and Soldati, 2013; Hatanaka et al., 2014; Moreiras, 2017). It follows that increased frequency of extreme weather and high temperatures will continue to generate large slope failures in the upcoming decades, due to a combination of effects of permafrost degradation and other factors that are sensitive to atmospheric conditions.

2.3.3 Question 3: What is the timescale of adjustment, i.e. will high-relief systems adjust to a new equilibrium state on human timescales?

Although permafrost loss is likely to result in decreased area that is susceptible to particular styles of landsliding (e.g. shallow-seated ALDs), landslide inventory studies postulate that the adjustment period will generate heightened instability on the short term (Blais-Stevens, Kremer, et al., 2015). The question remains whether this landscape adjustment will occur on human timescales. It may be reasonable to assume that an adjustment period of increased thaw-related landslide frequency is likely to occur during the transition from continuous or discontinuous permafrost to seasonally thawed near-surface materials. Based on climate models, this transition is likely to occur relatively quickly, particularly across regions where mean annual ground temperatures are near 0° C (Osterkamp et al., 2009; Slater and Lawrence, 2013; Pastick et al., 2015). While competing models forecast highly variable climate and permafrost extent in the upcoming decades, even the most conservative models predict loss of permafrost in current discontinuous zones by 2099 (Slater and Lawrence, 2013). As stated previously, ~40-60% of

permafrost will be lost by the end of the century in Alaska, where permafrost accounts for approximately 38% of the total land area (Pastick et al., 2015). Despite the uncertainty of the predicted permafrost area, it is clear that large areas of permafrost will be lost by the end of the century, with the greatest loss of permafrost beginning in lower latitudes where permafrost is isolated, sporadic, or discontinuous (Slater and Lawrence, 2013; Blunden and Arndt, 2017). I can therefore expect thaw-related landslide occurrence to track with a front of permafrost thaw, beginning at lower latitudes/elevations and propagating to higher latitudes and elevations as permafrost loss continues (Jin et al., 2000). Similarly, a conceptual model proposed by Borgatti and Soldati postulates that the influence of permafrost on slope stability likely extends from 10^{-2} years and up to 10^{3} years (Borgatti and Soldati, 2013), which follows local thaw at a near-instantaneous scale (Hasler et al., 2012) and long-term changes in permafrost conditions.

It is also important to consider the recovery time and stabilization of individual mass movements in order to evaluate the duration of the impact of landslides on terrestrial nutrient budgets, near-surface hydrology, and sediment delivery to the fluvial network. Multi-annual observations of a permafrost-induced landslide in China noted that, once permafrost ice had fully melted, landslide deformation rates began to decrease within nine years (Shan et al., 2015). In a time-series analysis of landslides initiated by an arctic tundra fire on Alaska's northern slope, most small landslides stabilized within five years, although ongoing ice wedge degradation continued to initiate ground surface subsidence beyond five years (Jones et al., 2015). Once deformed ground surface stabilizes, a return to pre-landslide conditions may take even longer. In tropical and temperate climates, recovery of pre-disturbance vegetation communities may occur on 10^{0}-10^{2} year timescales (Marston, 2010). In high-latitude permafrost systems, however, post-disturbance colonization by historic plant communities is slower (Wang et al., 2014). Monitoring

of landslides in the Canadian high arctic did not observe recovery of pre-disturbance vegetation cover in 50 years of observation (Cannone et al., 2010). In fact, a Holocene landslide chronology for the Russian Siberian Plain indicates that vegetation recovery on ancient landslides likely took at least 300 years and potentially more than 2000 years (Leibman et al., 2014). Depending on local conditions, however, individual mass movement features may never achieve pre-disturbance communities after permafrost disturbance due to changes in local hydrology (Osterkamp et al., 2009) and ongoing climate change. While landslide initiation response may therefore occur over the course of decades to centuries, recovery of historic conditions may require 10^2-10^3 years, or may never occur. Recognizing these vegetation recovery timescales may help identify past landslides at a local level.

2.3.4 Question 4: What is the degree to which anthropogenic activity exacerbates permafrost-related slope instability? What are the most effective methods for slope stabilization?

Landslides are exacerbated by human activity, through mechanisms including de-buttressing of hillslopes by roadcuts (Swanson and Dyrness, 1975; Wemple et al., 2001), clear-cutting and deforestation (Swanston and Swanson, 1976; Barnard et al., 2001), and breaching or overtopping of earthen dams and ditches (Grimsley et al., 2016). In high-latitude regions, anthropogenic destabilization of hillslopes may be exacerbated by modifications to the near surface that often result in permafrost degradation in addition to the simple mechanical impacts (Khak and Kozyreva, 2012). Disturbance of the ground surface, such as for infrastructure development and excavation, facilitates heat exchange through the subsurface (Khak and Kozyreva, 2012; Wang et al., 2014). Other ground surface modifications, such as loss of vegetation (Nauta et al., 2014) and changes to albedo following construction (Qin et al., 2016),

can further influence the rate of permafrost thaw. Increased heat transfer causing permafrost thaw can therefore amplify the destabilizing effect of roads construction, railways, and other ground surface modifications.

In addition to hillslope stabilization techniques applied worldwide (buttressing, groundwater routing, installation of geotextiles, etc.), protecting permafrost can be a successful practice to stabilize hillslopes in critical areas. Slope stabilization efforts in permafrost terrain have been summarized in geotechnical reports (e.g. Vinson et al., 1999; Wang et al., 2014; Addison et al., 2016; Skripnuk and Ulitin, 2016). The stabilization techniques described in these studies include physical stabilization as well as methods of mitigating ice and permafrost thaw, such as removing snow during cold winter months, when snow cover insulates permafrost from the colder atmosphere; installing tubing or ducts to facilitate heat transfer between the subsurface and atmosphere in the winter; and shading the ground surface with vegetation or structures when air temperatures rise in the spring.

2.3.5 Question 5: What is the net influence of mass movements and thermokarst features on terrestrial carbon budgets? Will increased landslide frequency and potential changes in failure style result in a net release or sequestration of soil carbon?

Microbial activity of soils exposed by landslide disturbance may release permafrost carbon to the atmosphere (Pautler et al., 2010), but drainage-scale studies indicate that the effects of physical disturbance by mass wasting are small relative to the increase in solute loads (carbon or other nutrients) due to rainfall runoff and groundwater flow through a deeper active layer (Lafrenière and Lamoureux, 2013). Studies of ALDs in the High Arctic semi-desert indicate that the short-term effect of shallow landslide disturbance on ecosystem respiration is minimal

(Beamish et al., 2014). Burial of soil horizons in landslide deposition zones may offset processes that release soil carbon to the atmosphere.

Because the magnitude of these carbon fluxes influenced by landslides are not well constrained, the net effect of landsliding on carbon release vs. sequestration is currently unclear. This is an important topic for future investigative research, however. Furthermore, the scale of influence of landslides on regional carbon budgets is not currently known. Additional research is needed to quantify the approximate pool of carbon that is disturbed by landslides to determine whether it is relevant to discussion of regional and global carbon budgets.

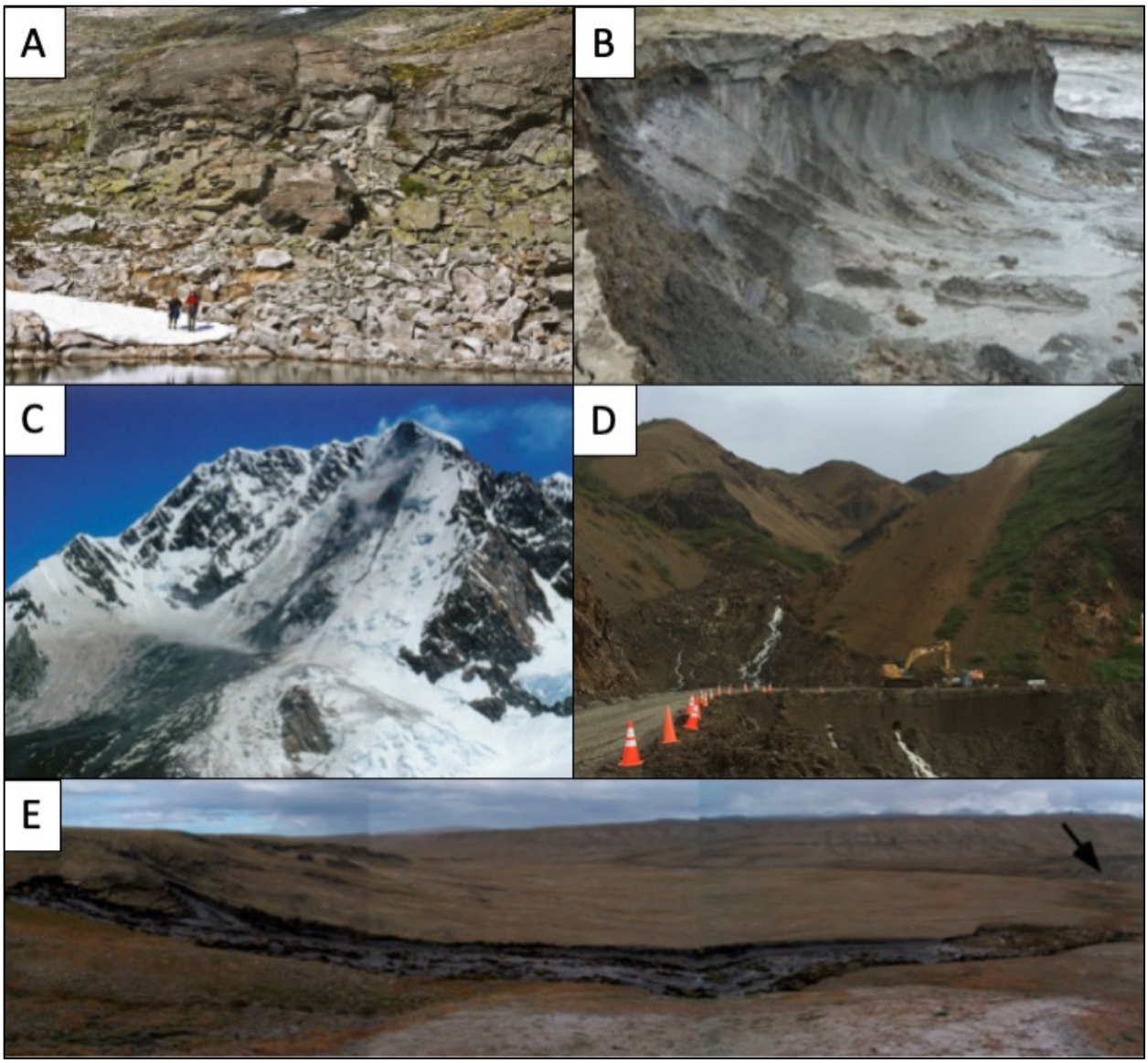

Figure. 2.4. Landslides triggered or influenced by permafrost. A) Rockslide in Norway (Matthews et al., 2018). B) "Retrogressive thaw slump" on the Yamal Peninsula, Russia (Leibman et al., 2014). C) Rock-ice avalanche on Aoraki Peak (Mt. Cook), New Zealand (Huggel et al., 2010). D) Complex landslide (debris slide/flow) that damaged infrastructure in Denali National Park, Alaska (photo by Patton, A.). E) Active layer detachment (ALD), Nunavut, Canada; arrow indicates tents for scale (Lewkowicz, 2007).

2.4 SYNTHESIS AND BROADER IMPLICATIONS

Based on the altered hydrology (Walvoord and Kurylyk, 2016b), vegetation (Racine et al., 2004; Osterkamp et al., 2009), and physical properties of annually thawed soils and bedrock

(e.g. Krautblatter et al., 2013; Guo et al., 2014), it is likely that the dynamic equilibrium states of landsliding will be fundamentally altered after permafrost thaws. I predict that landslides will be driven primarily by atmospheric input of moisture and freeze-thaw fracturing rather than responding to disconnected and perched groundwater, melting permafrost ice, and a plane of weakness between ground ice and the active layer. Transition between equilibrium states is likely to increase landslide frequency and magnitude, alter dominant failure styles, and mobilize carbon over timescales ranging from seasons to centuries. It is also important to note that changes in a number of geomorphic factors associated with permafrost thaw and increased temperature (increased hydraulic conductivity and infiltration rates, decreased cohesion, and altered vegetation communities) may have competing effects on hillslope stability at a local scale, such that exceptions to regional trends will exist.

These changes to the landslide occurrence and the physical properties of subsurface materials can pose serious geotechnical challenges (Khak and Kozyreva, 2012; Krautblatter et al., 2013) for human communities and the environment. The formation of thermokarst topography on low-relief terrain is well documented, with profound effects on local microclimate, water flow and storage, and biota (Osterkamp et al., 2009). Where thermal perturbation occurs on hillslopes, even where the slope angle is low (10-20º), landsliding is likely to become more frequent (Fig. 2.1) and on a broader spatial distribution (Leibman, 1995; Lewkowicz, 2007; Shan et al., 2014a, 2014b; Blais-Stevens et al., 2015). A more complete understanding of the influence of permafrost thaw on hillslope processes is an important component of predicting and mitigating the effects of increased landslide occurrence in permafrost regions. In addition, changing landslide regimes have several serious implications for both ecosystem processes and human communities.

First, fundamental changes to landslide regimes will alter the timing and/or magnitude of hillslope connection to surface water. Permafrost-related landslides are capable of displacing large volumes of hillslope sediment, nutrients, and soil downslope, altering the physical and ecological structure of affected hillslopes (Hilton et al., 2008; Gooseff et al., 2009; Osterkamp et al., 2009). Climate-driven changes to landslide frequency, magnitude, spatial distribution, and style are also likely to increase the connectivity of hillslopes and the fluvial network, increasing nutrient, sediment, and particulate carbon inputs to surface water in permafrost regions (Fig. 2.4B) (Bowden et al., 2008; Abbott et al., 2015; Li et al., 2016). These effects are likely to result in profound disturbance to aquatic ecosystems, where changes to nutrient budgets are integrated over large areas (Bowden et al., 2008). Disturbance to hillslope vegetation is likely to result in long-term changes to community composition in susceptible areas due to changes in microtopography and local hydrology (Racine et al., 2004; Osterkamp et al., 2009; Cannone et al., 2010). The integrated effects of climate change and changing occurrence of landslides, fire, and precipitation on ecosystem response are still not well understood.

Increased landslide occurrence may also accelerate permafrost carbon release to the atmosphere (Pautler et al., 2010). The process by which permafrost thaw releases previously sequestered carbon to the atmosphere is well documented in the literature. Several observational and experimental studies have demonstrated that thawing frozen soils releases ancient (Pleistocene) carbon to the atmosphere at measurable rates (Schuur et al., 2008, 2009; Belshe et al., 2013; Fisher et al., 2016). Because northern-latitude carbon stocks alone account for approximately 50% of the total global belowground carbon pool (Tarnocai et al., 2009) and more carbon than is contained in the atmosphere (McGuire et al., 2010), this flux is significant on a

global scale. The net effect of landslides on the carbon budget, however, is not constrained, nor is the magnitude of the carbon pool mobilized by landslides (Fig. 2.1).

Lastly, increased landslide frequency amplifies hazards to people and infrastructure (Vinson et al., 1999; Koch et al., 2014). Climate- and permafrost-induced landslide hazards are likely to fundamentally alter the safety and economic stability of human populations in permafrost terrain (Fig. 2.4D) (Vinson et al., 1999; Capps et al., 2017). The effects of increased hazard due to landsliding will be greatest when landslide hazards interact with other natural processes. For example, increased occurrence of large-magnitude landslides in steep-walled paraglacial fjords may trigger potentially catastrophic tsunamis (Fryer et al., 2004; Higman et al., 2018). Because the majority of landslide studies rely upon historical data, alteration of landslide regimes may complicate hazard assessments (Keiler et al., 2010). Particularly in remote regions, limited infrastructure and socioeconomic factors increase community vulnerability to landslides and other natural hazards (Cutter et al., 2003; Cutter and Finch, 2008). Understanding and predicting landslide response to permafrost loss is a crucial component of hazard mitigation in these communities.

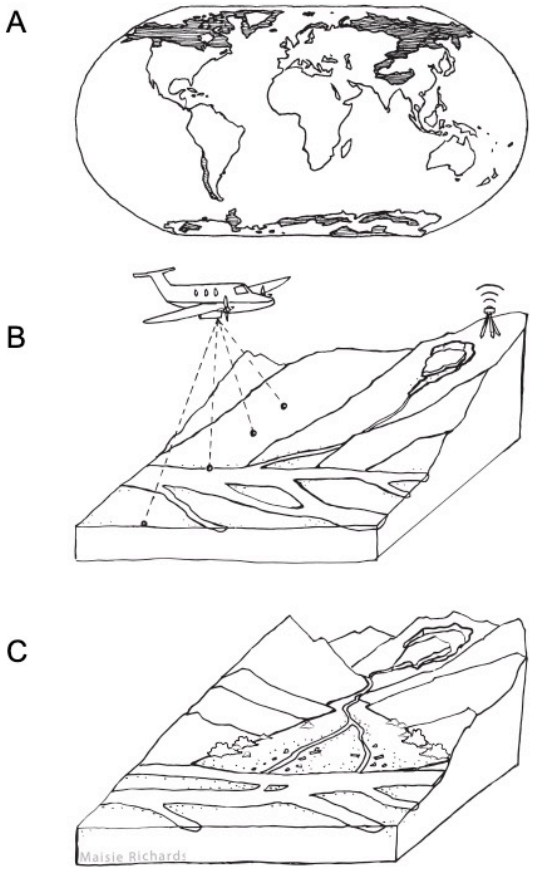

Figure. 2.5. Future research needs, ordered according to possible scales of investigation. A) Approximate permafrost distribution around the globe, which highlights the need for global-scale investigation of landslides in permafrost regions. B) Repeat imagery and remote sensing, as well as in-situ monitoring programs, will be crucial to researchers evaluating change to landslide regimes through time. C) Permafrost landslides have the potential to influence terrestrial carbon budgets and deliver carbon, other nutrients, and sediment to surface water. Illustration by Maisie Richards, www.maisierichards.com/.

2.5 FUTURE RESEARCH NEEDS

Based on a review of the literature on the influence of permafrost degradation and loss on landsliding style, frequency and magnitude, I identify three main areas of future research (Fig. 2.5). These topics will help fill gaps in knowledge and establish research directions related to this important topic, including:

1. **Expand the geographic extent of English-language research on landslides and permafrost (Fig. 2.5A).** Current studies are limited geographically, with the majority of English-language research being conducted in Alaska, Canada, and Europe (Table 1) (Gariano and Guzzetti, 2016). Expanding the range of data collection will improve understanding of global-scale variability. Large regions of Russia, northern Europe, Greenland, South America, and Antarctica are not well-represented in the English-language literature on landslides (Fig. 2.3), although important works on permafrost distribution and processes in these areas do contribute to process-based knowledge of landslide occurrence. English-language studies from the southern hemisphere are particularly scarce. Further study in these regions, international collaboration, as well as incorporation of research written in other languages (Chinese and Russian) will improve understanding of permafrost response across broad geographic regions.
2. **Maintain or initiate long-term monitoring projects and aerial data collection (Fig. 2.5B)** to allow for robust time-series analysis in upcoming decades. Long-term data are a scientifically robust strategy to evaluate the influence of climate over time, although such projects require lasting financial commitment from agencies and scientists (Coe and Godt, 2012). In particular, repeat data collection, such as the soil and air temperature monitoring study initiated in 1985 near Healy, AK (Osterkamp et al., 2009) will allow for comparative analysis over the long term to evaluate the relative influence of factors such as climate, soil temperature, precipitation, vegetation, and human activity in changing landslide regimes. Repeat collection of high-resolution topographic data and other remotely sensed datasets has immediate applicability for management of public lands (Capps et al., 2017), and can provide

the necessary tools to evaluate landslide hazards and adjustment over the course of years to decades (Kääb, 2008; Khomutov and Leibman, 2014).

3. **Quantify the net effect to carbon budget (Fig. 2.5C).** As discussed, there are competing effects of landsliding on carbon sequestration and release to the atmosphere, and the net effect on local scales or regional scales is not currently known. Quantifying the total carbon pool mobilized by landslides and the net sequestration/release will determine whether permafrost driven landslides have a significant impact on the carbon budget (Fig. 2.1).

3. LITHOLOGIC, GEOMORPHIC, AND PERMAFROST CONTROLS ON LANDSLIDING IN DENALI NATIONAL PARK, ALASKA[2]

3.1 INTRODUCTION

Landslides pose a persistent hazard in high-latitude regions where permafrost is degrading rapidly (Huggel, 2009; Blais-Stevens, Kremer, et al., 2015). Although models of forecasted permafrost loss are highly variable (Slater and Lawrence, 2013), it is likely that 40-60% of permafrost by area will be lost by the end of the century (Pastick et al., 2015). In Denali National Park (DNP), local monitoring suggests that permafrost temperatures are already near 0° C (Osterkamp et al., 2009). Modeled permafrost response to climate change in DNP suggests that although 75% of the park was underlain by permafrost in the 1950s, only 1% of the park will be underlain by permafrost by the end of the 21st century (Panda et al., 2014). Changing precipitation patterns worldwide (Stoffel and Huggel, 2012; Intergovermental Panel on Climate Change, 2013), permafrost degradation, and the transition to freeze-thaw regimes will contribute to landsliding by increasing landslide frequency and magnitude (Patton et al., 2019). Changes to landslide regimes in Alaska and other high-latitude regions increase the uncertainty of landslide hazards assessments. As such, the need for mechanistic understanding of landslide initiation and up-to-date landslide inventory data is greater than ever. Improved understanding of landslide hazards is applicable to management of public and private lands throughout permafrost regions worldwide. In particular, the physical process by which permafrost ice and topography control landsliding is likely consistent throughout high latitudes worldwide.

[2] Chapter in revision as Patton, A. I., Rathburn, S. L., Capps, D. M., Brown, R. A., Lithologic, geomorphic, and permafrost controls on landsliding in Denali National Park, Alaska, *Geosphere*.

3.1.1 Study Area

To focus on an area that is of management concern to DNP, I defined the study area as the 1-km wide Denali Park Road corridor from miles 33-66 (Fig. 3.1). The road corridor crosses the variable geology within the park, including bedrock exposures of multiple lithologies as well as diverse Quaternary sediment deposits. This transect of diverse topography and lithology allows for fundamental evaluation of multiple factors that contribute to landslide initiation in the Alaska Range and other discontinuous permafrost systems worldwide. Furthermore, the Denali Park Road provides the only access for ground vehicles to the interior of the park, and therefore is a significant resource for visitors, staff, and property owners (Vinson et al., 1999; Capps et al., 2017). I use the term study *region* to refer to a broader portion of the Alaska Range and discuss the geologic context of this specific study area.

The geology of the study region is structurally complex with regional-scale faults and folds (Csejtey et al., 1982; Gilbert, 1979; Nokleberg et al., 1994; Wilson et al., 2015). Primary lithologic units within the map area (Fig. 3.1) include Jurassic basalt and metabasalt of the Nikolai Formation, Cretaceous sedimentary rocks of the Cantwell Formation (sandstone and conglomerate), Paleogene volcanic rocks of the Teklanika Formation and Mt. Galen Formation (basalt, andesite, rhyolite, and tuff/tuff breccia), and Quaternary sediments (glacial, alluvial, etc.) (Gilbert, 1979; Csejtey et al., 1992; Yeend, 1997). The study region is located near the boundaries of multiple geologic terranes, including the Yukon-Tanana, Wrangellia, Farewell, and McKinley terranes (Csejtey et al., 1982; Ridgway et al., 2002; Dumoulin et al., 2018). Late Jurassic-Cretaceous collision and transpression of the Wrangellia island-arc composite terrane juxtaposed 3-5 km of marine strata (the Kahiltna assemblage) with the former North American continental margin (Yukon-Tanana terrane) (Ridgway et al., 2002).

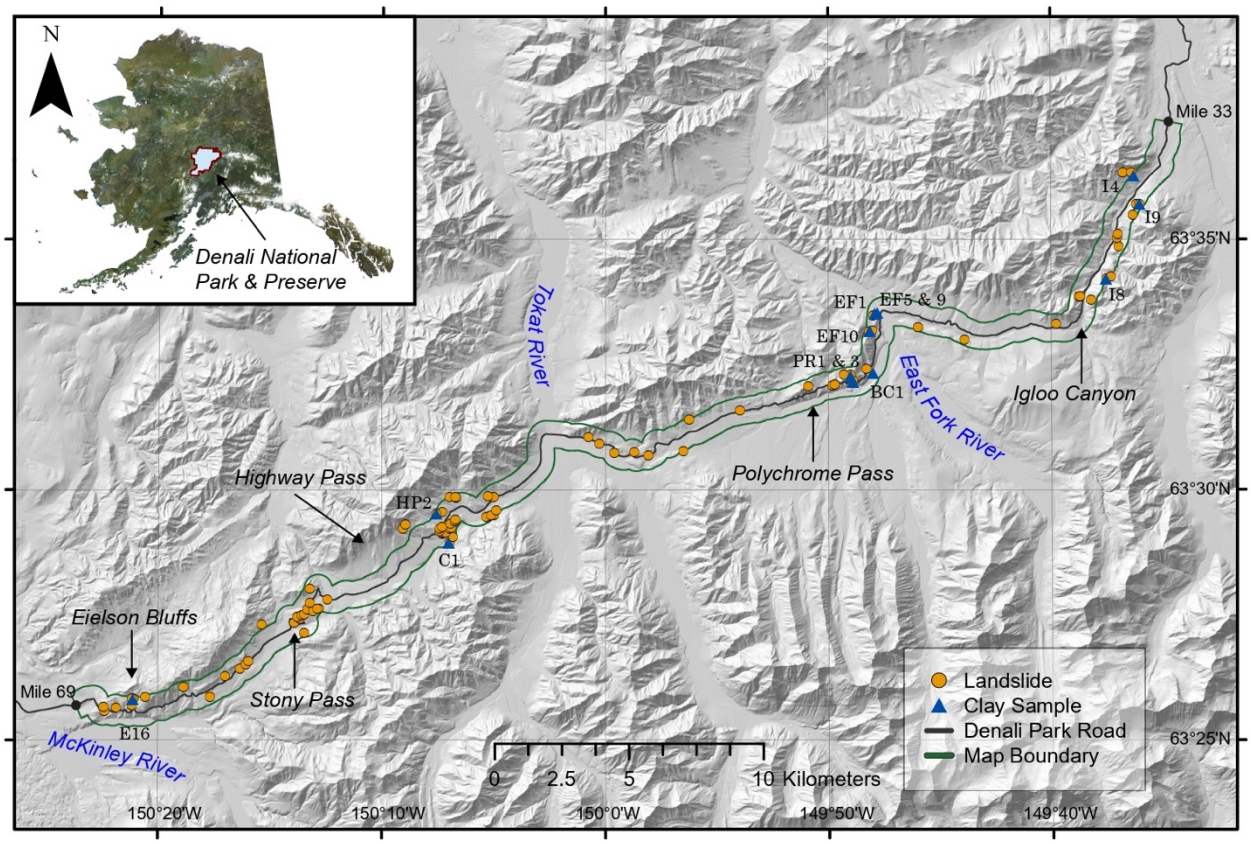

Figure 3.1. Study area within Denali National Park (DNP). Surficial geologic mapping was completed along the Denali road corridor from mile 33 to 66. Landslide scarp locations are shown as orange points, and clay sample locations and sample numbers described in the text are shown as blue triangles.

The high-relief topography of the Alaska Range is young, driven by rapid exhumation along the Denali fault system beginning 5-6 Ma (exhumation >1 mm/year) (Fitzgerald et al., 1993; Redfield and Fitzgerald, 1993) and the development of extensive valley glaciers during the last ice age and through the Pleistocene (Yeend, 1997). Quaternary dextral transpression along the Denali fault system continues to deform and exhume the high-relief topography of the Alaska Range (Haeussler et al., 2017). Seismicity in the Alaska Range contributes to landslide hazard: the McKinley strand of the Denali fault (south of the study area) is active at a slip rate of 7-12 mm/year (Benowitz et al., 2011). Until recently, the major strand of the Denali fault system within the study region, the Hines Creek fault, was considered inactive (Wahrhaftig et al., 1975;

Benowitz et al., 2011). Vertically offset alluvial fans and other Holocene deposits indicate that segments of this fault may still be active, with reverse motion along a north-dipping plane generating uplift at a rate of 0.7 mm/year in the Pleistocene (Koehler et al., 2015). Major strike-slip movement on the Hines Creek fault likely took place prior to 95 Ma (Wahrhaftig et al., 1975; Csejtey et al., 1982). Most of the primary lithologic units of the study area are therefore unlikely to be horizontally offset by movement along major terrane-bounding faults.

Current climate in northern DNP is typical of an interior Alaska landscape, with low annual precipitation (average 38 cm), cold winters (average 5.8 °F), and mild summers (average 53 °F) ("Denali National Park and Preserve"), although climate is highly variable over the large area of the park. Approximately 75% of DNP was underlain by near-surface permafrost in the 1950s, and 50% of DNP was underlain by near-surface permafrost at the beginning of this century (Panda et al., 2014). Permafrost is most prevalent at high elevations and in the low-relief terrain in the northern portion of the park.

3.2 METHODS

3.2.1 Surficial Geologic Mapping and Landslide Inventory

I conducted field mapping of surficial geologic units at 1:24,000 scale in the 1-km wide corridor along the Denali Park Road from miles 33-66 (Fig. 3.1, Supplementary Material Plate 1), building from unit designations in the existing literature, including work by Decker, (1975), Gilbert, (1979), Csejtey et al., (1992), and Yeend, (1997). Notably, this investigation dramatically improves the resolution of mapping in the study area and adds emphasis on surficial

units, distinguishing multiple glacial deposits, hillslope deposits, landslides, and alluvial units that were previously grouped in more general unit designations.

Surficial mapping efforts included a comprehensive inventory of identifiable (modern) landslides that occurred within the study area before August 2018. Landslide inventory data includes a mapped area, an initiation point designated near within the scarp, and a general failure style. Categories of style include rotational slides, debris flows, translational block slides, translational flows, active layer detachments, and combined failure mechanisms (Varnes, 1978; Cruden and Varnes, 1996; Hungr et al., 2014). Landslide initiation points were used to identify key geomorphic characteristics of each landslide for comparison with the entire study area, including underlying lithology, modeled permafrost presence and depth, elevation, slope aspect, slope angle, and hillslope curvature. Curvature was calculated using the ArcGIS planform curvature tool, described in the ESRI online tool reference (ESRI).

3.2.2 Landslide Distribution in Permafrost

Using the landslide inventory described above, I compared the distribution of landslides within the map area and the distribution of permafrost characteristics. Panda et al. (2014) modeled mean decadal ground temperature (°C) and active layer thickness within the national park using the GIPL 1.0 model at a spatial resolution of approximately 30 m^2. Permafrost characteristics in this model were derived using climate data, ecotype, soil characteristics, and snow characteristics, and were intended to represent permafrost conditions during the 2001-2010 decade. Negative active layer thickness values indicate that permafrost is not present, and instead describe seasonal frost thickness. Estimated error of the model used in this study is ±0.2-0.4°C for the mean ground temperatures and ±0.1-0.3 m for the active layer thickness. Using the

modeled permafrost extent developed for the previous decade (2001-2010), I evaluated both the ground surface temperature and active layer thickness (or seasonal frost thickness where permafrost is not present) at landslide sites and within the map area.

3.2.3 Clay Sample Collection and Analysis

Clay minerals influence the geotechnical properties of slope materials where in-situ weathering or hydrothermal alteration of bedrock promotes their development (Ikari and Kopf, 2011). I characterized the mineralogical composition of clay-rich sediment in landslides to evaluate the mechanism driving lithologic control on landslide initiation. I collected thirteen clay samples from mapped landslides where a significant volume of clay material was exposed in the scarp or within the landslide deposit. Clay samples were then dried and analyzed for mineral assemblage and chemical composition using a TerraSpec Halo multispectral mineral analyzer and mineral identification software.

3.3 RESULTS

3.3.1 Surficial Geologic Mapping

Surficial geologic mapping throughout the study area refined contacts and map resolution along the DNP road corridor (Fig. 3.2 and 3.3). In comparison with previous small-scale mapping efforts, this work distinguishes multiple units that were previously unmapped, grouped in more general units, or mapped in less detail. For example, I identify multiple glacial, alluvial, and hillslope deposits, including delineation of the currently active braid plain (Qbp), colluvium (Qcol), pediment (Qp), and relict landslide deposits (Qmw) (Table 1) that were previously

mapped together as alluvium/colluvium (Yeend, 1997). Furthermore, the geologic map differentiates exposures of the Mt. Galen Volcanics and Teklanika Volcanic units by lithology, including basalt, andesite, rhyolite, tuff, and tuff breccia where surface exposure of bedrock is adequate. Mapped lithologies are described in summary in Table 3.1. I also identified and refined the surface trace of several map-scale faults in the study area. Notably, topographic offset in Quaternary units suggests recent activity of a fault southeast of Eielson Bluffs (Figure 3.2) and I identified a previously unmapped oblique-sinistral fault that crosses the map area at the Polychrome Pass overlook (Figure 3.3). The complete 1:24,000 map is available in the Supplementary Material Plate 1.

Table 3.1. Summary of the primary lithologic units mapped in the study area. For simplicity, some units are grouped by type. Ages of units with ongoing deposition are listed as "modern." Where more specific units are distinguished on the map, unit symbols are included in the summarized description.

Unit Name	Symbol	Age	Summarized Description
Landslide	Qls	Modern	Recent landslide deposits where the entire landslide (scarp, transport zone, toe) is still distinguishable. Sediment is typically poorly sorted and angular. Landslides include multiple styles of failure, such as translational block sliding, back-rotational slumping, translational flow, and debris flow (Qdf).
Alluvium	Qal	Modern	Sorted, bedded sediment deposited by streams and rivers, including channel fill, floodplain sediment, gully fill, active braid plain sediment (Qbp) and recently active braid plain sediment (Qibp).
Alluvial fan	Qaf	Modern	Alluvial fan sediment, characterized by fan-shaped morphology and interfingering deposits from stream channels, floods, and debris flows.
Colluvium	Qcol	Modern	Diffusive mass wasting deposits on hillslopes, including talus slopes. Sediment is variable in size and is typically angular to subangular.
Pediment	Qp	Pleistocene-Holocene	Coalesced depositional aprons at the base of a mountain front. Sediment is poorly sorted and partially weathered. Incised channels indicate that pediment formation is no longer active.
Relict landslide deposit	Qmw	Pleistocene-Holocene	Discontinuous deposits from old landslides, where separate portions of the landslide (scarp, transport zone, toe), are no longer distinguishable. Sediment partially weathered, unsorted, and contains a variety of clast lithologies and rounding.
Glacial sediment	Qg	Pleistocene	Ice-related deposits from the preceding glaciations, including moraine deposits (Qgm), outwash (Qgo), and till. Most glacial units (Qg, Qgm) are unsorted and unstratified and are differentiated by topographic expression. Outwash (Qgo) is poorly sorted, stratified, and contains subrounded-rounded clasts. Clast lithologies include the volcanic and sedimentary units found in the study region.
Usibelli Group	Tu	Miocene	Fluvial pebbly sandstone and lacustrine mudstone with interbedded coal deposits. (Ridgway et al., 1999)
Mt. Galen Volcanics	Tmg	Late Eocene-Early Oligocene	Extrusive volcanic rocks including rhyolite (Tmgr), tuff breccia (Tmgtb), and andesite (Tmga) (Decker, 1975; Gilbert, 1979; Cole and Layer, 2000). The upper part of the formation is ~43 Ma based on one $^{40}Ar/^{39}Ar$ age (Cole and Layer, 2000).
Teklanika Volcanics	Tt	Paleocene	55-50 Ma bedded extrusive volcanic rocks including altered rhyolite (Ttr), andesite (Tta), and basalt (Ttb). Flow banding is present in some exposures (Gilbert et al., 1976; Gilbert, 1979). In the USGS lexicon, the Teklanika Volcanics unit is considered the upper member of the Cantwell Formation, though most regional-scale studies differentiate the two units.
Teklanika Basalt	Ttb	Paleocene	55-50 Ma aphyric basalt of the Teklanika Volcanics. Columnar jointing is common. Vesicles are present in some exposures (Gilbert et al., 1976; Gilbert, 1979).
Cantwell Formation	Kc	Late Cretaceous	Lithic sandstone and conglomerate; bedding in sandstone is 0.01-1 m thick. Conglomerate is mostly massively bedded. Clasts are sub-rounded to rounded and include quartz, quartzite, basalt, and other volcanic lithologies (Gilbert et al., 1976; Gilbert, 1979; Hickman et al., 1990).
Nikolai Formation	TRn	Middle-Late Triassic	Weathered porphyritic basalt; well-preserved pillow structures in some exposures. Often referred to as the Nikolai Greenstone, although basalts of this age in the map area have not undergone substantial regional metamorphism (Csejtey et al., 1982; Dusel-Bacon et al., 1993; Plafker et al., 1989; Wilson et al., 2015).

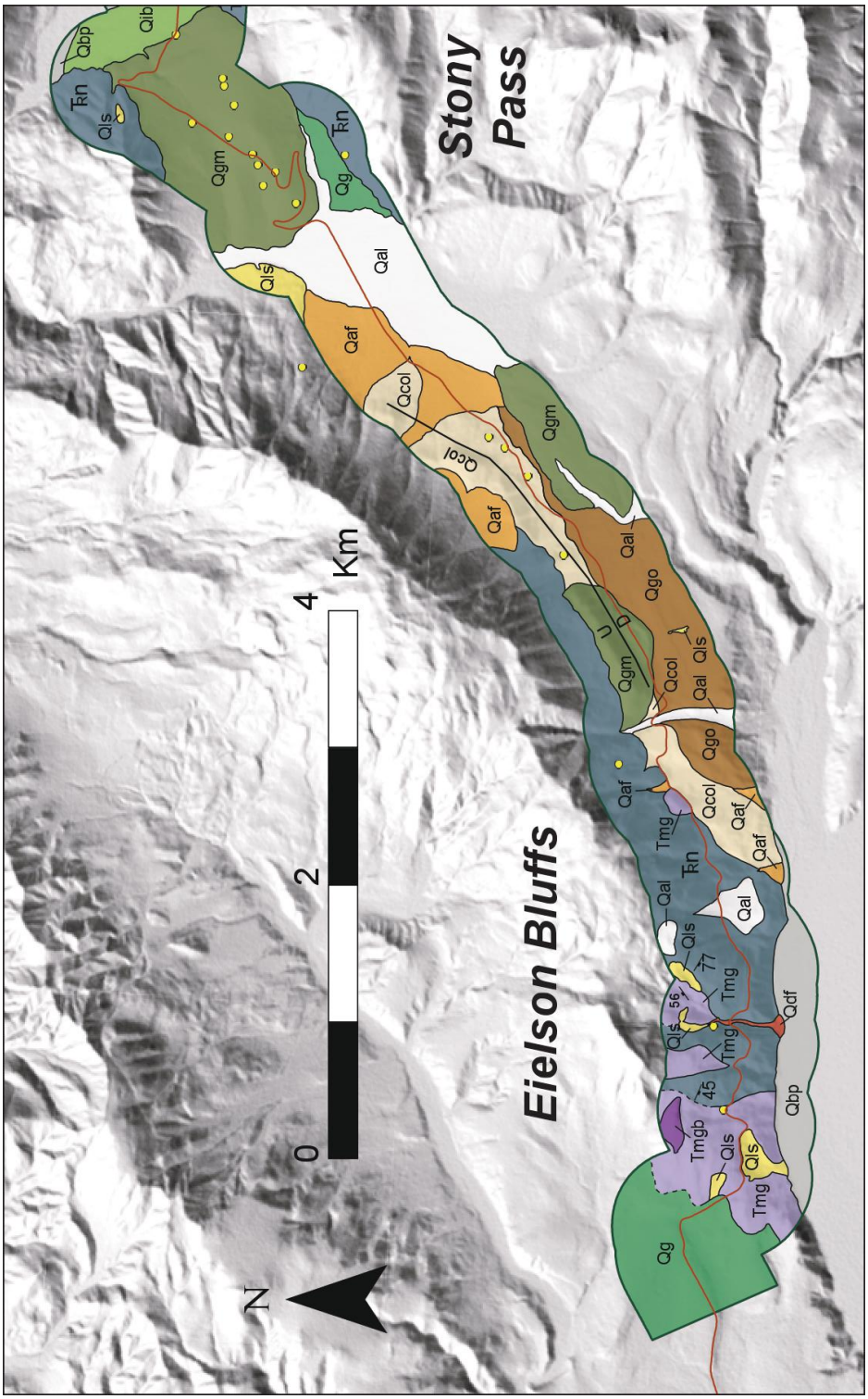

Figure 3.2. Sample geologic map of Eielson Bluffs, using standard geologic symbols and unit symbols as outlined in Table 3.1. Landslides are mapped as Qls (yellow) or as yellow dots where landslide size is too small to display. Prominent volcanic units in this area include the Mt. Galen Volcanics (Tmg) and Nikolai Formation (TRn). These volcanic formations generate multiple landslides. The complete 1:24,000 scale map is available in the Supplementary Material Plate 1.

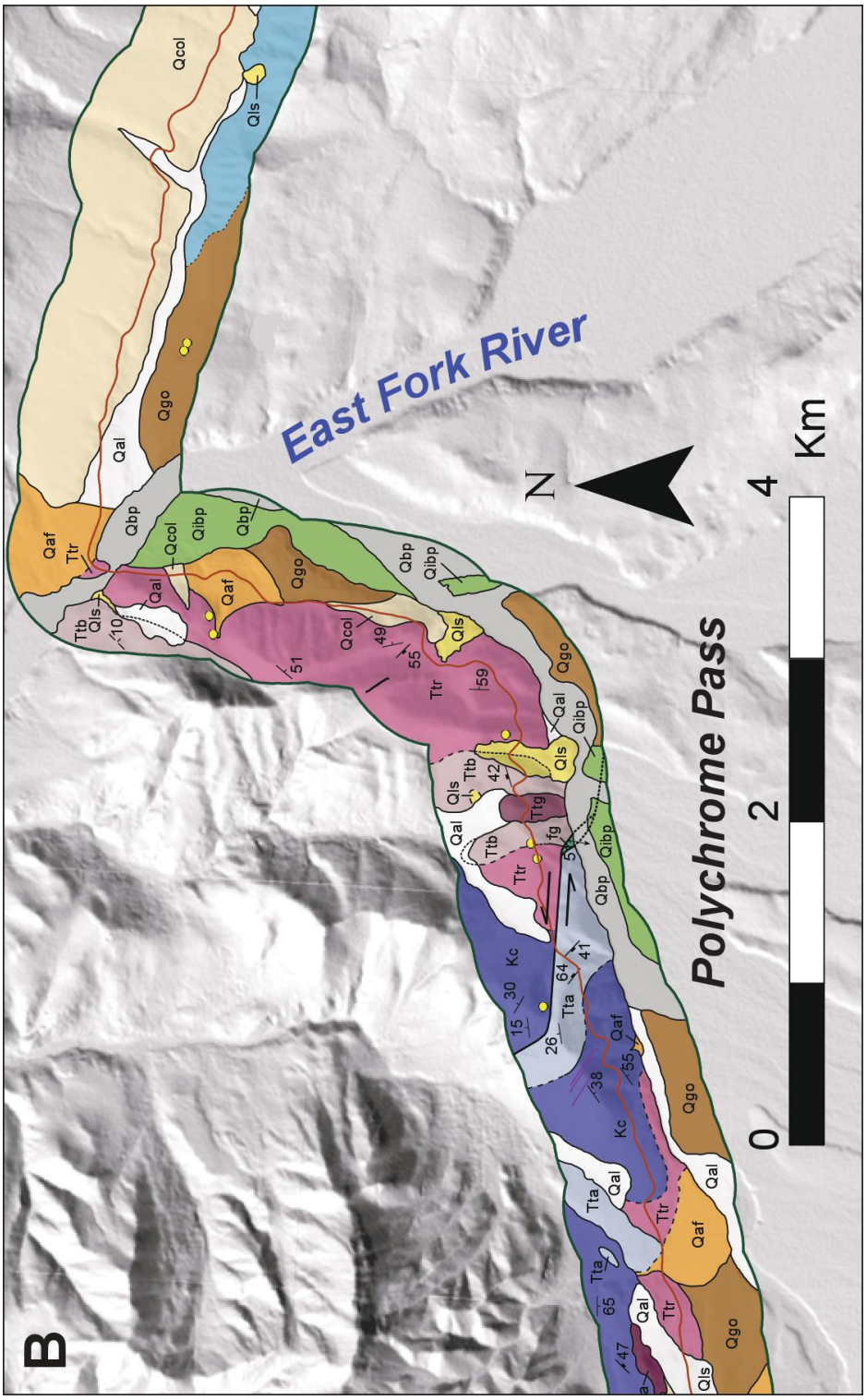

Figure 3.3. Sample geologic map of Polychrome Pass, using standard geologic symbols and unit symbols as outlined in Table 3.1. Landslides are mapped as Qls (yellow) or as yellow dots where landslide size is too small to display. Prominent volcanic units in this area include the Teklanika Volcanics rhyolite (Ttr) and basalt (Ttb). These volcanic formations generate multiple landslides. The complete 1:24,000 scale map is available in the Supplementary Material Plate 1.

3.3.2 Landslide Inventory

Landslides occur throughout the study area, although clusters of landslides occur in areas of greater relief, including (from west to east) Eielson Bluffs, Stony Pass, the Toklat and East Fork River valleys, and Igloo Canyon (Fig. 3.1). A total of 89 modern landslides were mapped in the study area, with 84 initiating within the map area (Appendix A). The majority of landslides in the study area are small in total surface area (Fig. 3.4); median landslide area is 0.20 km^2; 84% of inventoried landslides are less than 1 km^2; and 94% of inventoried landslides are less than 5 km^2. Planform curvature is similar between the landslide population and the map area, with mean curvature values near zero (0.068 ±0.83 and 0.023 ±0.78, respectively), indicating an even distribution of concave, convex, and planar hillslopes in both datasets. Landslides initiate on high-elevation slopes of all aspects (Fig. 3.5 and 3.6). The study area is biased towards south- and east-facing hillslopes because the park road follows the south-facing hillslopes of the Toklat, Stony Creek, and Thoroughfare river valleys. Landslide distributions follow the same trend of bias toward south-facing slopes. The distribution of slope angle of landslide initiation is bimodal, with peaks in landslide occurrence at approximately 18° and 28° (Fig. 3.5B). The Hartigan's dip test of unimodality (Hartigan and Hartigan, 1985) demonstrates the significance of the multimodality of landslide slopes, with a p-value of 0.03. Calculation of this dip test statistic does not depend on bin size. Kernel density estimation is shown as a black line, with dashed lines to indicate density peaks (Fig. 3.5C).

The majority of landslides inventoried initiated in unconsolidated sediments (Fig. 3.5C, 3.2, 3.3), including various glacial deposits (Qg), and relict landslide deposits (Qmw). Colluvium (Qcol) also generated a disproportionately large number of landslides relative to the total portion of the map area where colluvium occurred. Both of the felsic volcanic units mapped in the study

area, the Teklanika rhyolite (Ttr) and the Mt Galen Volcanic unit (Tmg), also generated a disproportionately large number of landslides relative to the total portion of the map area underlain by these volcanic units.

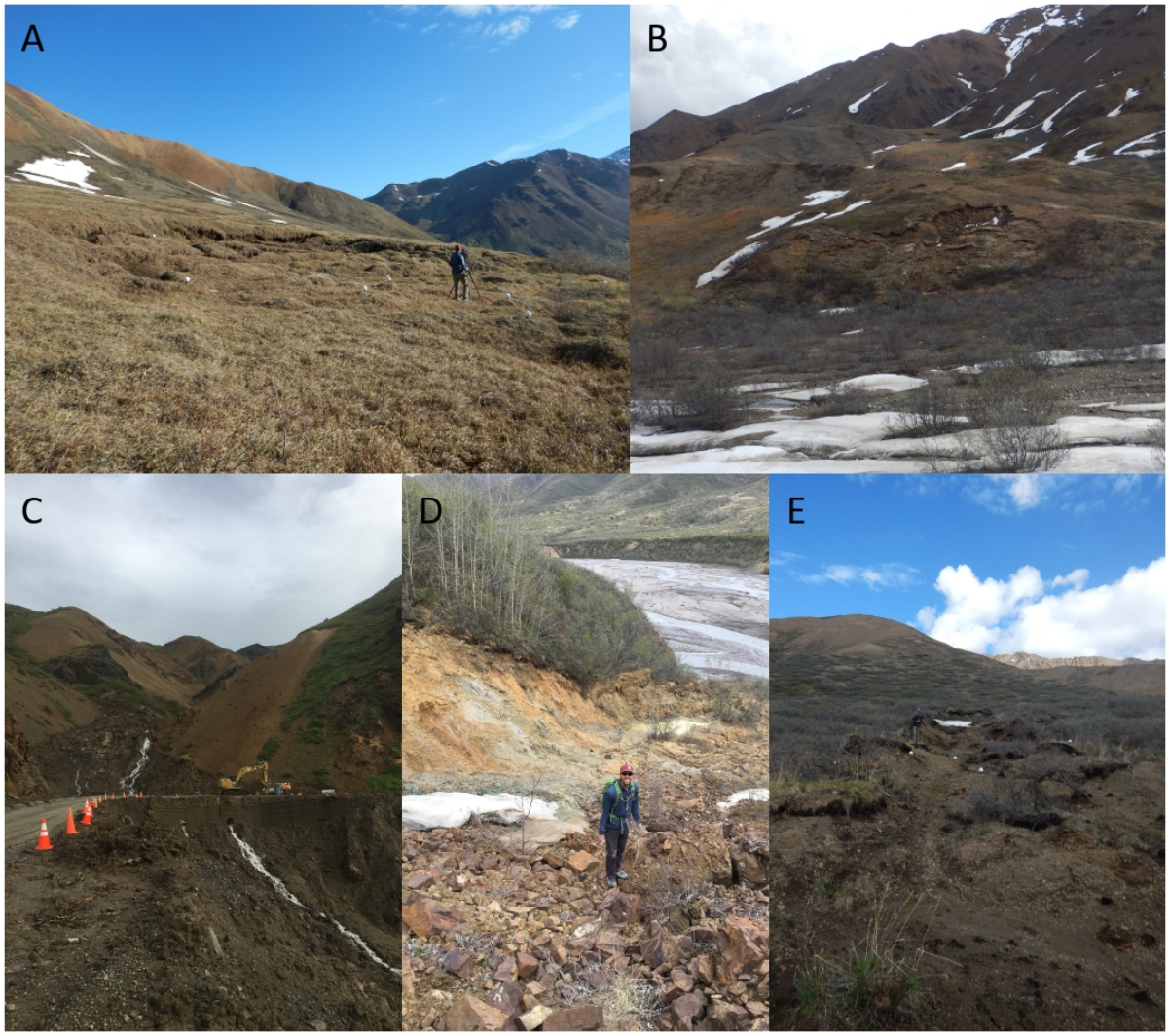

Figure 3.4. Notable landslides inventoried in the study area. A) Retrogressive rotational slide near Stony Pass; B) Rotational slide near Highway Pass; C) The "Eagle's Nest Landslide"; a complex landslide that initiated in August 2016 and blocked the road for several days; D) Debris slide on the East Fork River; E) The "Ptarmigan Landslide," an active layer detachment east of the Toklat River that likely occurred in July 2016.

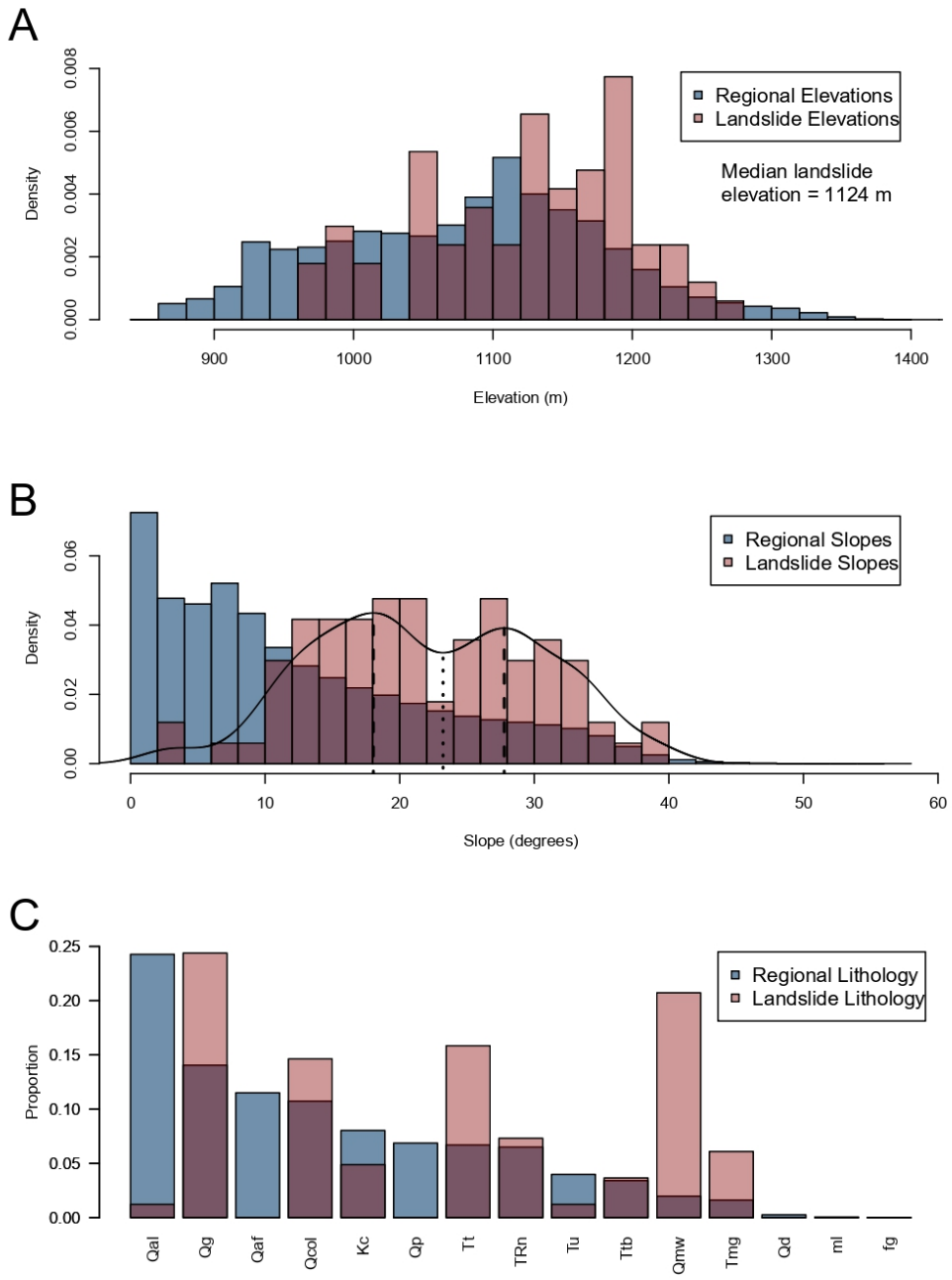

Figure 3.5. Histograms of landslide characteristics, showing the elevation, slope angle, and underlying lithologic unit relative to that of the study area. (A and B) The regional distribution of elevations and slope angles (blue) were extracted from a 5 m IFSAR-based Digital Terrain Model (DTM) of the road corridor from the area defined as the "study area." The distribution of elevations and slope angles, and underlying lithology for landslides (red) includes n = 84 landslides that initiated within the study area. Kernel density estimation of the landslide slope data is shown as a black line, with dashed lines showing density peaks. (C) The proportion of landslides that initiated within lithologic classes relative to the total proportion of the map area where the same units occur at the surface. The regional proportions (blue) are based on the

surficial geologic map produced in this study. The proportions of landslides that occur within each unit (red) includes n = 82 landslides that initiated within the study area in a single identifiable map unit. Lithologic unit symbols are described in Table 1; notably Tt here includes both rhyolite and andesite exposures of the Teklanika Volcanics, but Teklanika Basalt exposures are distinguished as Ttb.

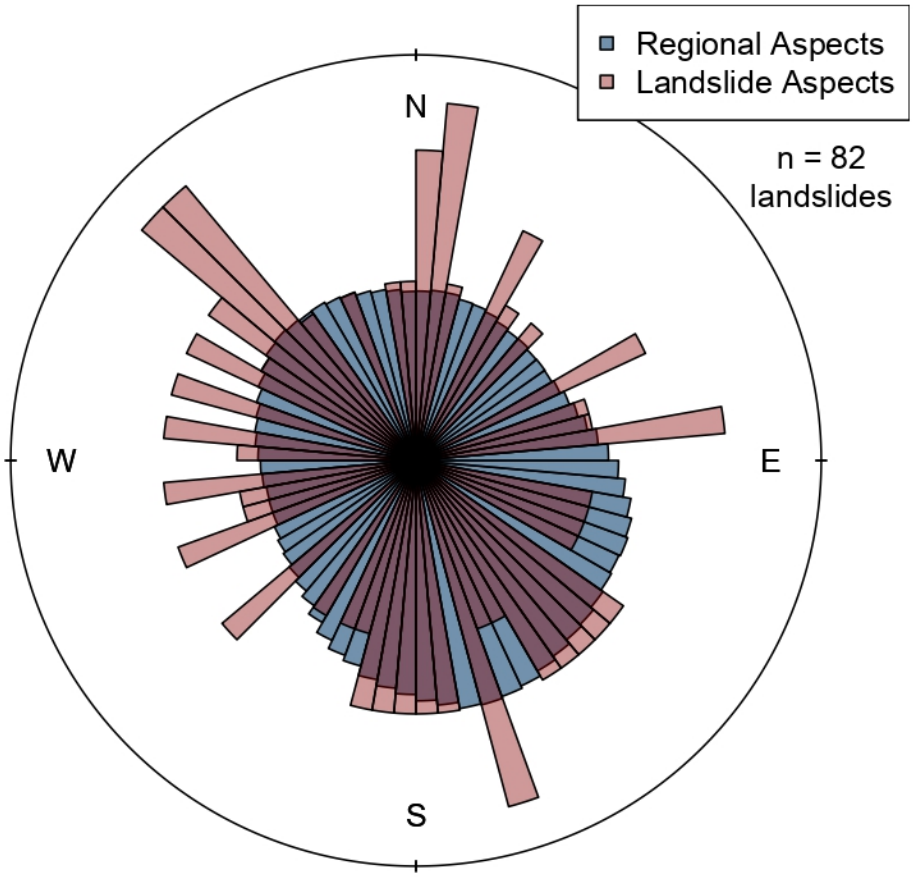

Figure 3.6. Rose diagram showing the distribution of azimuthal aspect of hillslopes where landslides initiated relative to that of the study area. The regional distribution of hillslope aspects (blue) was extracted from the 5 m DEM of the road corridor from the area defined as the "study area." The distribution of hillslope aspects for landslides (red) includes n = 84 landslides that initiated within the study area.

3.3.3 Landslide Distribution in Permafrost

As modeled by Panda et al. (2014), permafrost extended across 62% of the map area in the previous decade, with a mean surface temperature of -0.09 °C and a median active layer thickness of 0.94 m in the study area (Fig. 3.7). Landslides mapped in this study occurred preferentially in modeled permafrost terrain of Panda et al. (2014) (Fig. 3.8); 75% of landslides initiated in permafrost, with a mean surface temperature of -0.21 °C and a median active layer thickness of 0.97 m at initiation sites. Notably, a disproportionate majority of landslides occurred where modeled active layer thickness is approximately 1 m. Furthermore, slope angles of landslides that occur within permafrost terrain are lower than slope angles in landslides where seasonal thaw occurs (Fig. 3.9). Median slope angle of landslides in permafrost is 20.1°, compared to a median 27.1° slope angle of landslides that occur in seasonally thawed substrate.

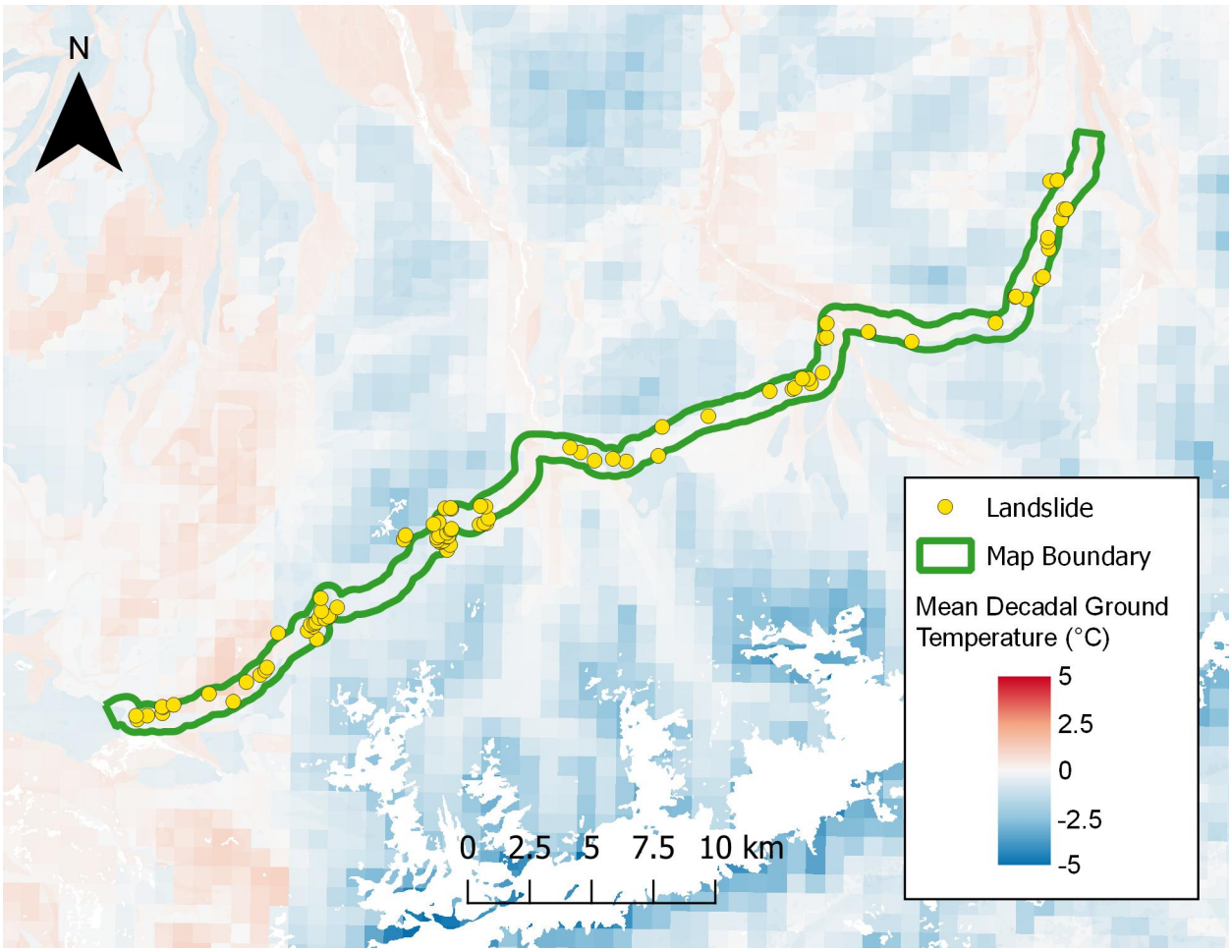

Figure 3.7. Map of mean decadal ground temperature (MDGT) and landslide points in the study area, using temperature data modeled by Panda et al. (2014) for the 2001-2010 decade.

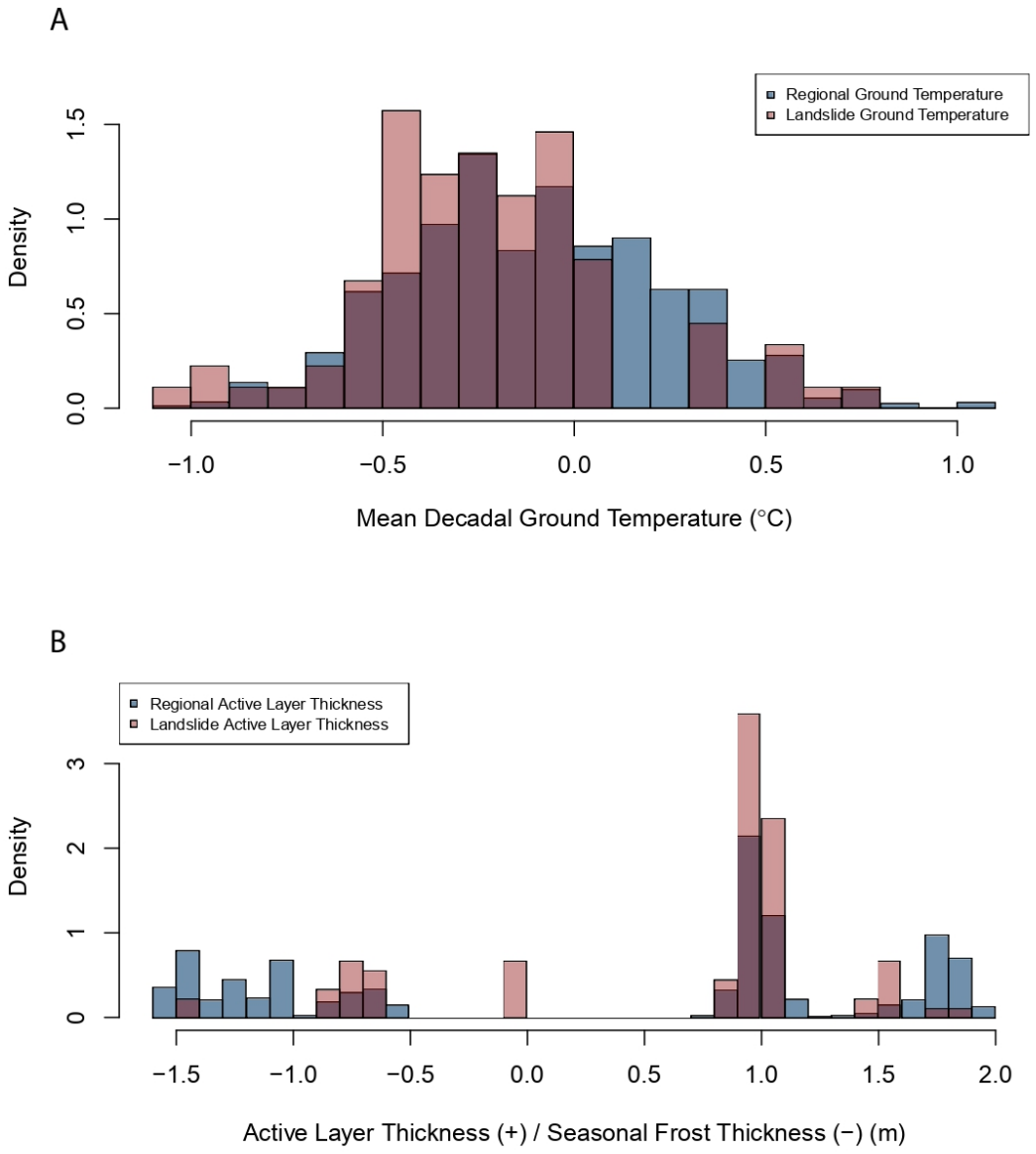

Figure 3.8. Histograms showing permafrost characteristics within the map area (blue) and at landslide initiation sites (red), including n = 84 landslides within the study area. Mean decadal ground temperature and active layer thickness values are modeled permafrost characteristics (Panda et al., 2014) based on climate data, ecotype, soil characteristics, and snow characteristics. Negative active layer thickness values indicate that permafrost is not present, and instead describe seasonal frost thickness.

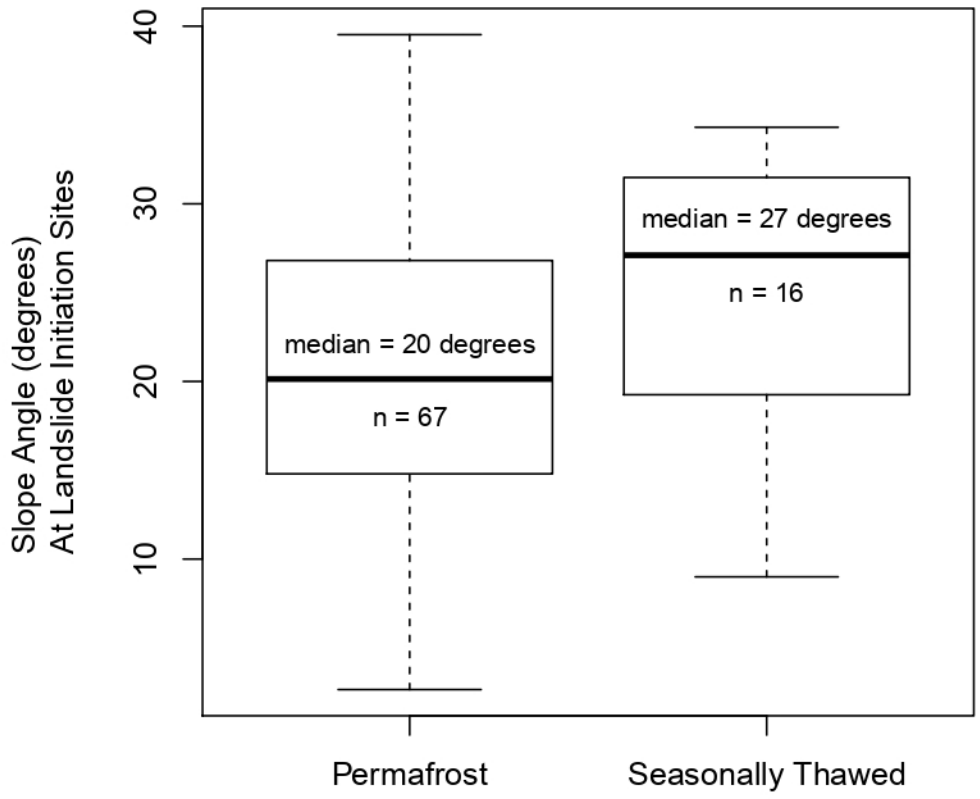

Figure 3.9. Distribution of slope angles of landslide initiation sites in permafrost compared to that of landslides on seasonally thawed hillslopes. The presence or absence of permafrost was determined using the Panda et al. (2014) model of permafrost distribution the study region. Box hinges show the interquartile range (first and third quartile), with a dark line showing the median. Whiskers indicate the minimum and maximum value of each population.

3.4.4 Clay Composition and Weathering History

Clay samples collected from modern landslide deposits (Fig. 3.10) include primarily 2:1 smectite minerals (montmorillonite, beidellite), and vermiculite (Table 3.2). Additional analysis is described in Appendix B.

Table 3.2. Minerals identified in each clay sample using the TerraSpec Halo multispectral mineral analyzer, along with the underlying unit identified in the field and the relative confidence provided by the instrument (1-3, where 3 indicates high confidence) of the mineral identification. Samples with an asterisk indicate high confidence that the underlying unit is the parent material and that it has locally near-homogenous composition. Scanning Electron Microscopy images are shown for samples EF1 and PR1 (Fig. 3.9).

Sample	Underlying Unit	Most prevalent minerals	Latitude (N), Longitude (W)
BC1*	Teklanika Rhyolite	Montmorillonite (3) Pyrophyllite (3) Rectorite (2)	63.53921, -149.80025
EF1*	Teklanika Rhyolite	Montmorillonite (3) Vermiculite (3)	63.55920, -149.79727
EF9*	Teklanika Rhyolite	Montmorillonite (3)	63.55324, -149.80269
EF10*	Teklanika Rhyolite	Hematite (3) Montmorillonite (3) Phlogopite (2)	63.55324, -149.80269
I4*	Teklanika Rhyolite	Illite/smectite (3) Rectorite (3)	63.60458, -149.60440
PR1*	Teklanika Rhyolite	Montmorillonite (3) Beidellite (3)	63.53639, -149.81511
PR3*	Teklanika Rhyolite	Montmorillonite (3) Beidellite (3)	63.53821, -149.81682
E16*	Mt. Galen Andesite	Montmorillonite (3) Vermiculite (3) Pyrophyllite (2)	63.43032, -150.35215
I8*	Teklanika Basalt	Montmorillonite (3) Fe/Mg chlorite (3)	63.57026, -149.62550
C1	Relict Landslide	Ferrihydrite (3) Montmorillonite (3) Fe smectite (2) Goethite (2)	63.48286, -150.11713
HP2	Relict Landslide	Ferrihydrite (3) K illite (3) Halloysite (2)	63.49258, -150.12645
EF5	Teklanika Fm.	Montmorillonite (3)	63.55906, -149.79874
I9	Teklanika Fm.	Ferrihydrite (3) Halloysite (3) K illite (3)	63.59526, -149.60070

Almost all of the minerals present in clay samples are typical of hydrothermal alteration of volcanic rocks and subsequent interaction with groundwater. The presence of montmorillonite and beidellite (smectite minerals) in most samples indicates formation of clay minerals in alkaline conditions with persistent groundwater (Anthony et al., 2001). A common weathering product of tuff and ash, montmorillonite in DNP may form within glassy felsic flows or minor

ash beds along bedding (flow) contacts, such as those identified by park staff (Frothingham and Capps, 2018). Similarly, vermiculite is common at the contact between felsic and mafic rocks, such as the prevalent contacts between Teklanika Volcanics rhyolite and basalt (Gilbert, 1979). The presence of clay minerals including rectorite and halloysite is consistent with clay minerals that form due to the weathering of feldspars (esp. potassic feldspars) (Anthony et al., 2001).

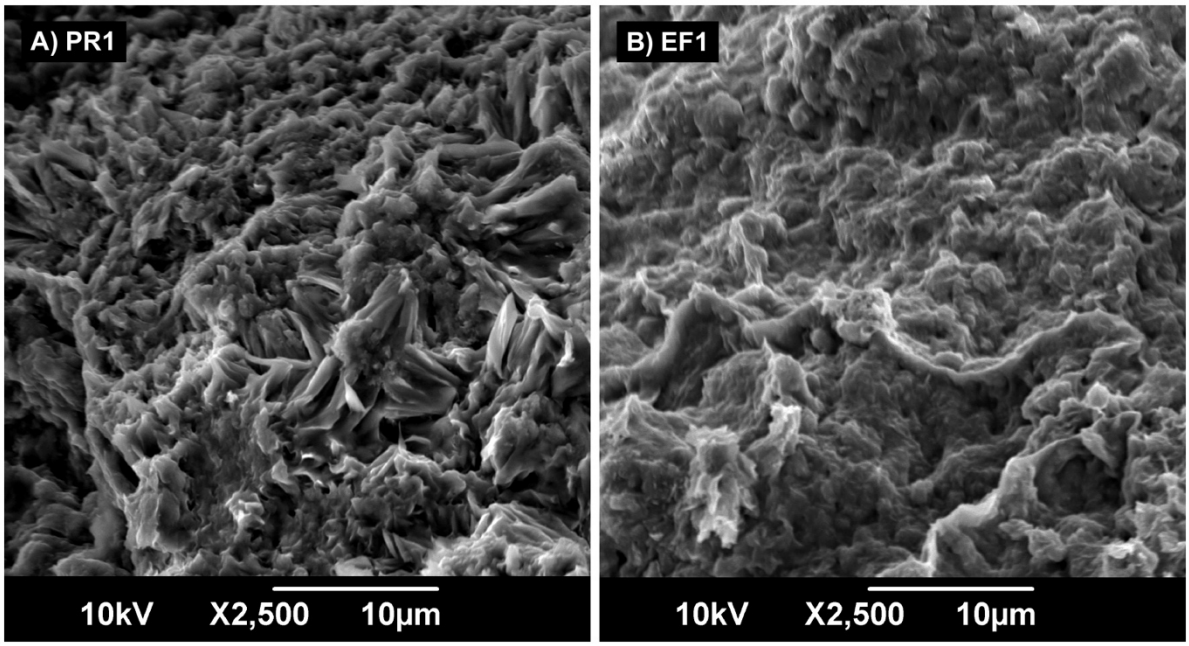

Figure 3.10. SEM images of samples collected from landslides near Polychrome Pass (Fig. 3.1). A) Sample PR1, which contains montmorillonite and beidellite. B) Sample EF1, which contains montmorillonite and vermiculite.

3.4 DISCUSSION

3.4.1 Geologic Mapping and Landslide Inventory

The surficial geologic map produced in this study improves the resolution of available geologic data along the DNP road corridor, providing a valuable resource for understanding landslide controls in diverse lithologies and areas of permafrost degradation. The extensive

landslide inventory conducted within the map area provides a census of all modern landslides that occurred before fieldwork was completed in August 2018. Characterization of this population is therefore representative of the map area and typifies spatial patterns of landslide initiation in the northern Alaska Range and other high-latitude mountain ranges with similar climate, topography and diverse underlying geology. This dataset will also allow for future landslide inventories to evaluate changes in landslide frequency and magnitude in future decades. Specifically, comprehensive information about landslide location, surface area, and type at a known time (August 2018) provides a baseline for future landslide inventories and time-series analysis. Such monitoring will provide a valuable insight into the many mechanisms by which climate change influences landslide initiation (e.g. Gariano and Guzzetti, 2016; Patton et al., 2019).

Within the DNP road corridor, landslide distribution indicates several important geomorphic controls on slope failure. Landslides occurred on all slope aspects throughout the study area, primarily at relatively high elevations (>1050 m) where topographic relief is greatest (Fig.3.5 and 3.6). The majority (84%) of landslides within the study area are less than 1 km^2 in area, indicating that small, frequent hazards are a significant source of concern in the region. Larger landslides, though present within the map area and beyond, are likely infrequent.

The bimodal distribution of slope angles in the study area indicates that there are two primary drivers of landslide failure within discontinuous permafrost zones: atmospheric events (snowmelt or rainfall) that saturate the subsurface and permafrost thaw. On steep hillslopes ($\geq$ 20°), landslides occur according to well-established patterns, particularly when rainfall or snowmelt increases soil saturation beyond threshold limits (e.g. Borga et al., 2014) and/or seismic activity reduces cohesion (e.g. Kargel et al., 2016). Landslides that occur on shallow

hillslopes require substantially lower shear strength due to low cohesion or friction (Milledge et al., 2014). Many of the shallow-angle landslides mapped in Denali National Park were characterized as active layer detachments, which typically occur where melting of ice lenses at the base of the active layer reduce shear strength and allow landslides to occur on shallow (10°-20°) hillslopes (Lewkowicz and Harris, 2005b; Lewkowicz, 2007; Blais-Stevens, Kremer, et al., 2015).

Landslides occurred throughout the study area and in almost all of the mapped units, except those that are inherently characterized by very shallow slope angles (e.g. alluvial sediment and pediment). Most landslides occurred in unconsolidated sediments (e.g. glacial deposits, colluvium, and relict landslide deposits) or felsic volcanic units (e.g. rhyolite and andesite of the Teklanika and Mt. Galen volcanic units). This pattern suggests that landslides throughout the Alaska Range and similar climatic zones are most likely to occur where low-cohesion unconsolidated material is available or where alteration of volcanic rocks produces sufficient clay content to reduce rock/soil strength, as discussed below (Behnsen and Faulkner, 2012; Torrence, 2014; Isobe and Torii, 2016). Notably, many of the unconsolidated units in the study area contain high concentrations of volcanic detritus.

Assuming that the map area is representative of other regions with similar climate, topography and diverse lithology, landsliding in discontinuous permafrost may be separated into two categories: atmospherically driven vs. ice-rich-permafrost-thaw driven. Increased rainfall intensity is likely to increase landslide frequency in upcoming decades (Stoffel et al., 2014; Gariano and Guzzetti, 2016). Ice-driven landslides are likely to become more frequent in upcoming decades (Patton et al., 2019), resulting in frequent small landslides. Due to the typically small size and relatively slow flow speeds of active layer detachments (Lewkowicz,

2007), these types of landslides are likely to result in infrastructure damage but are unlikely to pose serious hazards to human safety on a large scale. Loss of permafrost, which may allow more deep-seated landslides to initiate (Harris et al., 2009; Keiler et al., 2010), is likely to increase the magnitude of landslides in this and other regions experiencing permafrost thaw (Patton et al., 2019). The combined effect of permafrost loss and rainfall-driven landsliding on steep slopes is likely to result in larger and more hazardous landslides (Geertsema et al., 2006) throughout the Alaska Range, posing significant concerns for human safety and infrastructure stability.

3.4.2 Landslide Distribution in Permafrost

A disproportionate number of landslides (75%) initiated in permafrost terrain relative to the 62% of the map area underlain by permafrost (mean decadal surface temperature < 0 °C). This discrepancy demonstrates the influence of (ice-rich) permafrost in landslide initiation. Furthermore, median slope angles where landslides occur are 7° lower in permafrost terrain, demonstrating the ability for ice-rich permafrost to facilitate landslide initiation on shallow hillslopes due to perched groundwater (Walvoord and Kurylyk, 2016b) and low cohesion and friction along permafrost boundaries (Haeberli et al., 1997; Huggel, 2009). The majority of landslides within the study area initiate on slopes where active layer thickness is approximately 1 m. I postulate that ~1 m active layer thickness is a threshold depth of material to generate sufficient shear force along the low-cohesion permafrost boundary.

It is important to note that the permafrost parameters used in this comparison were calculated for the previous decade (2001-2010). While this time frame likely describes active layer depth and temperature of the study area when many of the inventoried landslides initiated,

based on partial re-vegetation of some of the surveyed landslides, some landslides have occurred several years after the time frame of this model. For example, eyewitness accounts constrain initiation of multiple inventoried landslides within the last five years, including the Eagle's Nest Landslide (Fig. 3.4C), which occurred in August 2016 and the Ptarmigan Landslide (Fig. 3.4E), which likely occurred in July 2016. Although average ground temperature at landslide initiation sites was slightly lower than the regional average (-0.21 °C and -0.09 °C, respectively), both mean temperatures are very near the 0 °C freezing threshold, indicating that in the previous decade permafrost was already unstable. Given this context, it is likely that ongoing permafrost thaw has increased landslide initiation within the study area, allowing landslides to occur along partially melted ice boundaries.

3.4.3 Clay Formation and Slope Stability

Montmorillonite, beidellite, and vermiculite are the most prevalent clay minerals present in the 13 samples. Sample I8, most likely derived from basalt, also contains measurable FeMg chlorite. These specific mineral assemblages indicate a saturated, alkaline weathering environment, consistent with the modern subsurface characteristics of discontinuous permafrost zones (Walvoord and Kurylyk, 2016b). Although the effect of climate on clay composition generally overwhelms other factors (Velde and Meunier, 2008), the minerals present also indicate generalized characteristics of the parent material. The primary minerals identified in my samples are typical of weathering feldspars and felsic volcanic rocks; contacts between felsic and mafic volcanic rocks; and tuff or glassy felsic flow deposits (Anthony et al., 2001). These environments are consistent with the sequences of volcanic rocks in both the Mt. Galen and

Teklanika formations, where felsic lithologies and complex contact relationships provide ample opportunity for montmorillonite, vermiculite, and other clay minerals to develop.

Clay weathering products are an important control on landslide susceptibility by impeding groundwater flow and increasing local pore pressure (Badger and Ignazio, 2018) and reducing rock strength (Bittelli et al., 2012; Borrelli and Gullà, 2017). Expansive clays (smectites and vermiculites, as identified in my samples) may even trigger landslides in response to changes in soil saturation (Velde and Meunier, 2008; Bittelli et al., 2012; Isobe and Torii, 2016). In most crustal rocks coefficients of friction range from 0.6-0.85 (Byerlee, 1978). Empirical data suggest that the coefficients of friction of most clay minerals are much lower, ranging from 0.12 (montmorillonite) to 0.38 (illite) when samples are wet (Behnsen and Faulkner, 2012). This reduction in friction can dramatically reduce slope stability where alteration increases clay content in bedrock. At a mechanistic level, weathering of felsic volcanic rocks and the production of clay minerals has the potential to reduce shear strength of bedrock slopes below thresholds of stability. The high clay content in landslide deposits, including abundant low-strength, expanding clay minerals (e.g. montmorillonite), explains the disproportionate number of landslides that initiated in felsic volcanic units in DNP. Permafrost thaw in clay-rich substrate will likely exacerbate the existing susceptibility of clay-rich slopes to slope failure.

Weathered volcanic sequences in other areas of the world are also susceptible to landsliding, particularly where clay weathering products are abundant. Hydrothermal alteration of volcanic rocks in an active volcanic complex in Ecuador likely contribute to the initiation of clay-rich debris flows (Detienne et al., 2017). In 2005, a complex landslide (Sutherland Landslide) in British Columbia occurred in a lithologic setting that is remarkably similar to the Mt. Galen and Teklanika Formations (Blais-Stevens, Geertsema, et al., 2015). The Sutherland

Landslide initiated on a hillslope where a relatively resistant Eocene basalt sequence capped a weaker felsic and volcaniclastic sequence. Clay samples collected from the landslide included abundant smectite-group minerals including montmorillonite, located stratigraphically above saturated volcaniclastics. Blais-Stevens and others suggest that weathered ash and/or feldspar provided the primary source material for the clay minerals and that expandable clays formed the primary slip plane of the Sutherland Landslide (2015). The global occurrence of landslides in weathered felsic volcanic units suggests that clay alteration products contribute to slope susceptibility in diverse geographic settings.

3.4.4 Future Work

Key research needs to advance knowledge of landslide initiation in high latitude regions include:

- Expansion of high-resolution surficial mapping beyond the road corridor, including the ongoing work by the USGS.
- Expansion of monitoring systems to measure in-situ subsurface temperature and soil moisture. Direct measurements of subsurface temperature profiles within DNP could be used to ground-truth and update existing permafrost models.
- Detailed sampling of rock and weathering products for the purpose of identifying gradients of alteration within the map area, particularly along fractures and lithologic boundaries.
- Characterization of the relationship between degree of alteration/proportion of clay minerals and hillslope stability in interior Alaska. Describing this relationship would determine whether landslide susceptibility increases linearly with degree of alteration or if a threshold of alteration controls landslide occurrence.

3.5 CONCLUSIONS

Within the study area, landslides occur primarily on high-elevation hillslopes on all slope aspects. The bimodal distribution of slope angles where landslides initiate in the study area indicates two primary failure mechanisms in discontinuous permafrost regions, including atmospheric events and permafrost/ice thaw. Landslides in the study area preferentially initiate in areas underlain by permafrost, and landslides in permafrost terrain occurred on slope angles approximately 7° shallower than landslides on seasonally thawed hillslopes. Modeled mean decadal ground surface temperatures were very near 0 °C for the previous decade, and thaw of sensitive permafrost provides a likely mechanism to reduce cohesion and allow landslides to develop on relatively low slope angles. Shallow-angle landslides (<20° slopes) in permafrost demonstrate that permafrost/ice thaw is an important triggering mechanism. Melting permafrost reduces shear strength by lowering cohesion and friction values along ice boundaries. Increased permafrost degradation associated with climate change will make this and other high-relief areas more susceptible to shallow-angle landslides.

Unconsolidated units, including colluvium and glacial deposits, generate the largest numbers of landslides, and generate more landslides than would be predicted by area alone. Felsic volcanic rocks also generate a disproportionate number of landslides due to the significant weathering of feldspars and glassy matrix to clay minerals (particularly montmorillonite, vermiculite, and beidellite). The presence of clay minerals may promote landslide initiation by impeding groundwater flow and increasing local pore pressure, reducing rock strength and reducing friction. The presence of swelling clays may even trigger landslides in response to changing saturation.

With expected rapid climate warming and subsequent permafrost thaw, landslide hazards pose an ongoing management challenge within DNP and in discontinuous permafrost regions worldwide. The refined geologic map provides a framework for ongoing monitoring and identifying susceptible lithologies and slope characteristics that require attention and maintenance. The high-resolution geologic map of the Denali road corridor provides detailed geologic information about significant resource for park staff and visitors. The comprehensive inventory of modern landslides in the road corridor up to August 2018 provides a baseline dataset for comparison of future landslides and time-series analysis of landslide frequency in the Alaska Range.

4. LANDSLIDE DEVELOPMENT IN THAWING PERMAFROST, DENALI NATIONAL PARK, ALASKA[3]

4.1 INTRODUCTION

Thawing permafrost influences the cohesion, friction, and groundwater dynamics of near-surface materials and can therefore have a profound impact on landslide process (Rist, 2008; Huggel, 2009; Shan et al., 2014; Walvoord and Kurylyk, 2016, Patton et al., 2019). Permafrost loss is particularly rapid where ground temperatures are already near 0° C, such as in the discontinuous permafrost in interior Alaska (Osterkamp et al., 2009; Panda et al., 2014). These sensitive regions are subject to accelerated climate warming observed at high latitudes (Intergovermental Panel on Climate Change (IPCC), 2014; Francis et al., 2017; Blunden and Arndt, 2017). Other factors that contribute to permafrost sensitivity to thaw include ground surface disturbance, which facilitates heat flux between the subsurface and atmosphere (Khak and Kozyreva, 2012; Wang et al., 2014), and loss of vegetation (Nauta et al., 2014). Increased occurrence of landslides in high-latitude areas is likely to continue as permafrost degrades (Gariano and Guzzetti, 2016).

In particular, shallow-angle landslides are likely to become more frequent during the transition period as permafrost thaws. Active-layer detachments slides (ALDs) are shallow-seated translational landslides that occur in the thawing layer above permafrost (Lewkowicz and Harris, 2005b). Low cohesion, low friction, and high saturation along the permafrost-active layer boundary allow ALDs and other landslides to occur even on very shallow (1-20°) hillslopes (Leibman, 1995; Lewkowicz, 2007, Patton et al., In Revision).

[3] Chapter in preparation as Patton, A. I., Rathburn, S. L., Capps, D. M., McGrath, D., Brown, R. A., Landslide development in thawing permafrost, Denali National Park, Alaska, *Landslides.*

Although shallow-seated ALDs typically do not displace large volumes of material, their frequency and broad spatial distribution result in a large cumulative impact on the landscape. Repeat landslide inventories in northern Canada document ALD frequencies of 2.6-6.2 landslides per year in a 12 km^2 study area before 1975 and 12.6-14.6 landslides per year in the same 12 km^2 study area from 1975-2000 (Lewkowicz and Harris, 2005a). A landslide inventory along the Yukon Alaska Highway corridor documented 1,600 landslides in the 22,000 km^2 study area, 3% of which were shallow-angle permafrost/thaw-related landslides (Blais-Stevens, Kremer, et al., 2015). Landslide mapping in the Denali National Park road corridor identified ten ALDs within the 54.8 km^2 study area (Patton et al., In Revision). These small landslides pose persistent hazards and have the potential to cause costly cumulative damage to infrastructure (Capps et al., 2017).

A majority of the current body of geomorphic literature focuses on large-magnitude landslides driven by atmospheric events, including those that follow wildfire. Landslides in relatively low-relief topography (0-20° slopes) are not as well understood. Mapping efforts and landslide data provide important insights into the initiation and spatial distribution of shallow-angle permafrost landslides. For example, existing literature documents and describes shallow-angle landslides and ALDs in several high-latitude regions (Leibman, 1995; Lewkowicz and Harris, 2005b; Lewkowicz, 2007; Leibman et al., 2014; Khomutov and Leibman, 2014). In the Yukon Alaska Highway corridor, susceptibility to initiation of shallow-seated landslides in discontinuous permafrost terrain is controlled by thaw rate (Lewkowicz and Harris, 2005a), slope angle, slope aspect, surficial geology, vegetation, and proximity to surface water (Blais-Stevens, Kremer, et al., 2015). Similar to other types of landslides, lithology may also be an important control on ALD initiation (Patton et al., In Revision). These studies provide a framework to infer

the mechanisms that drive landslide processes in permafrost systems, but direct observation of the unique mechanisms that control landslide initiation and development in permafrost terrain is limited. In particular, local-scale controls on rates of landslide deformation are poorly understood. For example, observed spatial variability in deformation rate of thaw features in the Lena Delta, Siberia, are poorly correlated with macro-scale topography (e.g. slope aspect), indicating that local geomorphic conditions, such as ground ice and soil properties, are important controls on landslide development (Zwieback et al., 2018). Furthermore, the rate of movement at thaw slumps is often limited by available heat energy, although factors such as precipitation and surface insulation by snow or debris are also important (Zwieback et al., 2018). This study documents deformation rates of three shallow-seated landslides in interior Alaska and characterizes permafrost conditions to more directly observe the development of permafrost landslides over time.

4.1.1 Study area

To evaluate the mechanisms and rates of deformation of small landslides in thawing permafrost, I characterized topographic change and permafrost conditions at three small, shallow-angle landslides in Denali National Park (DNP), Alaska (Fig. 4.1). The current climate in northern DNP is typical of interior Alaska, with low annual precipitation (average near 38 cm), cold winters (average near 5.8 °F), and mild summers (average near 53 °F) (Denali National Park and Preserve, 2018), although climate is variable over the large area of the park. Approximately 50% of DNP was underlain by discontinuous permafrost at the beginning of this century (Panda et al., 2014). Permafrost is thawing rapidly in this and other discontinuous permafrost regions; permafrost models predict that by the end of the century, less than 1% of the

park will be underlain by permafrost (Panda et al., 2014) and 40-60% of permafrost by area will be lost throughout Alaska (Pastick et al., 2015).

The study area is geologically diverse, with regional-scale fault and fold structures and bedrock lithologies including Cretaceous-Paleogene sedimentary and volcanic rocks underlain by Triassic basalt and metabasalt (Gilbert, 1979; Wilson et al., 2015). Active tectonic activity, Pleistocene glaciation, and ongoing fluvial and hillslope processes create a complex geomorphic setting (Csejtey et al., 1982; Gilbert, 1979; Nokleberg et al., 1994; Yeend, 1997; Wilson et al., 2015, Patton et al., In Revision). Ongoing evolution of the high-relief topography in DNP also reflects the regular occurrence of landslides of multiple styles (Patton et al., In Revision).

Our work focuses on the Park Road corridor in DNP (Fig. 4.1), where human use is most concentrated and where road maintenance interacts with landslide process (Vinson et al., 1999; Capps et al., 2017). I use three small landslides as case studies to evaluate the impact of landslide age, morphology, and permafrost condition on the topographic deformation over the one-year study period.

4.2 METHODS

To evaluate the processes that control landslide development in small landslides, I investigated three study landslides along the DNP road corridor. All three landslides are small, shallow angle, south-facing landslides (Table 1) in poorly-sorted unconsolidated sediment (colluvium or glacial deposits). Two of the study slides are active layer detachments (ALDs). The Ptarmigan ALD is young, with an initiation date in summer of 2016. The Eielson ALD is partially re-vegetated, with some mosses and low tundra plants but no shrubs, which indicates that it is several decades old (Roland, 2019, Personal Communication). The Stony Pass Slide is a young (2015) complex slide, characterized by a combination of translational and rotational

movement, although the morphology of this landslide resembles compact ALDs (Lewkowicz and Harris, 2005b). The Stony Pass Slide is also influenced by de-stabilization during ongoing road maintenance; maintenance staff periodically remove accumulated sediment to clear the roadway.

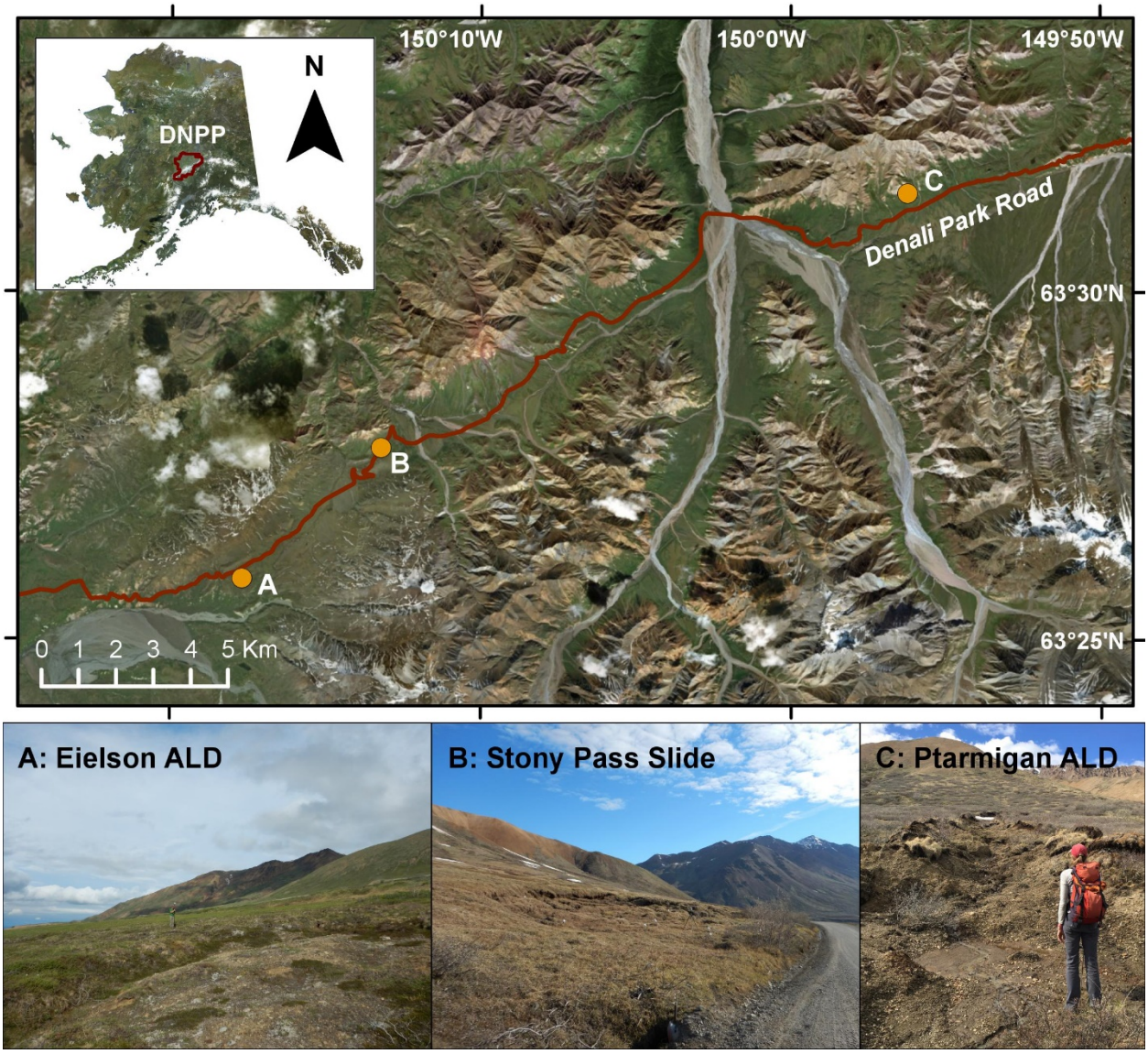

Figure 4.1. Map of study area in Denali National Park (DNP) showing the Denali Park Road in red and the three study sites as orange circles. The braided Toklat River flows from north to south between sites B and C. ALD indicates Active Layer Detachments. People for scale are about 2 m tall.

4.2.1 Terrestrial laser scanning (TLS)

To quantify topographic change with high precision, I conducted repeat terrestrial laser scan (TLS) surveys in June 2017, and June/early July 2018, following the basic methodology of previous TLS slope investigations (e.g. Abellán et al., 2014). Surveys were conducted in spring as soon as sufficient snow had melted from the slide area to capture the ground surface. Notably, the June 2017 survey of the Ptarmigan ALD does capture some snow near the base of the landslide scarp. I georeferenced the TLS point clouds by surveying five or more target points with an RTK-GPS. I then used the Geomorphic Change Detection (GCD) Software (Wheaton et al., 2010) to calculate elevation difference between the three surveys. I used simple additive error propagation to combine error from the TLS, RTK survey, and OPUS correction, such that the Stony Pass, Ptarmigan, and Eielson landslides each had a total estimated error of 3.5 cm, 7.9 cm, and 4.4 cm, respectively. These values are input as significance thresholds for differencing, such that differenced values that are lower than the error magnitude are reported as "no data" in the resulting DEM of Difference (DoD). Vegetation heights were similarly low in the two surveys, but small differences in grass height and leaf density introduce noise that cannot be completely filtered from the off-nadir TLS returns. Vegetation density is greatest in the undisturbed portions of the slope and on the vegetated landslide toe at the Stony Pass Slide (Fig. 4.1B) and the Ptarmigan ALD (Fig. 4.1C). Although the three-dimensional data are not shown here, I also used the Multiscale Model to Model Cloud Comparison (M3C2) point cloud differencing technique (Lague et al., 2013; Barnhart and Crosby, 2013) to visually evaluate point cloud surfaces and identify areas where vegetation likely contributed the most noise.

4.2.2 Ground-penetrating radar (GPR)

In collaboration with Dan McGrath (Colorado State University), I collected radar data along transect lines in and near the Stony Pass Slide in August 2018 using a Pulse-Ekko 500 MHz GPR unit and processed data using ReflexW software. I used processed radargrams to visually identify the permafrost surface. At 54 nodes along survey lines, I manually probed to refusal at the permafrost surface using a cm-scale steel probe, with a maximum probe depth of 2.3 m. Although coarse slope material interfered with some measurements, recorded depths presented here are areas where I had high confidence that the probe hit refusal at the ice surface. Probe depths to permafrost did not show any relationship with return times of radar traces, and I therefore did not estimate depth to permafrost using radar data. I assumed that maximum active layer depth in August 2018 approximates depth to permafrost, although it is important to note that the exact depth of the permafrost surface is variable in time and space. I also collected similar GPR data at the Ptarmigan ALD, although highly uneven topography, surface water, and 1-2 m tall shrubs prevented continuous coupling of the GPR unit and the ground surface.

4.3 RESULTS

4.3.1 Landslide morphology

The three study landslides exhibit diverse morphology, although slope characteristics at each site are broadly similar (Table 1, Fig. 4.1). The Stony Pass Slide (851 m^2) is arcuate in map view, with a steep ~1 m tall headscarp, 0-0.5 m side scarps, and no distinct levees. Landslide width is 31.5 m. Within the interior of the landslide, vegetation (moss and grasses) is preserved on top of small back-rotational steps. Bare clay-rich sediment is exposed between these steps.

The Ptarmigan ALD (2341 m^2) is elongate in shape, with a total length of 129 m and an average width of 14.3 m. The Ptarmigan ALD is channelized and lined by sharp levees (1-2 m tall), with surface water observed in the channel in mid-late summer. Levees are composed primarily of tundra vegetation and root masses; in some areas tall shrubs have been preserved on the top of levees.

The Eielson ALD (1246 m^2) exhibits two distinct morphologic units. The eastern portion of the landslide is channelized, with a rocky channel and small levees (<1 m tall). The morphology of the western portion of the landslide is stepped, similar to the Stony Pass Slide, although the majority of the western portion of the Eielson ALD is vegetated by moss and grasses. The combined width of the landslide is 35 m.

Table 4.1. Summary characteristics of the three study landslides in DNP. Probable initiation dates are based on first-person accounts for the two younger landslides and the degree of vegetation recovery in the older landslide. Active layer thickness and mean decadal ground temperature data are from a recent model of permafrost distribution in the park (Panda et al., 2014) and are estimates for the 2001-2010 decade.

	Stony Pass Slide (Fig. 4.1B)	**Ptarmigan ALD (Fig. 4.1C)**	**Eielson ALD (Fig. 4.1A)**
Coordinates	63.46286, -150.2204	63.52394, -149.9374	63.43146, -150.2948
Probable initiation date	2015	Summer 2016	20-50 years ago
Slide area (m^2)	851	2341	1246
Length (m)	30.5	129	39
Width (m)	31.5	14.3	35
L/W ratio	0.97	9.0	1.1
Elevation at scarp (m)	1182	1198	1129
Slope angle	10.3°	16.5°	12.0°
Slope aspect	116°	151°	162°
Lithology	Glacial moraine	Colluvium	Glacial outwash
Active layer thickness (m)	0.90	1.8	Seasonal thaw
Mean decadal ground temperature (°C)	-1.0 °C	-0.2 °C	0.36 °C
Elevation loss at scarp (m)	-0.8	-1.0	-0.2
Maximum elevation loss (m)	-0.8	-1.0	-0.5
Morphology	Compact	Elongate	Complex

4.3.2 Topographic change

Over the one-year study period, the older Eielson ALD demonstrated minimal change in elevation (Fig. 4.2). Maximum elevation loss in this landslide is 0.5 m in a 0.25 m^2 area on the mid-channel side scarp, with maximum elevation loss of 0.2 m at the scarp and between vegetated steps and maximum elevation gain of 0.2 m on the vegetated steps. Elevation loss is not spatially continuous along the landslide scarp or within the body of the landslide. The majority of the landslide by area did not experience significant elevation change, as is shown by the low magnitude of differences and the relative symmetry of the distribution of differenced cell values around zero (Fig. 4.3).

Both of the younger landslides, the Stony Pass Slide and the Ptarmigan ALD, experienced significant elevation change over the study period. Excluding areas with dense vegetation, maximum elevation loss within the Stony Pass Slide is 0.8 m near the landslide scarp. The majority of the landslide body lowered by 0.04-0.25 m. Elevation loss is spatially continuous along the scarp and within the body of the landslide, as is shown by the fact that the majority of the differenced cell value distribution is negative (Fig. 4.3). The two peaks in negative differenced cell values show the moderate elevation loss within the body of the landslide and the larger elevation loss along the scarp. Some material accumulated at the toe of the landslide over the one-year study period, with a maximum elevation gain of 0.5 m and characteristic elevation gain of 0.04-0.25 m. Vegetation near the landslide toe adds uncertainty to this estimate of elevation gain. Some landslide debris was also removed from the landslide toe at the park road by maintenance staff during the study period.

Excluding the known snow field and areas with dense vegetation, the maximum elevation loss within the Ptarmigan ALD is 1.0 m near the scarp. The majority of the landslide channel lowered by 0.1-0.6 m. Characteristic elevation loss in the channel is 0.09-0.30 m. Elevation loss is spatially continuous along the landslide scarp and within the channel, as is shown by the fact that the majority of the differenced cell value distribution is negative (Fig. 4.3). Some material accumulated at the toe of the landslide over the one-year study period, with a maximum elevation gain of 1.0 m. Dense vegetation on the landslide toe and on levees adds substantial uncertainty to this estimate of elevation gain.

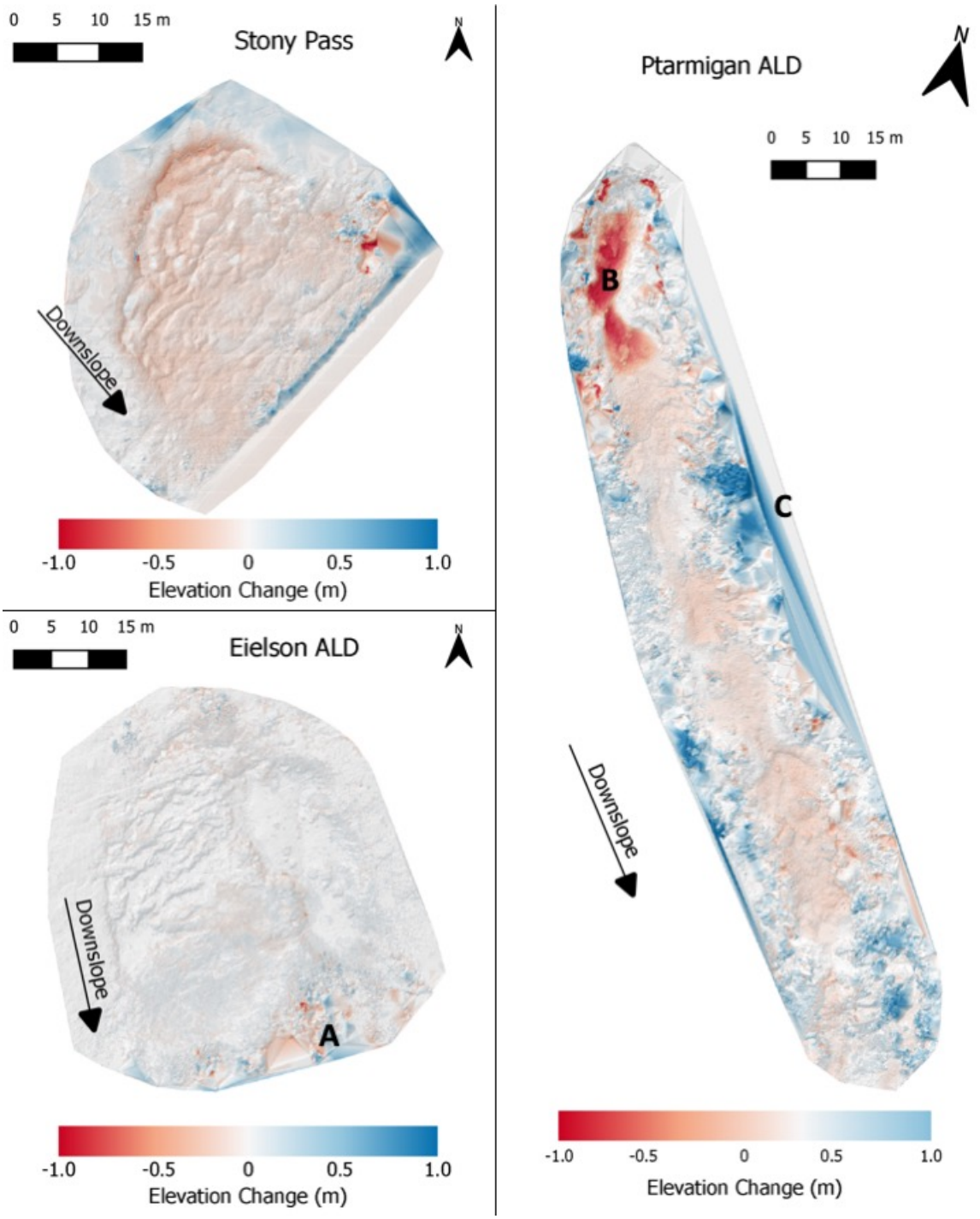

Figure 4.2. DEMs of Difference (DoDs) showing significant elevation change at the three study landslides from June 2017 to June/July 2018. Where cell differences are smaller than the magnitude of propagated error, no significant change has occurred. Dense vegetation adds uncertainty to changes in the ground surface, which is most visible in areas where elevation gain/loss is inconsistent on a small scale (e.g. area A). Snow near the scarp of Ptarmigan ALD added error to the surface difference at area B. Sparse point cloud data add uncertainty to the edges of the survey data (e.g. area C).

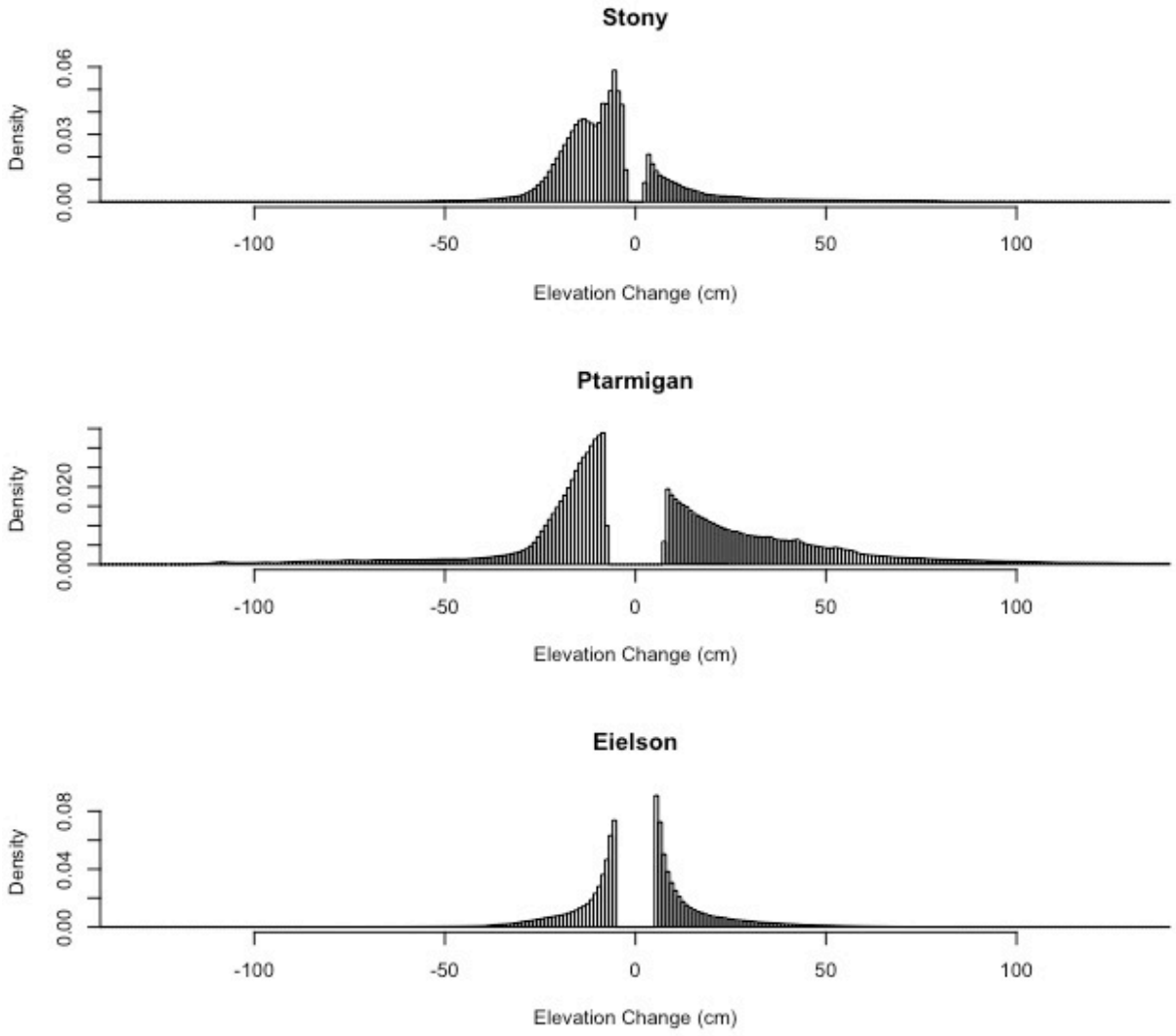

Figure 4.3. Histograms showing cell values of the one-year difference in elevation at the three study landslides. Values within the threshold of error described in are reported as "no change" and are not included on the histograms. The Stony Pass, Ptarmigan, and Eielson error values are 3.5 cm, 7.9 cm, and 4.4 cm, respectively.

4.3.3 Permafrost condition

Using the radargram data, I identified permafrost with high confidence near the Stony Pass Slide, particularly in the undisturbed slope to the northeast of the landslide (Fig. 4.4). I did not identify any permafrost within the slide with radar data or the manual probe, however. Measured probe depths indicate that permafrost is present at 0.4-1.5 m depth to the northeast of the slide, and 0.9-1.9 m depth to the northwest of the landslide scarp. Average depth to permafrost was 1.06 m ± 0.4 m. These measured depths to permafrost approximately align with the most recent permafrost model of DNP, which estimated 0.90 m depth to permafrost in the 2001-2010 decade at this location and in adjacent cells (Panda et al., 2014). Processed GPR data from the Ptarmigan ALD returned inconclusive subsurface data and are therefore not presented here (Appendix C).

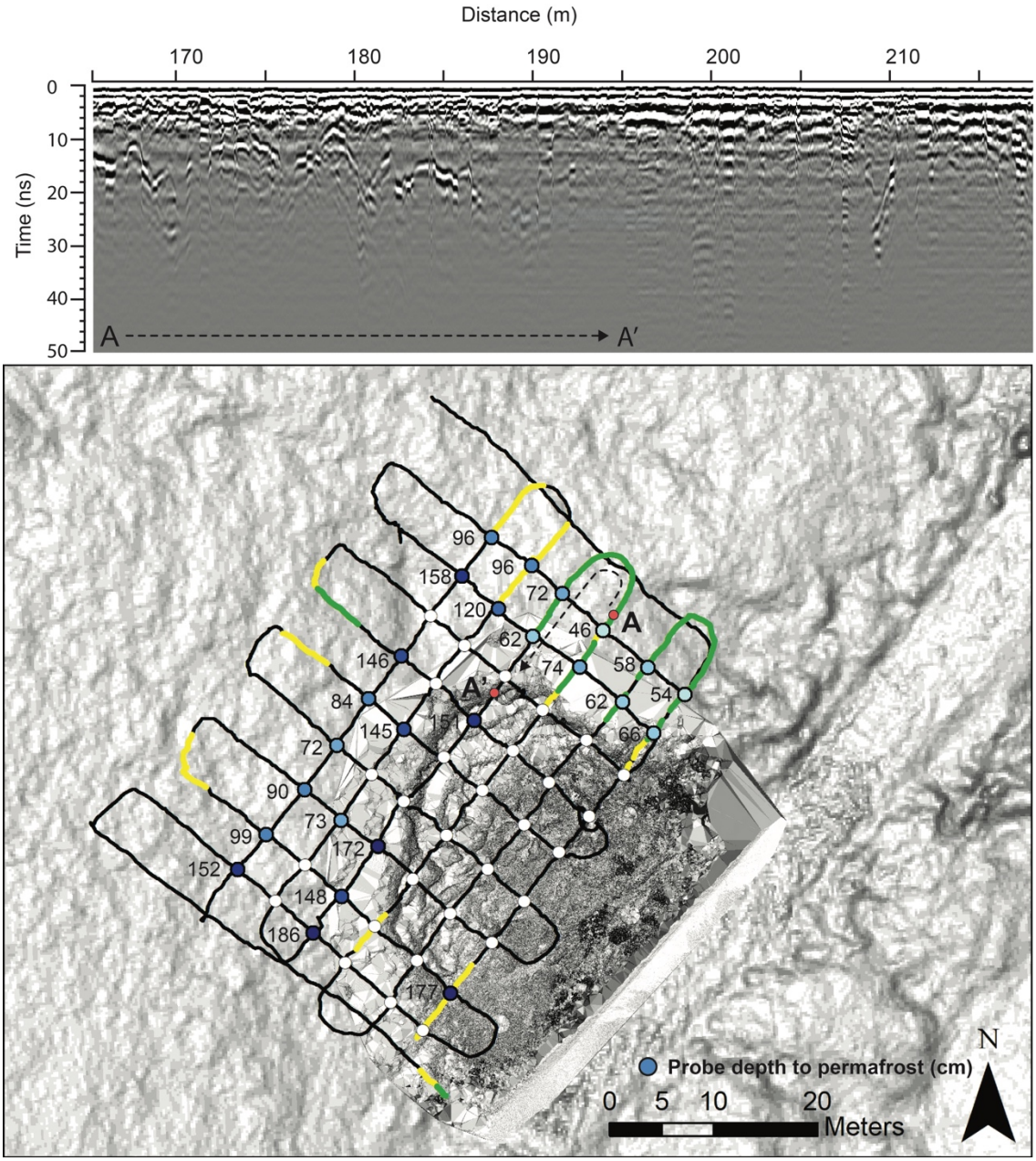

Figure 4.4. Example radargram, GPR transects, probe locations at the Stony Pass Slide. High-confidence permafrost surface is visible in the radargram (~165-187 m). I did not identify a permafrost surface on this radargram from 878-905 m. The radargram is a cross-section of the GPR transect that follows a curve, as shown by the A-A' arrow in map view. GPR transect lines are shown in map view on a slope map derived from the 2018 TLS survey, over a 24 cm slope map derived from photogrammetry collected in 2015. Portions of the transect with high-confidence permafrost are shown in green, low-confidence permafrost is shown in yellow, sections with no observed permafrost are indicated by a black line. Blue points show locations where manual probing identified permafrost, with darker blue indicating greater depth to permafrost. White points show locations where manual probing did not identify permafrost within 2.3 m depth.

4.4 DISCUSSION

4.4.1 Landslide morphology

At all three landslides, I interpret initial failure on a shallow-angle permafrost plane at ~1-2 m depth, although recent permafrost models indicate that permafrost at Eielson ALD has since thawed (Panda et al., 2014). Positive pore pressures above the permafrost-active layer boundary after melt of permafrost ice allow for slope failure even on shallow hillslopes (Harris and Lewkowicz, 2000; Lewkowicz and Harris, 2005b; Lewkowicz, 2007). Despite the similarity of slope angle (10.3-16.5°), lithology, and aspect (116-162°), the three landslides studied in DNP demonstrate diverse morphology.

Morphology of the Ptarmigan ALD is similar to that of the elongate ALDs described by Lewkowicz and Harris (2005) in northern Canada; the length-to-width ratio is 9.0, the largest of the three DNP landslides described in this study. Similarities also include the landslide shape in plan view and lateral compression structures along the length of the landslide. The Ptarmigan ALD created 1-2 m levees where vegetated ridges of soil, organic material, and tundra accumulated along the margins of the slide.

Morphology and thaw patterns of the Stony Pass Slide are similar to those of the "compact" ALD morphology described by Lewkowicz and Harris (2005). The landslide they describe initiated along the permafrost boundary during a forest fire. Rapid thaw of permafrost after the landslide initiated allowed a retrogressive slump to develop. Similarly, the Stony Pass Slide appears to have initiated along the thawing permafrost boundary, which then continued to thaw to the point that I was not able to observe permafrost within the slide.

Morphology of the Eielson ALD is similar to the complex ALDs described by Lewkowicz and Harris (2005). Although the exact failure sequence is not clear, I interpret an initial elongate failure on the eastern portion of the slide, with subsequent retrogressive failure of the western portion of the landslide in response to loss of lateral support. These two deformation events may have occurred nearly-simultaneously or may have been separated by days to months.

4.2 Topographic change

I observed spatially continuous elevation change at the young landslides, with a maximum elevation loss of 1.0 m within the Ptarmigan ALD (excluding the area beneath the snow field in 2017) and 0.8 m within the Stony Pass Slide. The elevation loss in the Ptarmigan ALD is primarily in the channel bottom and scarp. Magnitude of ground surface change outside of the landslide channel (i.e. on the levees) is not clear, because brush and tall grass prevented detailed characterization of the levee surfaces and the undisturbed hillslope. Ongoing surface lowering within the Ptarmigan ALD is consistent with scarp retreat and surface water erosion of fine material from the channel. Although the magnitude of sediment accumulation at the Ptarmigan ALD toe is unclear, it is likely that some sediment accumulates at the landslide toe and that surface water transports some eroded material farther downslope.

Elevation loss at Stony Pass Slide is concentrated near the scarp, which retreated upslope by ~1 m over the one-year study. Spatially continuous subsidence also occurred throughout the landslide body and lowered ground elevations by 0.04-0.25 m. These surveys also capture a small buildup of material at the toe of the landslide; additional material was removed along the road by maintenance staff during the study period. This removal of sediment at the landslide toe

reduces lateral confinement, likely promotes downslope transport and continued landslide deformation.

I observed minimal significant topographic change at the Eielson ALD, indicating that stabilization of this landslide has occurred in the 20-50 years since it initiated. If the Eielson ALD is representative of other shallow-seated, shallow-angle landslides in the study region, this 20-50 year stabilization is the baseline recovery time under recent climate and permafrost conditions. In the previous 20-50 years, as climate patterns shift and permafrost continues to degrade, the recovery times of shallow-seated landslides may change, however. Due to increased hydraulic conductivity and connectivity as permafrost thaws (Walvoord and Kurylyk, 2016a), as well as changing structure of vegetation communities (Fisher et al., 2016), the recovery time of the Stony Pass Slide, Ptarmigan ALD, and other new landslides may not follow historical patterns.

4.4.3 Permafrost and ongoing landslide deformation

In a recent permafrost model for Denali National Park (Panda et al., 2014), permafrost is present at 0.90 m depth at the Stony Pass site, and 1.8 m depth at the Ptarmigan site (Table 1). Although permafrost was not modeled at the Eielson site during the time period of the Panda et al. (2014) study, I assume that permafrost was likely present at the time of initiation 20-50 years ago based on landslide morphology, rates of permafrost loss within the park, and the modern mean decadal ground temperature that is just above 0° C. Identification of the permafrost surface at the Ptarmigan ALD using radar data was inconclusive. Although two-dimensional radar data improve the spatial resolution of subsurface imaging, heterogeneous substrate, vegetation, patchy

surface water, and irregular topography limit the effectiveness of this technique in complex terrain.

Where I measured permafrost in the Stony Pass landslide, depth to permafrost is variable but on the same order of magnitude as the permafrost model (0.4-1.9 m). I did not identify any permafrost within the interior of the landslide, however, in the radargram or with a manual probe. It is likely that warm climate and landslide disturbance have accelerated permafrost thaw in the decade since the model was produced, resulting in a spatially reduced permafrost extent in the study area.

The loss of permafrost within the slide boundary likely contributes to the ongoing deformation of this landslide, as loss of permafrost ice can reduce shear strength and increase groundwater conductivity and connectivity (Rist, 2008; Huggel, 2009; Shan, Guo, Wang, et al., 2014; Walvoord and Kurylyk, 2016a; Patton et al., 2019). The relative timing of landslide initiation (2015) and the onset of widespread permafrost thaw at Stony Pass is not known, but the low angle of the slope indicates that some degree of ice thaw occurred before the landslide initiated, which produced meltwater and reduced shear strength, contributing to slope susceptibility. After the initiation of the Stony Pass Slide, ground disturbance and loss of some tundra vegetation likely increased the heat flux from the atmosphere to the subsurface and contributed to accelerated permafrost thaw near the disturbed area during warm months.

Furthermore, the topographic depression formed by the landslide shields snow within the landslide body, allowing a thicker snowpack to accumulate and persist into the spring. (Fig. 4.5). The increased insulation in the winter and spring likely prevents cold air temperatures from fully freezing the ground beneath the landslide. Gradual release of meltwater in the spring may also deliver both groundwater and heat energy, further increasing near-surface ground temperatures

and soil saturation. At the Stony Pass slide, snow within the landslide persisted long after snow on the adjacent hillslope had melted and caused a delay in the planned TLS survey until the snow fully melted in early July 2018. The combined loss of insulation during the warm season (loss of vegetation) and increased insulation during the cold season (deeper snowpack) likely resulted in an increased rate of permafrost thaw beneath the landslide.

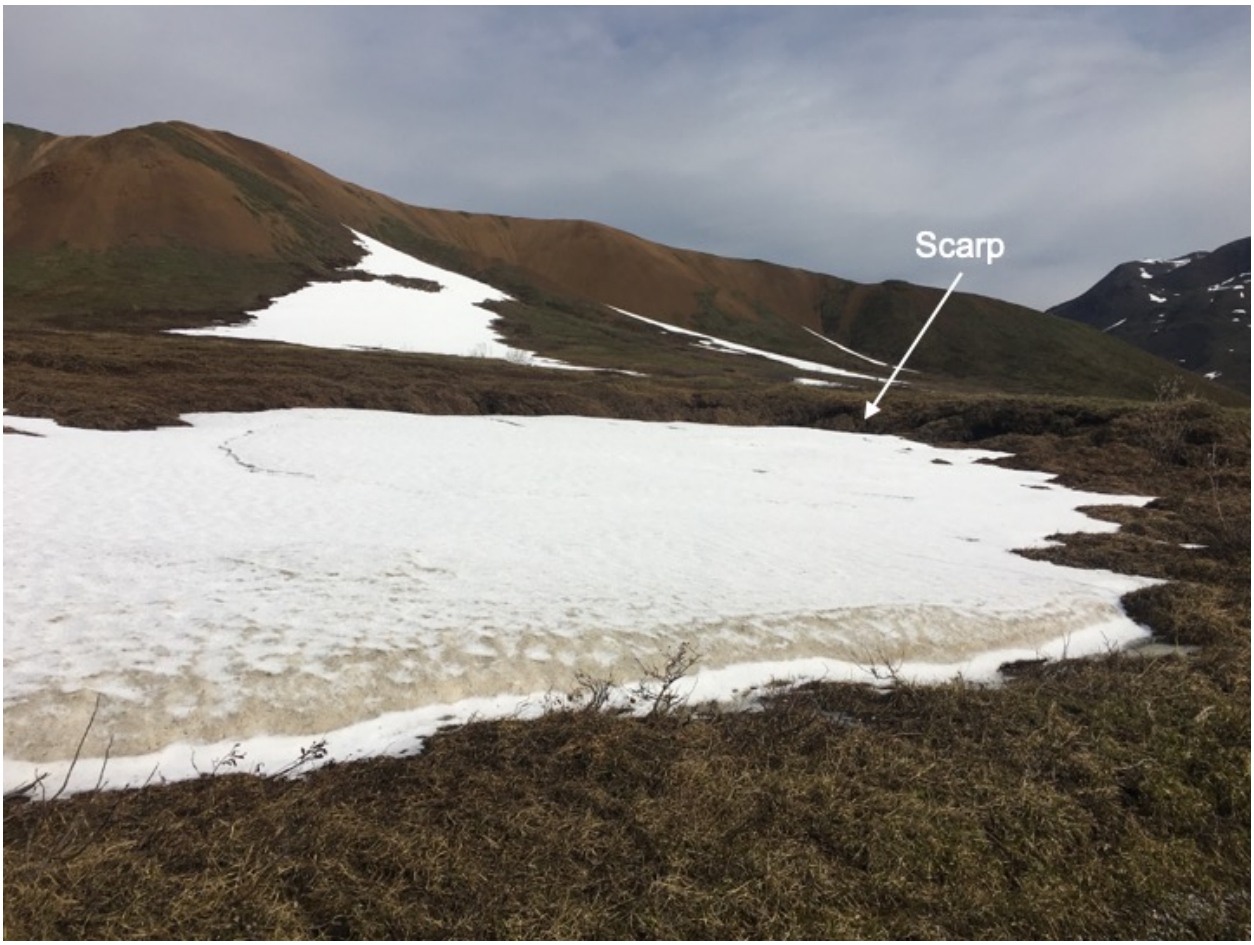

Figure 4.5. Snow accumulation within the Stony Pass Slide in late June, 2018. Deep snow that accumulated in the slide body likely insulated the slide from cold air temperatures in the winter and early spring.

Based on these observations, I postulate that the relationship between permafrost thaw and landslide initiation creates a positive feedback loop, in which both processes promote each other (Fig. 4.6). Human disturbance, such as the removal of landslide debris, likely contributes to

this effect by further facilitating heat flux to the subsurface. This hypothesis is consistent with observations of continued instability following fire-related permafrost thaw in Canada, where disturbance of insulating vegetation initiated progressive thaw of permafrost throughout the landslide (Lewkowicz and Harris, 2005b).

In the context of ongoing permafrost thaw at Stony Pass and continued removal of debris from the landslide toe, I predict continued subsidence and retrogressive erosion of the scarp at Stony Pass Slide. The feedback between climate change and landslide disturbance will likely accelerate permafrost thaw in this area in the upcoming decades, exacerbating existing landslide hazards. Accelerated permafrost thaw and landslide occurrence will pose serious challenges for the management of high-use public lands throughout sensitive permafrost regions, where human activity and infrastructure will also contribute to landslide occurrence and permafrost thaw.

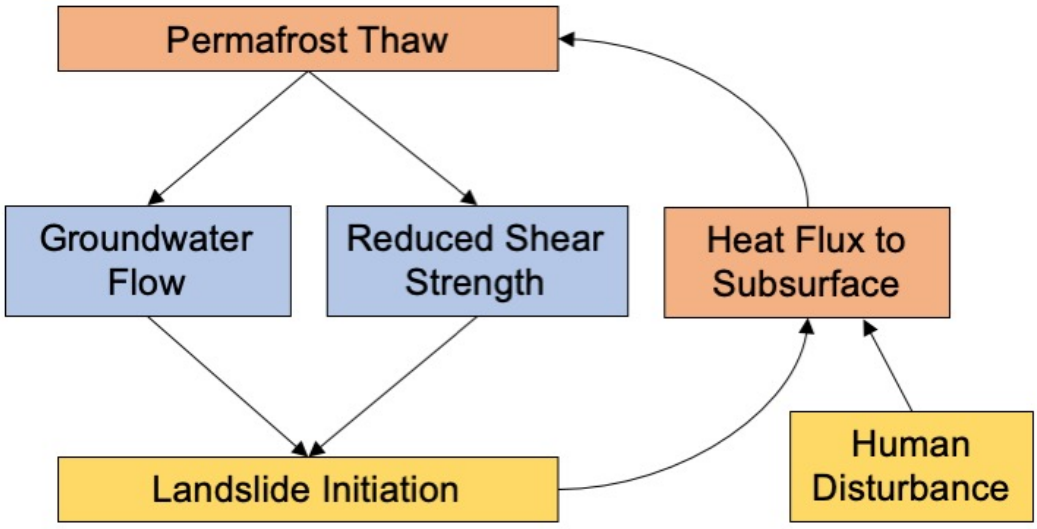

Figure 4.6. Conceptual diagram showing postulated feedback loop between permafrost thaw and landslide initiation. The term "groundwater flow" is used to describe a number of permafrost-related changes to groundwater process. Relative importance of different processes likely varies spatially and temporally.

4.4.4 Climate change and predictions for landslide development

Climate change is likely to exacerbate landslide hazard around the globe (Gariano and Guzzetti, 2016; Patton et al., 2019). A nationwide study of climate change in national parks estimated an increase in average annual temperature of 4.3 ± 1.1 °C per century in DNP, the highest of any national park in the United States (Gonzalez et al., 2018). Earlier climate models for DNP specifically forecasted an 0.9-3.4 °C increase in annual average daily temperature and an 0.09-0.28 mm (6.87-26.71% change) increase in average annual daily precipitation by the end of this century (Crossman et al., 2013). Winter temperatures are likely to increase more relative to summer temperatures, and the warm season will become longer (Rupp and Loya, 2008; Crossman et al., 2013). The exact influence of increased annual precipitation depends on the timing and intensity of additional precipitation relative to increased evapotranspiration as the growing season becomes longer (Rupp and Loya, 2008).

Under these conditions, discontinuous permafrost is expected to degrade rapidly (Panda et al., 2014; Pastick et al., 2015), facilitating the initiation of shallow-angle landslides. Although increased evapotranspiration rates may result in lower soil moisture over the course of the year (Rupp and Loya, 2008), changes to storm intensity may continue to promote rain-induced landslides as well as thaw-induced landslides. This increase in landslide frequency is likely to be most profound during the adjustment period of permafrost thaw over the next few decades (Blais-Stevens, Kremer, et al., 2015). Furthermore, an increase in the length of the warm season is likely to extend the portion of the year when landslides may occur, and rapid ice melt may destabilize hillslopes that were previously considered low-hazard.

4.5 CONCLUSIONS

Ongoing deformation of recent landslides continue to deliver sediment downslope and alter local topography by lowering ground surface elevation over one year by up to 0.8 m and 1.0 m in the Stony and Ptarmigan landslides, respectively. The older landslide investigated appears to have achieved stability within the several decades since initiation. Ongoing climate change may cause modern active landslides to remain unstable over longer timeframes.

Although discontinuous permafrost persists in the Stony Pass area, no permafrost was identified within the slide area, indicating a loss of permafrost before and/or after landslide initiation. Observations of this landslide indicate that permafrost degradation increases meltwater saturation and groundwater connectivity and promotes continued downslope movement. Based on these processes, permafrost thaw may contribute to triggering landslides. Once a landslide occurs, accelerated permafrost thaw within the landslide may result from ground disturbance, loss of vegetation insulation during the summer, and deeper snow insulation during the winter. Permafrost thaw likely creates a positive feedback loop with landslide process, such that landslide occurrence accelerates permafrost thaw and permafrost thaw promotes landslide initiation and continued deformation. Ongoing human activity likely contributes to the destabilization of the Stony Pass Slide, as removal of material from the landslide reduces lateral support and contributes to increased heat flux to the subsurface. The Stony Pass landslide is likely to continue to deliver sediment to the DNP road and pose persistent hazards.

Forecasted climate patterns are likely to increase the frequency and deformation rates of ALDs and other shallow-angle permafrost landslides. Increased average temperature, increased average precipitation, and longer summers will extend the spatial and temporal distribution of

landslides in DNP and other sensitive permafrost regions. Landslide frequency is likely to be highest in the upcoming decades during an adjustment period of widespread permafrost loss.

5. CONCLUSIONS

On a global scale, widespread permafrost thaw will alter the hydrology, vegetation, and physical properties of hillslopes in high-latitude and high-elevation areas, resulting in loss of shear strength of slope materials. The transition to seasonally thawed slopes is likely to alter the dynamic equilibrium states of hillslopes in these regions in the next several decades. Based on the existing literature, I conclude that landslides will be driven primarily by atmospheric input of moisture and freeze-thaw fracturing rather than responding to disconnected perched groundwater, melting permafrost ice, and a discontinuity at the permafrost surface. The transition between equilibrium states is likely to increase landslide frequency and magnitude, alter dominant failure styles, and mobilize carbon over timescales ranging from seasons to centuries. These changes to landslide regimes are likely to pose serious geotechnical challenges for human communities and the environment.

In DNP, landslides occur primarily on high-elevation hillslopes on all slope aspects. Landslides initiate on slope angles with a bimodal distribution, indicating that landslides are driven by two primary failure mechanisms in discontinuous permafrost regions, including atmospheric events and permafrost/ice thaw. Landslides in the study area preferentially initiate in areas underlain by permafrost, and landslides in permafrost terrain occurred on slope angles approximately 7° shallower than landslides on seasonally thawed hillslopes. Shallow-angle landslides (<20° slopes) in permafrost demonstrate that permafrost/ice thaw is an important triggering mechanism in the study region. Melting permafrost reduces shear strength by lowering cohesion and friction values along ice boundaries. Unconsolidated units, including colluvium and glacial deposits generate a disproportionate number of landslides. Felsic volcanic rocks also

generate a disproportionate number of landslides due to the rapid weathering of feldspars to clay minerals (particularly montmorillonite, vermiculite, and beidellite). The presence of clay minerals may promote landslide initiation by impeding groundwater flow and increasing local pore pressure, reducing rock strength.

Ongoing deformation of two recent, shallow-angle landslides in DNP (Ptarmigan ALD and Stony Pass Slide) continue to deliver sediment and alter local topography by lowering ground surface elevation over one year by up to 1.0 m. The older landslide investigated (Eielson ALD) achieved stability within several decades since initiation, indicating that small landslides achieved topographic stability within several decades under recent climate conditions. Although discontinuous permafrost persists in the DNP road corridor, no permafrost was observed within the interior of the Stony Pass Slide, indicating a loss of permafrost before and/or after landslide initiation. Because landslide disturbance alters heat exchange patterns with the atmosphere, by removing summer insulation (vegetation and organic soil) and adding winter insulation (snow), the development of landslides likely creates a positive feedback loop with permafrost thaw, such that landslide occurrence accelerates permafrost thaw and permafrost thaw promotes landslide initiation and continued deformation. Human modification and ground disturbance may exacerbate landslide deformation and permafrost thaw.

Based on predicted changes of increased annual temperature, longer warm seasons, and increased rainfall in the next few decades, landslide occurrence is likely to increase in DNP and other discontinuous permafrost regions worldwide. In particular, increased permafrost degradation associated with climate change will make DNP and other high-relief areas more susceptible to shallow-angle landslides, which pose persistent management problems by damaging infrastructure. The comprehensive inventory of modern landslides in the DNP road

corridor up to August 2018 provides a baseline dataset for comparison of future landslides and time-series analysis of landslide frequency in the Alaska Range.

5.1 MANAGEMENT RECOMMENDATIONS

Management recommendations based on the results of this work include:

1. Expand current hazards assessments to evaluate slopes that may have been considered "stable" under recent climate conditions. In particular, shallow-angle hillslopes in discontinuous, thawing permafrost, may pose new management concerns.
2. Avoid developing new infrastructure on susceptible hillslopes where permafrost is present, as thawing permafrost will counteract many standard stabilization techniques. Given the rate of temperature increase at high latitudes, most techniques to stabilize permafrost are effective only temporarily.
3. Collect repeat data and aerial imagery (topographic data, orthophotos, multispectral imagery, etc.) at a scale that captures patterns of landslide initiation. Remote imagery may also be useful for monitoring permafrost degradation.
4. Maintain or create emergency response plans, knowing that many high-latitude permafrost regions are vulnerable to landslides and other geohazards due to sparse infrastructure. In particular, damage to vital access roads may necessitate alternative access strategies for responders.

5.2 FUTURE RESEARCH

As outlined in Chapter 2, recommendations for future research include quantifying the total C mobilized by shallow-angle landslides in thawing permafrost. The relative importance of

this C pool to terrestrial C budgets is currently unknown, because the total mass of C moved by landslides has not been quantified. To address this objective, I intend to estimate C concentration in a collection of soil samples from shallow-angle landslides in the DNP road corridor. I will use estimates of landslide volume to calculate the total mass of C mobilized in each individual landslide and across the study area. Preliminary data are presented in Appendix D. Additionally, I intend to compare C concentrations in landslide soils and proximal undisturbed soils to evaluate the impact of landslide process on carbon sequestration or release.

6. REFERENCES

Abbott, B.W., Jones, J.B., Godsey, S.E., Larouche, J.R., and Bowden, W.B., 2015, Patterns and persistence of hydrologic carbon and nutrient export from collapsing upland permafrost: Biogeosciences, v. 12, p. 3725–3740, doi: 10.5194/bg-12-3725-2015.

Abellán, A., Oppikofer, T., Jaboyedoff, M., Rosser, N.J., Lim, M., and Lato, M.J., 2014, Terrestrial laser scanning of rock slope instabilities: Earth Surface Processes and Landforms, v. 39, p. 80–97, doi: 10.1002/esp.3493.

ACIA, 2004, Impacts of a Warming Arctic: Arctic Climate Impact Assessment: Cambridge University Press, Cambridge, 140 p., doi: 10.2277/0521617782.

Addison, P.E., Lautala, P., Oommen, T., and Vallos, Z., 2016, Embankment Stabilization Techniques for Railroads on Permafrost, *in* Proceedings of the 2016 Joint Rail Conference, Columbia, SC, p. 9, doi: 10.1115/JRC2016-5731.

Alexander, D., 2005, Vulnerability to Landslides, *in* Gade, T., Anderson, M., and Crozier, M.J. eds., Landslide Hazard and Risk, p. 175–198.

Alexeev, V.A., and Jackson, C.H., 2013, Polar amplification: Is atmospheric heat transport important? Climate Dynamics, v. 41, p. 533–547, doi: 10.1007/s00382-012-1601-z.

Allen, S., and Huggel, C., 2013, Extremely warm temperatures as a potential cause of recent high mountain rockfall: Global and Planetary Change, v. 107, p. 59–69, doi: 10.1016/j.gloplacha.2013.04.007.

Anderson, S.W., Anderson, S.P., and Anderson, R.S., 2015, Exhumation by debris flows in the 2013 Colorado Front Range storm: Geology, v. 43, p. 1–4, doi: 10.1130/G36507.1.

Anthony, J.W., Bideaux, R.A., Bladh, K.W., Nichols, M.C., and Eds., 2001, Handbook of

Mineralogy:, http://www.handbookofmineralogy.org/.

Apollaro, C., Accornero, M., Marini, L., Barca, D., and De Rosa, R., 2009, The impact of dolomite and plagioclase weathering on the chemistry of shallow groundwaters circulating in a granodiorite-dominated catchment of the Sila Massif (Calabria, Southern Italy): Applied Geochemistry, v. 24, p. 957–979, doi: 10.1016/j.apgeochem.2009.02.026.

Badger, T.C., and Ignazio, M.D., 2018, First-time landslides in Vashon advance glaciolacustrine deposits , Puget: Engineering Geology, v. 243, p. 294–307, doi: 10.1016/j.enggeo.2018.07.011.

Ballantyne, C.K., 2002a, A general model of paraglacial landscape response: The Holocene, v. 12, p. 371–376.

Ballantyne, C.K., 2002b, Paraglacial Geomorphology: Quaternary Science Reviews, v. 21, p. 1935–2007.

Barnard, P., Owen, L., Sharma, M., and Finkel, R., 2001, Natural and human-induced landsliding in the Garhwal Himalaya of Northern India: Geomorphology, v. 40, p. 21–35.

Barnhart, T.B., and Crosby, B.T., 2013, Comparing two methods of surface change detection on an evolving thermokarst using high-temporal-frequency terrestrial laser scanning, Selawik River, Alaska: Remote Sensing, v. 5, p. 2813–2837, doi: 10.3390/rs5062813.

Beamish, A., Neil, A., Wagner, I., and Scott, N.A., 2014, Short-term impacts of active layer detachments on carbon exchange in a High Arctic ecosystem, Cape Bounty, Nunavut, Canada: Polar Biology, v. 37, p. 1459–1468, doi: 10.1007/s00300-014-1536-4.

Behnsen, J., and Faulkner, D.R., 2012, The effect of mineralogy and effective normal stress on frictional strength of sheet silicates: Journal of Structural Geology, doi: 10.1016/j.jsg.2012.06.015.

Belshe, E.F., Schuur, E.A.G., and Bolker, B.M., 2013, Tundra ecosystems observed to be CO2 sources due to differential amplification of the carbon cycle: Ecology Letters, v. 16, p. 1307–1315, doi: 10.1111/ele.12164.

Benowitz, J.A., Layer, P.W., Armstrong, P., Perry, S.E., Haeussler, P.J., Fitzgerald, P.G., and VanLaningham, S., 2011, Spatial variations in focused exhumation along a continental-scale strike-slip fault: The Denali fault of the eastern Alaska Range: Geosphere, v. 7, p. 455–467, doi: 10.1130/ges00589.1.

Bittelli, M., Valentino, R., Salvatorelli, F., and Rossi, P., 2012, Geomorphology Monitoring soil-water and displacement conditions leading to landslide occurrence in partially saturated clays: Geomorphology, v. 173–174, p. 161–173, doi: 10.1016/j.geomorph.2012.06.006.

Blais-Stevens, A., Geertsema, M., Schwab, J.W., and Van Asch, T.W.J., 2015, Complex Landslide Triggered in an Eocene Volcanic-Volcaniclastic Succession along Sutherland River, British Columbia, Canada: Environmental & Engineering Geoscience, v. 21, p. 35–45, doi: 10.2113/gseegeosci.21.1.35.

Blais-Stevens, A., Kremer, M., Bonnaventure, P.P., Smith, S.L., Lipovsky, P., and Lewkowicz, A.G., 2015, Active Layer Detachment Slides and Retrogressive Thaw Slumps Susceptibility Mapping for Current and Future Permafrost Distribution, Yukon Alaska Highway Corridor: Engineering Geology for Society and Territory, v. 1, p. 449–453, doi: 10.1007/978-3-319-09300-0.

Blikra, L.H., and Christiansen, H.H., 2014, A field-based model of permafrost-controlled rockslide deformation in northern Norway: Geomorphology, v. 208, p. 34–49, doi: 10.1016/j.geomorph.2013.11.014.

Blikra, L.H., Kristensen, L., Christiansen, H.H., and Dehls, J., 2012, Displacements and the

influence of permafrost on rockslides in northern Norway; implications for driving mechanisms and hazards, *in* Eberhardt, E., Froese, C., Turner, K., and Leroueil, S. eds., Landslides and Engineered Slopes: Protecting Society through Improved Understanding, London, Taylor & Francis Group, p. 921–927.

Blunden, J., and Arndt, D. (Eds.), 2017, State of the Climate in 2016: American Meteorological Society, v. 98, 298 p., doi: 10.1175/2017BAMSStateoftheClimate.

Borga, M., Stoffel, M., Marchi, L., Marra, F., and Jakob, M., 2014, Hydrogeomorphic response to extreme rainfall in headwater systems: Flash floods and debris flows: Journal of Hydrology, v. 518, p. 194–205, doi: 10.1016/j.jhydrol.2014.05.022.

Borgatti, L., and Soldati, M., 2013, Hillslope Processes and Climate Change, *in* Shroder, J.F., Marston, R.A., and Stoffel, M. eds., Treatise on Geomorphology, Academic Press, v. 7, p. 306–319, doi: 10.1016/B978-0-12-374739-6.00180-9.

Borgatti, L., and Soldati, M., 2010, Landslides as a geomorphological proxy for climate change: A record from the Dolomites (northern Italy): Geomorphology, v. 120, p. 56–64, doi: 10.1016/j.geomorph.2009.09.015.

Borrelli, L., and Gullà, G., 2017, Tectonic constraints on a deep-seated rock slide in weathered crystalline rocks: Geomorphology, doi: 10.1016/j.geomorph.2017.04.025.

Bourg, A.C.M., and Berlin, C., 1994, Seasonal and Spatial Trends in Manganese Solubility in an Alluvial Aquifer: Environmental Science and Technology, v. 28, p. 868–876, doi: 10.1021/es00054a018.

Bowden, W.B., Gooseff, M.N., Balser, A., Green, A., Peterson, B.J., and Bradford, J., 2008, Sediment and nutrient delivery from thermokarst features in the foothills of the North Slope, Alaska: Potential impacts on headwater stream ecosystems: Journal of Geophysical

Research: Biogeosciences, v. 113, p. 1–12, doi: 10.1029/2007JG000470.

Bring, A., Fedorova, I., Dibike, Y., Hinzman, L., Mård, J., Mernild, S.H., Prowse, T., Semenova, O., Stuefer, S.L., and Woo, M.K., 2016, Arctic terrestrial hydrology: A synthesis of processes, regional effects, and research challenges: Journal of Geophysical Research G: Biogeosciences, v. 121, p. 621–649, doi: 10.1002/2015JG003131.

Byerlee, J., 1978, Friction of Rocks: Pure and Applied Geophysics, v. 116, p. 615–626.

Cannone, N., Lewkowicz, A.G., and Guglielmin, M., 2010, Vegetation colonization of permafrost-related landslides, Ellesmere Island, Canadian high arctic: Journal of Geophysical Research: Biogeosciences, v. 115, p. 1–10, doi: 10.1029/2010JG001384.

Capps, D.M., Rosenberg, R., Collins, A., Hooper, S., Rogers, H., Anderson, D.A., Collins, B., and Bilderback, E., 2017, Geohazards Risk Assessment of the Denali National Park Road, *in* 3rd North American Symposium on Landslides, Roanoke, VA, Association of Engineering & Environmental Geologists, p. 840–850.

Carling, G.T., Tingey, D.G., Fernandez, D.P., Nelson, S.T., Aanderud, Z.T., Goodsell, T.H., and Chapman, T.R., 2015, Evaluating natural and anthropogenic trace element inputs along an alpine to urban gradient in the Provo River, Utah, USA: Applied Geochemistry, v. 63, p. 398–412, doi: 10.1016/j.apgeochem.2015.10.005.

Christiansen, H.H., Etzelmüller, B., Isaksen, K., Juliussen, H., Farbrot, H., Humlum, O., Johansson, M., Ingeman-Nielsen, T., Kristensen, L., Hjort, J., Holmlund, P., Sannel, A.B.K., Sigsgaard, C., Åkerman, H.J., et al., 2010, The Thermal State of Permafrost in the Nordic Area during the International Polar Year 2007–2009: Permafrost and Periglacial Processes, v. 21, p. 156–181, doi: 10.1002/ppp.687.

Coe, J.A., and Godt, J.W., 2012, Review of approaches for assessing the impact of climate

change onlandslide hazards, *in* Eberhardt, E., Froese, C., Turner, K., and Leroueil, S. eds., Landslides and Engineered Slopes: Protecting Society through Improved Understanding, London, Taylor & Francis Group, p. 371–377.

Coe, J.A., Kean, J.W., Godt, J.W., Baum, R.L., Jones, E.S., Gochis, D.J., and Anderson, G.S., 2014, New insights into debris-flow hazards from an extraordinary event in the Colorado Front Range: GSA Today, v. 24, p. 4–10, doi: 10.1130/GSATG214A.1.

Cole, R.B., and Layer, P.W., 2000, Stratigraphy, age, and geochemistry of Tertiary volcanic rocks and associated synorogenic deposits, Mount McKinley Quadrangle, Alaska, *in* Wilson, F.H. and Galloway, J.P. eds., Studies by the U.S. Geological Survey in Alaska, 2000, U.S. Geological Survey Professional Paper 1662, p. 19–43.

Connon, R.F., Quinton, W.L., Craig, J.R., and Hayashi, M., 2014, Changing hydrologic connectivity due to permafrost thaw in the lower Liard River valley, NWT, Canada: Hydrological Processes, v. 28, p. 4163–4178, doi: 10.1002/hyp.10206.

Crossman, J., Futter, M.N., and Whitehead, P.G., 2013, The significance of shifts in precipitation patterns: modelling the impacts of climate change and glacier retreat on extreme flood events in Denali National Park, Alaska.: PloS one, v. 8, p. 18, doi: 10.1371/journal.pone.0074054.

Crozier, M., 2013, Mass-Movement Hazards and Risks: Treatise on Geomorphology, v. 7, p. 249–258, doi: 10.1016/B978-0-12-374739-6.00175-5.

Cruden, D.M., and Varnes, D.J., 1996, Landslide Types and Processes, *in* Turner, A.K. and Schuster, R.L. eds., Landslides: Investigation and Mitigation, p. 77.

Csejtey, B., Cox, D.P., Evarts, R.C., Stricker, G.D., and Foster, H.L., 1982, The Cenozoic Denali Fault System and the Cretaceous accretionary development of southern Alaska: Journal of

Geophysical Research: Solid Earth (1978–2012), v. 87, p. 3741–3754, doi: 10.1029/JB087iB05p03741.

Csejtey, B., Mullen, M.W., Cox, D.P., and Stricker, G.D., 1992, Geology and geochronology of the Healy Quadrangle, south-central Alaska:, http://pubs.er.usgs.gov/publication/i1961.

Cutter, S.L., Boruff, B.J., and Shirley, W.L., 2003, Social vulnerability to environmental hazards: Social Science Quarterly, v. 84, p. 242–261, doi: 10.1111/1540-6237.8402002.

Cutter, S.L., and Finch, C., 2008, Temporal and spatial changes in social vulnerability to natural hazards: Proceedings of the National Academy of Sciences of the United States of America, v. 105, p. 2301–6, doi: 10.1073/pnas.0710375105.

Daanen, R.P., Grosse, G., Darrow, M.M., Hamilton, T.D., and Jones, B.M., 2012, Rapid movement of frozen debris-lobes: Implications for permafrost degradation and slope instability in the south-central Brooks Range, Alaska: Natural Hazards and Earth System Science, v. 12, p. 1521–1537, doi: 10.5194/nhess-12-1521-2012.

Decker, J.E., 1975, Geology of the Mt. Galen area, Mt. McKinley National Park, Alaska: University of Alaska, 77 p.

Deline, P., Gruber, S., Delaloye, R., Fischer, L., Geertsema, M., Giardino, M., Hasler, A., Kirkbride, M., Krautblatter, M., Magnin, F., McColl, S., Ravanel, L., and Schoeneich, P., 2015, Ice Loss and Slope Stability in High-Mountain Regions, *in* Shroder, J.F., Haeberli, W., and Whiteman, C. eds., Snow and Ice-Related Hazards, Risks, and Disasters, Academic Press, p. 521–561.

Denali National Park and Preserve Weather and Climate: National Park Service, https://www.nps.gov/dena/learn/nature/climate.htm (accessed December 2018).

Detienne, M., Delmelle, P., Guevara, A., Samaniego, P., Opfergelt, S., and Mothes, P.A., 2017,

Contrasting origin of two clay-rich debris flows at Cayambe Volcanic Complex, Ecuador: Bulletin of Volcanology, v. 79, doi: 10.1007/s00445-017-1111-2.

Dhakal, A.S., and Sidle, R.C., 2004, Distributed simulations of landslides for different rainfall conditions: Hydrological Processes, v. 18, p. 757–776, doi: 10.1002/hyp.1365.

Dietrich, W.E., and Dorn, R., 1984, Significance of Thick Deposits of Colluvium on Hillslopes: A Case Study Involving the Use of Pollen Analysis in the Coastal Mountains of Northern California: The Journal of Geology, v. 92, p. 147–158, doi: 10.1086/628845.

Dobinski, W., 2011, Permafrost: Earth-Science Reviews, v. 108, p. 158–169, doi: 10.1016/j.earscirev.2011.06.007.

Draebing, D., Haberkorn, A., Krautblatter, M., Kenner, R., and Phillips, M., 2017, Thermal and Mechanical Responses Resulting From Spatial and Temporal Snow Cover Variability in Permafrost Rock Slopes, Steintaelli, Swiss Alps: Permafrost and Periglacial Processes, v. 28, p. 140–157, doi: 10.1002/ppp.1921.

Draebing, D., Krautblatter, M., and Dikau, R., 2014, Interaction of thermal and mechanical processes in steep permafrost rock walls: A conceptual approach: Geomorphology, v. 226, p. 226–235, doi: 10.1016/j.geomorph.2014.08.009.

Dugan, H.A., Lamoureux, S.F., Lewis, T., and Lafrenière, M.J., 2012, The Impact of Permafrost Disturbances and Sediment Loading on the Limnological Characteristics of Two High Arctic Lakes: Permafrost and Periglacial Processes, v. 23, p. 119–126, doi: 10.1002/ppp.1735.

Dumoulin, J.A., Jones, J. V., Box, S.E., Bradley, D.C., Ayuso, R.A., and O'Sullivan, P., 2018, The Mystic subterrane (partly) demystified: New data from the Farewell terrane and adjacent rocks, interior Alaska: Geosphere, v. 14, p. 1501–1543, doi: 10.1130/ges01588.1.

Dusel-Bacon, C., Csejtey, B., Foster, H.L., Doyle, E. 0, Nokleberg, W.J., and Plafker, G., 1993, Distribution, Facies, Ages, and Proposed Tectonic Associations of Regionally Metamorphosed Rocks in East-and South-Central Alaska: USGS Professional Paper 1497-C, p. 73.

Eisbacher, G.H., and Clague, J.J., 1984, Destructive Mass Movements in High Mountains: Hazard and Management: Geological Survey of Canada Paper 84-16, p. 1–230.

Elango, L., and Kannan, R., 2007, Rock-water interaction and its control on chemical composition of groundwater, *in* Sarkar, D., Datta, R., and Hannigan, R. eds., Developments in Environmental Science, v. 5, p. 229–243, doi: 10.1016/S1474-8177(07)05011-5.

Esper Angillieri, M.Y., and Perucca, L.P., 2015, A large and active debris-rockslide in the Central Andes of Argentina (30.26°S): Morphometry and triggering mechanisms: Quaternary International, v. 374, p. 182–188, doi: 10.1016/j.quaint.2014.12.019.

ESRI Curvature Function: ArcGIS for Desktop, http://desktop.arcgis.com/en/arcmap/10.3/manage-data/raster-and-images/curvature-function.htm (accessed January 2019).

Evans, S.G., and Clague, J.J., 1994, Recent climatic change and catastrophic geomorphic processes in mountain environments: Geomorphology, v. 10, p. 107–128, doi: 10.1016/0169-555X(94)90011-6.

Farbrot, H., Isaksen, K., Etzelmüller, B., and Gisnås, K., 2013, Ground Thermal Regime and Permafrost Distribution under a Changing Climate in Northern Norway: Permafrost and Periglacial Processes, v. 24, p. 20–38, doi: 10.1002/ppp.1763.

Ferrero, A.M., Godio, A., Migliazza, M., Sambuelli, L., Segalini, A., and Theodule, A., 2014, Geotechnical and geophysical characterization of frozen granular material, *in* Shan, W.,

Guo, Y., Wang, F., Marui, H., and Strom, A. eds., Landslides in Cold Regions in the Context of Climate Change, Springer International, p. 205–218.

Fischer, L., Huggel, C., Kääb, A., and Haeberli, W., 2013, Slope failures and erosion rates on a glacierized high-mountain face under climatic changes: Earth Surface Processes and Landforms, v. 38, p. 836–846, doi: 10.1002/esp.3355.

Fisher, J.P., Estop-Aragones, C., Thierry, A., Charman, D.J., Wolfe, S.A., Hartley, I.P., Murton, J.B., Williams, M., and Phoenix, G.K., 2016, The influence of vegetation and soil characteristics on active-layer thickness of permafrost soils in boreal forest: Global Change Biology, v. 22, p. 3127–3140, doi: 10.1111/gcb.13248.

Fitzgerald, P.G., Stump, E., Redfield, T.F., Fitzgerald, P.G., Stump, E., and Redfield, T.F., 1993, Late Cenozoic Uplift of Denali and Its Relation to Relative Plate Motion and Fault Morphology: Science, v. 259, p. 497–499.

Francis, J.A., Vavrus, S.J., and Cohen, J., 2017, Amplified Arctic warming and mid-latitude weather: new perspectives on emerging connections: Wiley Interdisciplinary Reviews: Climate Change, v. 8, p. 1–11, doi: 10.1002/wcc.474.

Frothingham, M.G., and Capps, D.M., 2018, The effects of geological structure and clay on landslides in the Teklanika Formation, Denali National Park and Preserve, AK: NPS Geoscientists-in-the Parks Report,.

Fryer, G.J., Watts, P., and Pratson, L.F., 2004, Source of the great tsunami of 1 April 1946: A landslide in the upper Aleutian forearc: Marine Geology, v. 203, p. 201–218, doi: 10.1016/S0025-3227(03)00305-0.

Gariano, S.L., and Guzzetti, F., 2016, Landslides in a changing climate: Earth-Science Reviews, v. 162, p. 227–252, doi: 10.1016/j.earscirev.2016.08.011.

Geertsema, M., 2012, Initial observations of the 11 June 2012 rock/ice avalanche, Lituya Mountain, Alaska, *in* The First Meeting of Cold Region Landslides Network, Harbin, China, p. 5, doi: 10.13140/2.1.2473.5682.

Geertsema, M., Clague, J.J., Schwab, J.W., and Evans, S.G., 2006, An overview of recent large catastrophic landslides in northern British Columbia, Canada: Engineering Geology, v. 83, p. 120–143, doi: 10.1016/j.enggeo.2005.06.028.

Gilbert, W.G., 1979, A Geologic Guide To Mount McKinley National Park: Anchorage, AK, Alaska Natural History Association, 52 p.

Gilbert, W.G., Ferrell, V.M., and Turner, D.L., 1976, The Teklanika Formation: a new Paleocene volcanic formation in the central Alaska Range: v. Alaska Div, p. 16, http://dggs.alaska.gov/webpubs/dggs/gr/text/gr047.pdf.

Gisnås, K., Etzelmüller, B., Lussana, C., Hjort, J., Sannel, A.B.K., Isaksen, K., Westermann, S., Kuhry, P., Christiansen, H.H., Frampton, A., and Åkerman, J., 2017, Permafrost Map for Norway, Sweden and Finland: Permafrost and Periglacial Processes, v. 28, p. 359–378, doi: 10.1002/ppp.1922.

Godt, J.W., and Coe, J.A., 2007, Alpine debris flows triggered by a 28 July 1999 thunderstorm in the central Front Range, Colorado: Geomorphology, v. 84, p. 80–97, doi: 10.1016/j.geomorph.2006.07.009.

Gonzalez, P., Wang, F., Notaro, M., Vimont, D.J., and Williams, J.W., 2018, Disproportionate magnitude of climate change in United States national parks: Environmental Research Letters, v. 13, p. 104001, doi: 10.1088/1748-9326/aade09.

Goode, J.R., Luce, C.H., and Buffington, J.M., 2012, Enhanced sediment delivery in a changing climate in semi-arid mountain basins: Implications for water resource management and

aquatic habitat in the northern Rocky Mountains: Geomorphology, v. 139–140, p. 1–15, doi: 10.1016/j.geomorph.2011.06.021.

Gooseff, M.N., Balser, A., Bowden, W.B., and Jones, J.B., 2009, Effects of hillslope thermokarst in Northern Alaska: Eos, v. 90, p. 29–30, doi: 10.1029/2009EO040001.

Griffiths, D. V., Huang, J., and Fenton, G.A., 2011, Probabilistic infinite slope analysis: Computers and Geotechnics, v. 38, p. 577–584, doi: 10.1016/j.compgeo.2011.03.006.

Grimsley, K.J., Rathburn, S.L., Friedman, J.M., and Mangano, J.F., 2016, Debris Flow Occurrence and Sediment Persistence, Upper Colorado River Valley, CO: Environmental Management, doi: 10.1007/s00267-016-0695-1.

Gruber, S., and Haeberli, W., 2007, Permafrost in steep bedrock slopes and its temperatures-related destabilization following climate change: Journal of Geophysical Research: Earth Surface, v. 112, p. 1–10, doi: 10.1029/2006JF000547.

Gruber, S., Hoelzle, M., and Haeberli, W., 2004, Permafrost thaw and destabilization of Alpine rock walls in the hot summer of 2003: Geophysical Research Letters, v. 31, p. 1–4, doi: 10.1029/2004GL020051.

Guo, Y., Shan, W., Jiang, H., Sun, Y., and Zhang, C., 2014, The impact of freeze-thaw on the stability of soil cut slope in high-latitude frozen regions, *in* Shan, W., Guo, Y., Wang, F., Marui, H., and Strom, A. eds., Landslides in Cold Regions in the Context of Climate Change, Springer International, p. 85–98.

Haeberli, W., Wegmann, M., and Vonder Mühll, D., 1997, Slope stability problems related to glacier shrinkage and permafrost degradation in the Alps: Eclogae Geoligicae Helvetiae, v. 90, p. 407–414.

Haeussler, P.J., Matmon, A., Schwartz, D.P., and Seitz, G.G., 2017, Neotectonics of interior

Alaska and the late Quaternary slip rate along the Denali fault system: Geosphere, v. 13, p. 1445–1463, doi: 10.1130/GES01447.1.

Hales, T.C., and Roering, J.J., 2007, Climatic controls on frost cracking and implications for the evolution of bedrock landscapes: Journal of Geophysical Research: Earth Surface, v. 112, p. 1–14, doi: 10.1029/2006JF000616.

Harris, C., Arenson, L.U., Christiansen, H.H., Etzelmüller, B., Frauenfelder, R., Gruber, S., Haeberli, W., Hauck, C., Hölzle, M., Humlum, O., Isaksen, K., Kääb, A., A, K.-L.M., Lehning, M., et al., 2009, Permafrost and climate in Europe: monitoring and modelling thermal, geomorphological and geotechnical responses: Earth Science Reviews, v. 92, p. 117–171.

Harris, C., and Lewkowicz, A.G., 2000, An analysis of the stability of thawing slopes, Ellesmere Island, Nunavut, Canada: Canadian Geotechnical Journal, v. 37, p. 449–462, doi: 10.1139/t99-118.

Hartigan, J.A., and Hartigan, P.M., 1985, The Dip Test of Unimodality: Annals of Statistics, v. 13, p. 70–84.

Hasler, A., Gruber, S., and Beutel, J., 2012, Kinematics of steep bedrock permafrost: Journal of Geophysical Research: Earth Surface, v. 117, p. 1–17, doi: 10.1029/2011JF001981.

Hatanaka, K., Mitani, Y., Okeke, A., Kuwanda, Y., and Wang, F., 2014, Investigation and mechanism clarification of the 2011.1.5 Atom-en landslide in Kashima area, Matsue City, *in* Shan, W., Guo, Y., Wang, F., Marui, H., and Strom, A. eds., Landslides in Cold Regions in the Context of Climate Change, Springer International, p. 53–69.

Hickman, R.G., Kirk Sherwood, C.W., and Craddock, C., 1990, STRUCTURAL EVOLUTION OF THE EARLY TERTIARY CANTWELL BASIN, SOUTH CENTRAL ALASKA:

Tectonics, v. 9, p. 1433–1449.

Higman, B., Shugar, D.H., Stark, C.P., Ekström, G., Koppes, M.N., Lynett, P., Dufresne, A., Haeussler, P.J., Geertsema, M., Gulick, S., Mattox, A., Venditti, J.G., Walton, M.A.L., McCall, N., et al., 2018, The 2015 landslide and tsunami in Taan Fiord, Alaska: Scientific Reports, v. 8, p. 1–12, doi: 10.1038/s41598-018-30475-w.

Higuera, P.E., Chipman, M.L., Barnes, J.L., Urban, M.A., and Hu, F.S., 2011, Variability of tundra fire regimes in Arctic Alaska: Millennial-scale patterns and ecological implications: Ecological Applications, v. 21, p. 3211–3226, doi: 10.1890/11-0387.1.

Hilton, R.G., Galy, A., and Hovius, N., 2008, Riverine particulate organic carbon from an active mountain belt: Importance of landslides: Global Biogeochemical Cycles, v. 22, p. 1–12, doi: 10.1029/2006GB002905.

Hong, E., Perkins, R., and Trainor, S., 2014, Thaw Settlement Hazard of Permafrost Related to Climate Warming in Alaska: Arctic, v. 67, p. 93–103.

Hu, F.S., Higuera, P.E., Walsh, J.E., Chapman, W.L., Duffy, P.A., Brubaker, L.B., and Chipman, M.L., 2010, Tundra burning in Alaska: Linkages to climatic change and sea ice retreat: Journal of Geophysical Research: Biogeosciences, v. 115, p. 1–8, doi: 10.1029/2009JG001270.

Huggel, C., 2009, Recent extreme slope failures in glacial environments: effects of thermal perturbation: Quaternary Science Reviews, v. 28, p. 1119–1130, doi: 10.1016/j.quascirev.2008.06.007.

Huggel, C., Clague, J.J., and Korup, O., 2012, Is climate change responsible for changing landslide activity in high mountains? Earth Surface Processes and Landforms, v. 37, p. 77–91, doi: 10.1002/esp.2223.

Huggel, C., Gruber, S., and Korup, O., 2013, Landslide Hazards and Climate Change in High Mountains: Elsevier Ltd., v. 13, 288-301 p., doi: 10.1016/B978-0-12-374739-6.00367-5.

Huggel, C., Salzmann, N., Allen, S., Caplan-Auerbach, J., Fischer, L., Haeberli, W., Larsen, C., Schneider, D., and Wessels, R., 2010, Recent and future warm extreme events and high-mountain slope stability: Philosophical Transactions of the Royal Society A: Mathematical, Physical and Engineering Sciences, v. 368, p. 2435–2459, doi: 10.1098/rsta.2010.0078.

Hungr, O., Leroueil, S., and Picarelli, L., 2014, The Varnes classification of landslide types, an update: Landslides, v. 11, p. 167–194, doi: 10.1007/s10346-013-0436-y.

Huscroft, C. a, Lipovsky, P.S., and Bond, J.D., 2004, Permafrost and landslide activity: Case studies from southwestern Yukon Territory: Yukon Exploration and Geology 2003, p. 107–119.

Ikari, M.J., and Kopf, A.J., 2011, Cohesive strength of clay-rich sediment: Geophysical Research Letters, doi: 10.1029/2011GL047918.

Intergovermental Panel on Climate Change (IPCC), 2013, Climate change 2013: The Physical Science Basis: The Physical Science Basis. Contribution of Working Group I to the Fifth Assessment Report of the Intergovernmental Panel on Climate Change,.

Intergovermental Panel on Climate Change (IPCC), 2014, Climate Change 2014: Synthesis Report: 2-26 p., doi: 10.1017/CBO9781107415324.

Isobe, H., and Torii, M., 2016, Swellable clay minerals in weathering products of volcanic sediments related to landslides, *in* American Geophysical Union 2016 fall meeting. San Francisco, CA, United States,.

Iverson, R.M., George, D.L., Allstadt, K., Reid, M.E., Collins, B.D., Vallance, J.W., Schilling, S.P., Godt, J.W., Cannon, C.M., Magirl, C.S., Baum, R.L., Coe, J.A., Schulz, W.H., and

Bower, J.B., 2015, Landslide mobility and hazards: Implications of the 2014 Oso disaster: Earth and Planetary Science Letters, v. 412, p. 197–208, doi: 10.1016/j.epsl.2014.12.020.

Iverson, R.M., Reid, M.E., and Lahusen, R.G., 1997, Debris-Flow Mobilization From Landslides: Annual Review of Earth Planetary Sciences, v. 25, p. 85–138.

Iverson, R.M., Reid, M.E., Logan, M., LaHusen, R.G., Godt, J.W., and Griswold, J.P., 2011, Positive feedback and momentum growth during debris-flow entrainment of wet bed sediment: Nature Geoscience, v. 4, p. 116–121, doi: 10.1038/ngeo1040.

Jin, H., Li, S., Cheng, G., Shaoling, W., and Li, X., 2000, Permafrost and climatic change in China: Global and Planetary Change, v. 26, p. 387–404, doi: 10.1016/S0921-8181(00)00051-5.

Jones, B.M., Grosse, G., Arp, C.D., Miller, E., Liu, L., Hayes, D.J., and Larsen, C.F., 2015, Recent Arctic tundra fire initiates widespread thermokarst development: Nature Publishing Group, p. 1–13, doi: 10.1038/srep15865.

Kääb, A., 2008, Remote sensing of permafrost-related problems and hazards: Permafrost and Periglacial Processes, v. 19, p. 107–136, doi: 10.1002/ppp.

Kargel, J.S., Leonard, G.J., Shugar, D.H., Haritashya, U.K., Bevington, A., Fielding, E.J., Fujita, K., Geertsema, M., Miles, E.S., Steiner, J., Anderson, E., Bajracharya, S., Bawden, G.W., Breashears, D.F., et al., 2016, Geomorphic and geologic controls of geohazards induced by Nepal's 2015 Gorkha earthquake: Science, v. 351, doi: 10.1126/science.aac8353.

Keiler, M., Knight, J., and Harrison, S., 2010, Climate change and geomorphological hazards in the eastern European Alps: Philosophical Transactions of the Royal Society A: Mathematical, Physical and Engineering Sciences, v. 368, p. 2461–2479, doi: 10.1098/rsta.2010.0047.

Khak, V.A., and Kozyreva, E.A., 2012, Changes of geological environment due to the anthropogenic impacts: a case study of south of East Siberia, Russia: Zeitschrift für Geomorphologie, v. 56, p. 183–199, doi: 10.1127/0372-8854/2011/0064.

Kharin, V. V., Zwiers, F.W., Zhang, X., and Wehner, M., 2013, Changes in temperature and precipitation extremes in the CMIP5 ensemble: Climatic Change, v. 119, p. 345–357, doi: 10.1007/s10584-013-0705-8.

Khomutov, A., and Leibman, M.O., 2014, Assessment of landslide hazards in a typical tundra of Central Yamal, Russia, *in* Shan, W., Guo, Y., Wang, F., Marui, H., and Strom, A. eds., Landslides in Cold Regions in the Context of Climate Change, Springer International.

Klaar, M.J., Kidd, C., Malone, E., Bartlett, R., Pinay, G., Chapin, F.S., and Milner, A.M., 2014, Vegetation succession in deglaciated landscapes: implications for sediment and landscape stability: Earth Surface Processes and Landforms, v. 40, p. 1088–1100, file:///Users/annettepatton/Downloads/Klaar_et_al-2015-Earth_Surface_Processes_and_Landforms.pdf (accessed September 2015).

Koch, J., Clague, J.J., and Blais-Stevens, A., 2014, Debris flow chronology and potential hazard along the Alaska highway in Southwest Yukon territory: Environmental and Engineering Geoscience, v. 20, p. 25–43, doi: 10.2113/gseegeosci.20.1.25.

Koch, J.C., Runkel, R.L., Striegl, R., and McKnight, D.M., 2013, Hydrologic controls on the transport and cycling of carbon and nitrogen in a boreal catchment underlain by continuous permafrost: Journal of Geophysical Research: Biogeosciences, v. 118, p. 698–712, doi: 10.1002/jgrg.20058.

Koehler, R.D., Reger, R.D., Spangler, E.R., and Gould, A.I., 2015, INVESTIGATION OF POTENTIALLY ACTIVE TECTONIC FAULTS ALONG THE ROUTE OF THE

PROPOSED ALASKA STAND ALONE PIPELINE, LIVENGOOD TO COOK INLET, ALASKA: Alaska Division of Geological & Geophysical Surveys Report of Investigation 2015-4, p. 78.

Krautblatter, M., Funk, D., and Günzel, F.K., 2013, Why permafrost rocks become unstable: A rock-ice-mechanical model in time and space: Earth Surface Processes and Landforms, v. 38, p. 876–887, doi: 10.1002/esp.3374.

Lafrenière, M.J., and Lamoureux, S.F., 2013, Thermal perturbation and rainfall runoff have greater impact on seasonal solute loads than physical disturbance of the active layer: Permafrost and Periglacial Processes, v. 24, p. 241–251, doi: 10.1002/ppp.1784.

Lague, D., Brodu, N., and Leroux, J., 2013, Accurate 3D comparison of complex topography with terrestrial laser scanner: Application to the Rangitikei canyon (N-Z): ISPRS Journal of Photogrammetry and Remote Sensing, v. 82, p. 10–26, doi: 10.1016/j.isprsjprs.2013.04.009.

Lane, S.N., Bakker, M., Gabbud, C., Micheletti, N., and Saugy, J.N., 2016, Sediment export, transient landscape response and catchment-scale connectivity following rapid climate warming and Alpine glacier recession: Geomorphology, v. 277, p. 210–227, doi: 10.1016/j.geomorph.2016.02.015.

Lara, M.J., Chipman, M.L., and Hu, F.S., 2019, Automated detection of thermoerosion in permafrost ecosystems using temporally dense Landsat image stacks: Remote Sensing of Environment, v. 221, p. 462–473, doi: 10.1016/j.rse.2018.11.034.

Leibman, M.O., 1995, Cryogenic landslides on the Yamal Peninsula, Russia: Preliminary observations: Permafrost and Periglacial Processes, v. 6, p. 259–264, doi: 10.1002/ppp.3430060307.

Leibman, M.O., Khomutov, A., and Kizyakov, A., 2014, Cryogenic landslides in the West-

Siberian Plain of Russia: Classification, mechanisms, and landforms, *in* Shan, W., Guo, Y., Wang, F., Marui, H., and Strom, A. eds., Landslides in Cold Regions in the Context of Climate Change, Springer International, p. 143–162.

Lewkowicz, A.G., 2007, Dynamics of Active-Layer Detachment Failures, Fosheim Peninsula, Ellesmere Island, Nunavut, Canada: Permafrost and Periglacial Processes, v. 18, p. 89–103, doi: 10.1002/ppp.578 Dynamics.

Lewkowicz, A.G., and Harris, C., 2005a, Frequency and magnitude of active-layer detachment failures in discontinuous and continuous permafrost, northern Canada: Permafrost and Periglacial Processes, v. 16, p. 115–130, doi: 10.1002/ppp.522.

Lewkowicz, A.G., and Harris, C., 2005b, Morphology and geotechnique of active-layer detachment failures in discontinuous and continuous permafrost, northern Canada: Geomorphology, v. 69, p. 275–297, doi: 10.1016/j.geomorph.2005.01.011.

Li, T., Li, P., and Wang, H., 2014, Forming mechanism of landslides in the seasonal frozen loess region in China, *in* Shan, W., Guo, Y., Wang, F., Marui, H., and Strom, A. eds., Landslides in Cold Regions in the Context of Climate Change, Springer International, p. 41–51.

Li, G., West, J.A., Densmore, A.L., Hammond, D.E., Jin, Z., Zhang, F., Wang, J., and Hilton, R.G., 2016, Journal of Geophysical Research : Earth Surface the 2008 Wenchuan earthquake: Journal of Geophysical Research: Earth Surface, v. 121, p. 703–724, doi: 10.1002/2015JF003718.

Li, T., Xing, X., and Li, P., 2015, The landslides induced by the released inclusion water of the frozen soil in the side of the Heifangtai Loess Platform, Gansu Province, China, *in* Lollino, G., Manconi, A., Clague, J., Shan, W., and Chiarle, M. eds., Engineering Geology for Society and Territory - Volume 1: Climate Change and Engineering Geology, v. 1, p. 1–

572, doi: 10.1007/978-3-319-09300-0.

Lipovsky, P.S., Evans, S.G., Clague, J.J., Hopkinson, C., Couture, R., Bobrowsky, P., Ekström, G., Demuth, M.N., Delaney, K.B., Roberts, N.J., Clarke, G., and Schaeffer, A., 2008, The July 2007 rock and ice avalanches at Mount Steele, St. Elias Mountains, Yukon, Canada: Landslides, v. 5, p. 445–455, doi: 10.1007/s10346-008-0133-4.

Lu, N., and Godt, J., 2008, Infinite slope stability under steady unsaturated seepage conditions: Water Resources Research, v. 44, p. 1–13, doi: 10.1029/2008WR006976.

Magnin, F., Deline, P., Ravanel, L., Noetzli, J., and Pogliotti, P., 2015, Thermal characteristics of permafrost in the steep alpine rock walls of the Aiguille du Midi (Mont Blanc Massif, 3842 m a.s.l): The Cryosphere, v. 9, p. 109–121, doi: 10.5194/tc-9-109-2015.

Marston, R.A., 2010, Geomorphology and vegetation on hillslopes: Interactions, dependencies, and feedback loops: Geomorphology, v. 116, p. 206–217, doi: 10.1016/j.geomorph.2009.09.028.

Masson-Delmotte, V., Kageyama, M., Braconnot, P., Charbit, S., Krinner, G., Ritz, C., Guilyardi, E., Jouzel, J., Abe-Ouchi, A., Crucifix, M., Gladstone, R.M., Hewitt, C.D., Kitoh, A., LeGrande, A.N., et al., 2006, Past and future polar amplification of climate change: Climate model intercomparisons and ice-core constraints: Climate Dynamics, v. 26, p. 513–529, doi: 10.1007/s00382-005-0081-9.

Matthews, J.A., Winkler, S., Wilson, P., Tomkins, M.D., Dortch, J.M., Richard, W., Hill, J.L., Owen, G., and Vater, A.E., 2018, Small rock-slope failures conditioned by Holocene permafrost degradation: a new approach and conceptual model based on Schmidt-hammer exposure-age dating , Jotunheimen, southern Norway: Boreas, v. 47, p. 1144–1169, doi: 10.1111/bor.12336.

McColl, S.T., 2012, Paraglacial rock-slope stability: Geomorphology, v. 153–154, p. 1–16, doi: 10.1016/j.geomorph.2012.02.015.

McGuire, A.D., Macdonald, R.W., Schuur, E.A.G., Harden, J.W., Kuhry, P., Hayes, D.J., Christensen, T.R., and Heimann, M., 2010, The carbon budget of the northern cryosphere region: Current Opinion in Environmental Sustainability, v. 2, p. 231–236, doi: 10.1016/j.cosust.2010.05.003.

Milledge, D.G., Bellugi, D., Densmore, A.L., and Dietrich, W.E., 2014, A multidimensional stability model for predicting shallow landslide size and shape across landscapes: Journal of Geophysical Research : Earth Surface, v. 119, p. 2481–2504, doi: 10.1002/2014JF003135.

Moreiras, S.M., 2017, Coupled slope collapse—Cryogenic processes in deglaciated valleys of the Aconcagua Region, Central Andes, *in* Mikoš, M., Vilímek, V., Yin, Y., and Sassa, K. eds., Advancing Culture of Living with Landslides, v. 5, p. 1–557, doi: 10.1007/978-3-319-53483-1.

Nauta, A.L., Elberling, B., Petrov, R.E., Li, B., Heijmans, M.M.P.D., Limpens, J., van Huissteden, J., Blok, D., Gallagher, A., Maximov, T.C., and Berendse, F., 2014, Permafrost collapse after shrub removal shifts tundra ecosystem to a methane source: Nature Climate Change, v. 5, p. 67–70, doi: 10.1038/nclimate2446.

Nokleberg, W.J., Plafker, G., and Wilson, F.H., 1994, Geology of south-central Alaska, *in* Plafker, G. and Berg, H.C. eds., The Geology of Alaska, Geological Society of America, p. 311–366.

Nyman, P., Sheridan, G.J., and Lane, P.N.J., 2013, Hydro-geomorphic response models for burned areas and their applications in land management: Progress in Physical Geography, v. 37, p. 787–812, doi: 10.1177/0309133313508802.

Oliva, M., and Ruiz-Fernández, J., 2015, Coupling patterns between para-glacial and permafrost degradation responses in Antarctica: Earth Surface Processes and Landforms, v. 40, p. 1227–1238, doi: 10.1002/esp.3716.

Orlowsky, B., and Seneviratne, S.I., 2012, Global changes in extreme events: Regional and seasonal dimension: Climatic Change, v. 110, p. 669–696, doi: 10.1007/s10584-011-0122-9.

Osterkamp, T.E., Jorgenson, M.T., Schuur, E.A.G., Shur, Y.L., Kanevskiy, M.Z., Vogel, J.G., and Tumskoy, V.E., 2009, Physical and ecological changes associated with warming permafrost and thermokarst in interior Alaska: Permafrost and Periglacial Processes, v. 20, p. 235–256, doi: 10.1002/ppp.

Panda, S., Marchenko, S., and Romanovsky, V., 2014, High-Resolution Permafrost Modeling in Denali National Park and Preserve: Natural Resource Technical Report, Geophysical Institute, University of Alaska Fairbanks, p. 44.

Parker, R.N., Hales, T.C., Mudd, S.M., Grieve, S.W.D., and Constantine, J.A., 2016, Colluvium supply in humid regions limits the frequency of storm-triggered landslides: Scientific Reports, v. 6, p. 34438, doi: 10.1038/srep34438.

Pastick, N.J., Jorgenson, M.T., Wylie, B.K., Nield, S.J., Johnson, K.D., and Finley, A.O., 2015, Distribution of near-surface permafrost in Alaska: Estimates of present and future conditions: Remote Sensing of Environment, v. 168, p. 301–315, doi: 10.1016/j.rse.2015.07.019.

Patton, A.I., Rathburn, S.L., Bilderback, E., and Lukens, C.E., 2018, Patterns of debris flow initiation and periglacial sediment sourcing in the Colorado Front Range: Earth Surface Processes and Landforms, v. 43, p. 2998–3008, doi: https://doi.org/10.1002/esp.4463.

Patton, A.I., Rathburn, S.L., and Capps, D.M., 2019, Landslide response to climate change in permafrost regions: Geomorphology, v. 340, p. 116–128.

Patton, A. I., Rathburn, S. L., Capps, D. M., Brown, R. A., In Revision, Lithologic, geomorphic, and permafrost controls on landsliding in Denali National Park, Alaska, *Geosphere*.

Pautler, B.G., Simpson, J., Mcnally, D.J., and Lamoureux, S.F., 2010, Arctic Permafrost Active Layer Detachments Stimulate Microbial Activity and Degradation of Soil Organic Matter: Environmental Science & Technology, v. 44, p. 4076–4082.

Pavlova, I., Jomelli, V., Brunstein, D., Grancher, D., Martin, E., and Déqué, M., 2014, Debris flow activity related to recent climate conditions in the French Alps: A regional investigation: Geomorphology, v. 219, p. 248–259, doi: 10.1016/j.geomorph.2014.04.025.

Plafker, G., Nokleberg, W.J., and Lull, J.S., 1989, Bedrock geology and tectonic evolution of the Wrangellia, Peninsular, and Chugach Terranes along the Trans-Alaska Crustal Transect in the Chugach Mountains and Southern Copper River Basin, Alaska: Journal of Geophysical Research: Solid Earth, doi: 10.1029/JB094iB04p04255.

Qin, Y., Tan, K., Yang, H., and Li, F., 2016, The albedo of crushed-rock layers and its implication to cool roadbeds in permafrost regions: Cold Regions Science and Technology, v. 128, p. 32–37, doi: 10.1016/j.coldregions.2016.05.004.

Rabassa, J., 2010, Impact of Global Climate Change on Glaciers and Permafrost of South America, with Emphasis on Patagonia, Tierra del Fuego, and the Antarctic Peninsula, *in* Developments in Earth Surface Processes, Elsevier, v. 13, p. 415–438, doi: 10.1016/S0928-2025(08)10019-0.

Racine, C., Jandt, R., Meyers, C., and Dennis, J., 2004, Tundra fire and vegetation change along a hillslope on the Seward Peninsula, Alaska: Arctic, Antarctic, and Alpine Research, v. 36,

p. 1–10, doi: 10.1657/1523-0430.

Ravanel, L., Magnin, F., and Deline, P., 2017, Impacts of the 2003 and 2015 summer heatwaves on permafrost-affected rock-walls in the Mont Blanc massif: Science of the Total Environment, v. 609, p. 132–143, doi: 10.1016/j.scitotenv.2017.07.055.

Redfield, T.F., and Fitzgerald, P.G., 1993, Denali Fault System of southern Alaska: An interior strike-slip structure responding to dextral and sinistral shear coupling: Tectonics, v. 12, p. 1195–1208, doi: 10.1029/93TC00674.

Ridgway, K.D., Trop, J.M., and Jones, D.E., 1999, PETROLOGY AND PROVENANCE OF THE NEOGENE USIBELLI GROUP AND NENANA GRAVEL: IMPLICATIONS FOR THE DENUDATION mSTORY OF THE CENTRAL ALASKA RANGE: Journal of Sedimentary Research, v. 69, p. 1262–1275.

Ridgway, K.D., Trop, J.M., Nokleberg, W.J., Davidson, C.M., and Eastham, K.R., 2002, Mesozoic and Cenozoic tectonics of the eastern and central Alaska Range: Progressive basin development and deformation in a suture zone: Bulletin of the Geological Society of America, v. 114, p. 1480–1504.

Rist, A., 2008, Hydrothermal Processes within the Active Layer above Alpine Permafrost in Steep Scree Slopes and their Influence on Slope Stability: University of Zurich, 199 p.

Rist, A., and Phillips, M., 2005, First results of investigations on hydrothermal processes within the active layer above alpine permafrost in steep terrain: Norsk Geografisk Tidsskrift, v. 59, p. 177–183, doi: 10.1080/00291950510020574.

Rocha, A. V., Loranty, M.M., Higuera, P.E., MacK, M.C., Hu, F.S., Jones, B.M., Breen, A.L., Rastetter, E.B., Goetz, S.J., and Shaver, G.R., 2012, The footprint of Alaskan tundra fires during the past half-century: Implications for surface properties and radiative forcing:

Environmental Research Letters, v. 7, doi: 10.1088/1748-9326/7/4/044039.

Roering, J.J., Mackey, B.H., Handwerger, A.L., Booth, A.M., Schmidt, D.A., Bennett, G.L., and Cerovski-Darriau, C., 2015, Beyond the angle of repose: A review and synthesis of landslide processes in response to rapid uplift, Eel River, Northern California: Geomorphology, v. 236, p. 109–131, doi: 10.1016/j.geomorph.2015.02.013.

Romanovsky, V.E., Smith, S.L., and Christiansen, H.H., 2010, Permafrost Thermal State in the Polar Northern Hemisphere during the International Polar Year 2007–2009: a Synthesis: Permafrost and, v. 21, p. 106–116, doi: 10.1002/ppp.689.

Rowland, J.C., Travis, B.J., and Wilson, C.J., 2011, The role of advective heat transport in talik development beneath lakes and ponds in discontinuous permafrost: Geophysical Research Letters, v. 38, p. 1–5, doi: 10.1029/2011GL048497.

Rupp, S., and Loya, W., 2008, Projected climate change scenarios for Denali Naitonal Park & Preserve:

Schuster, R.L., and Highland, L.M., 2007, Overview of the Effects of Mass Wasting on the Natural Environment: Environmental and Engineering Geoscience, v. 13, p. 25–44, doi: 10.2113/gseegeosci.13.1.25.

Schuur, E. a G., Bockheim, J., Canadell, J.P., Euskirchen, E., Field, C.B., Goryachkin, S. V, Kuhry, P., Lafleur, P.M., Lee, H., Mazhitova, G., Nelson, F.E., Rinke, a, Romanovsky, V.E., Shiklomanov, N., et al., 2008, Vulnerability of permafrost carbon to climate change: Implications for the global carbon cycle: BioScience, v. 58, p. 701–714, doi: 10.1641/B580807.

Schuur, E.A.G., Vogel, J.G., Crummer, K.G., Lee, H., Sickman, J.O., and Osterkamp, T.E., 2009, The effect of permafrost thaw on old carbon release and net carbon exchange from

tundra: Nature, v. 459, p. 556–559.

Screen, J.A., Deser, C., and Simmonds, I., 2012, Local and remote controls on observed Arctic warming: Geophysical Research Letters, v. 39, p. 1–5, doi: 10.1029/2012GL051598.

Shan, W., Guo, Y., Wang, F., Marui, H., and Strom, A. (Eds.), 2014, Landslides in Cold Regions in the Context of Climate Change: 310 p.

Shan, W., Guo, Y., Zhang, C., Hu, Z., Jiang, H., and Wang, C., 2014, Climate-Change Impacts on Embankments and Slope Stability in Permafrost Regions of Bei'an-Heihe Highway, *in* Sassa, K., Canuti, P., and Yin, Y. eds., Landslide Science for a Safer Geoenvironment, Springer International, p. 155–160.

Shan, W., Hu, Z., Guo, Y., Zhang, C., Wang, C., Jiang, H., and Liu, Y., 2015, The impact of climate change on landslides in southeastern of high-latitude permafrost regions of China: Frontiers in Earth Science, v. 3, p. 1–11, doi: 10.3389/feart.2015.00007.

Sidle, R.C., and Bogaard, T.A., 2016, Dynamic earth system and ecological controls of rainfall-initiated landslides: Earth-Science Reviews, v. 159, p. 275–291, doi: 10.1016/j.earscirev.2016.05.013.

Skripnuk, D., and Ulitin, V. V., 2016, Technical and economic substantiation of permafrost thermal stabilization technology under global warming conditions: Materials Physics and Mechanics, v. 26, p. 85–88.

Slater, A.G., and Lawrence, D.M., 2013, Diagnosing Present and Future Permafrost from Climate Models: Journal of Climate, v. 26, p. 5608–5623, doi: 10.1175/JCLI-D-12-00341.1.

van der Sluijs, J., Kokelj, S. V., Fraser, R.H., Tunnicliffe, J., and Lacelle, D., 2018, Permafrost terrain dynamics and infrastructure impacts revealed by UAV photogrammetry and thermal imaging: Remote Sensing, v. 10, p. 1–30, doi: 10.3390/rs10111734.

Snyder, C.W., 2016, Evolution of global temperature over the past two million years: Nature, v. 538, p. 226–228, doi: 10.1038/nature19798.

Soldati, M., Corsini, A., and Pasuto, A., 2004, Landslides and climate change in the Italian Dolomites since the Late glacial: Catena, v. 55, p. 141–161, doi: 10.1016/S0341-8162(03)00113-9.

Stock, J.D., and Dietrich, W.E., 2006, Erosion of steepland valleys by debris flows: Bulletin of the Geological Society of America, v. 118, p. 1125–1148, doi: 10.1130/B25902.1.

Stoffel, M., and Huggel, C., 2012, Effects of climate change on mass movements in mountain environments: Progress in Physical Geography, v. 36, p. 421–439, doi: 10.1177/0309133312441010.

Stoffel, M., Tiranti, D., and Huggel, C., 2014, Climate change impacts on mass movements - Case studies from the European Alps: Science of the Total Environment, v. 493, p. 1255–1266, doi: 10.1016/j.scitotenv.2014.02.102.

Swanson, F.J., and Dyrness, C.T., 1975, Impact of clear-cutting and road construction on soil erosion by landslides in the western Cascade Range, Oregon: Geology, v. 3, p. 393–396.

Swanston, D.N., and Swanson, F.J., 1976, Timber harvesting, mass erosion and steepland forest geomorphology in the Pacific Northwest, *in* Coats, D.R. ed., Geomorphology and Engineering, p. 199–221.

Tarnocai, C., Canadell, J.G., Schuur, E.A.G., Kuhry, P., Mazhitova, G., and Zimov, S., 2009, Soil organic carbon pools in the northern circumpolar permafrost region: Global Biogeochemical Cycles, v. 23, p. 1–11, doi: 10.1029/2008GB003327.

Torrence, K.J., 2014, Chemistry, Sensitivity and Quick-Clay Landslide Amelioration, *in* L'Heureux, J.-S., Locat, A., Leroueil, S., Demers, D., and Locat, J. eds., Landslides in

Sensitive Clays, p. 15–24.

Varnes, D.J., 1978, Slope Movement Types and Processes: Landslides, v. 176, p. 11–33, doi: In Special report 176: Landslides: Analysis and Control, Transportation Research Board, Washington, D.C.

Velde, B., and Meunier, A., 2008, The Origin of Clay Minerals in Soils and Weathered Rocks: Berlin, Germany, Springer-Verlag, 406 p.

Vinson, T.S., Thrall, F.G., and Pfeiffer, T.J., 1999, Mitigation options to reduce thaw instability hazard at the Denali Park Mile Post 45 Landslide, *in* Cold Regions Engineering: Putting Research into Practice, Proceedings of the 10th International Conference, Lincoln, New Hampshire, p. 267–278.

Wahrhaftig, C., Turner, D.L., Weber, F.R., and Smith, T.E., 1975, Nature and timing of movement on hines creek strand of denali fault system, alaska: Geology, v. 3, p. 463–466.

Walvoord, M.A., and Kurylyk, B.L., 2016a, Hydrologic Impacts of Thawing Permafrost—A Review: Vadose Zone Journal, v. 15, p. 0, doi: 10.2136/vzj2016.01.0010.

Walvoord, M.A., and Kurylyk, B.L., 2016b, Hydrologic impacts of thawing permafrost - a review: Vadose Zone Journal, v. 15, p. 1–20, doi: 10.2136/vzj2016.01.0010.

Wang, C., Shan, W., Guo, Y., Hu, Z., and Jiang, H., 2015, Permafrost Distribution Research Based on Remote Sensing Technology in Northwest Section of Lesser Khingan Range in China, *in* Lollino, G., Manconi, A., Clague, J., Shan, W., and Chiarle, M. eds., Engineering Geology for Society and Territory: Climate Change and Engineering Geology, Institute of Cold Regions Science and Engineering, v. 1, p. 285–290, doi: 10.1007/978-3-319-09300-0.

Wang, H., Xing, X., Li, T., Qin, Z., and Yang, J., 2014, Slope instability phenomenon in the permafrost region along the Qinghai–Tibetan Highway, China, *in* Shan, W., Guo, Y., Wang,

F., Marui, H., and Strom, A. eds., Landslides in Cold Regions in the Context of Climate Change, Springer International, p. 11–23, doi: 10.1007/978-3-319-00867-7.

Wei, Z., Jin, H.J., Zhang, J.M., Yu, S.P., Han, X.J., Ji, Y.J., He, R.X., and Chang, X.L., 2011, Prediction of permafrost changes in Northeastern China under a changing climate: Science China Earth Sciences, v. 54, p. 924–935, doi: 10.1007/s11430-010-4109-6.

Wemple, B.C., Swanson, F.J., and Jones, J.A., 2001, Forest roads and geomoprhic process interactions, Cascade Range, Oregon: Earth Surface Processes and Landforms, v. 26, p. 191–204.

Westermann, S., Peter, M., Langer, M., Schwamborn, G., Schirrmeister, L., Etzelmüller, B., and Boike, J., 2017, Transient modeling of the ground thermal conditions using satellite data in the Lena River delta, Siberia: The Cryosphere, v. 11, p. 1441–1463.

Westermann, S., Schuler, T. V., Gisnås, K., and Etzelmüller, B., 2013, Transient thermal modeling of permafrost conditions in Southern Norway: The Cryosphere, v. 7, p. 719–739, doi: 10.5194/tc-7-719-2013.

Wheaton, J.M., Brasington, J., Darby, S.E., and Sear, D.A., 2010, Accounting for uncertainty in DEMs from repeat topographic surveys: Improved sediment budgets: Earth Surface Processes and Landforms, v. 35, p. 136–156, doi: 10.1002/esp.1886.

Wilson, F.H., Hults, C.P., Mull, C.G., and Karl, S.M., 2015, Geologic Map of Alaska: USGS Scientific Investigations Map 3340, pamphlet, scale 1:1,584,000, p. 197, 2 sheets.

Yamazaki, Y., Kubota, J., Ohata, T., Vuglinsky, V., and Mizuyama, T., 2006, Seasonal changes in runoff characteristics on a permafrost watershed in the southern mountainous region of eastern Siberia: Hydrological Processes, v. 20, p. 453–467, doi: 10.1002/hyp.5914.

Yeend, W., 1997, Reconnaisance Geologic Map of Surficial Deposits of the Mount McKinley

Quadrangle, Alaska: USGS Open-File Report OF-97-138 scale 1:250,000, p. 1.

Zhao, S., Zhang, S., Cheng, W., and Zhou, C., 2019, Model Simulation and Prediction of Decadal Mountain Permafrost Distribution Based on Remote Sensing Data in the Qilian Mountains from the 1990s to the 2040s: Remote Sensing, v. 11, p. 1–19, doi: 10.3390/rs11020183.

Zimmerman, M., and Haeberli, W., 1992, Climatic change and debris flow activity in high-mountain areas: a case study in the Swiss Alps: Catena Supplement, v. 22, p. 59–72.

Zwieback, S., Kokelj, S., Günther, F., Boike, J., Grosse, G., and Hajnsek, I., 2018, Sub-seasonal thaw slump mass wasting is not consistently energy limited at the landscape scale: Cryosphere, v. 12, p. 549–564, doi: 10.5194/tc-12-549-2018.

Zwieback, S., Westermann, S., Langer, M., Boike, J., Marsh, P., and Berg, A., 2019, Improving Permafrost Modeling by Assimilating Remotely Sensed Soil Moisture: Water Resources Research, v. 55, p. 1814–1832, doi: 10.1029/2018WR023247.

APPENDIX A: LANDSLIDE INVENTORY

Table A1. Landslide inventory data, including coordinates of the initiation site and slope characteristics of the landslides evaluated in Chapter 3. The unit column indicates the underlying geologic unit as described in Table 3.1. Slope characteristics include area (m^2); slope angle (°); slope aspect (°), planform hillslope curvature (unitless); active layer thickness/seasonal frost thickness (m), where positive values indicate active layer thickness and negative values indicate seasonal frost depth; and mean decadal ground temperature (°C).

ID	Latitude	Longitude	Unit	Area	Slope	Aspect	Elev	Curv	ALT	MDGT
1	63.4264638	-150.37297	Tmg	66324	29.4	187.6	1017	-1.136	1.03	-0.22
2	63.4276846	-150.36471	Tmg	1771	28.5	184.0	1046	0.124	1.03	-0.19
3	63.4283314	-150.35251	TRn	307	30.4	104.9	1076	0.782	1.02	-0.21
4	63.4278189	-150.37392	Tmg	15089	17.5	253.9	1065	-0.182	1.03	-0.23
5	63.4305168	-150.35177	Tmga	4161	18.9	192.7	1171	-0.315	-0.73	0.36
6	63.4306558	-150.35254	Tmga	10215	27.5	195.8	1172	-0.011	-0.72	0.36
7	63.4312067	-150.34316	TRn	22689	29.7	311.5	1239	-1.494	-0.72	0.36
8	63.4314599	-150.29479	Qgo	3407	12.0	162.4	1129	-0.119	-0.74	0.36
9	63.4346853	-150.31416	TRn	446	33.3	182.9	1260	0.698	-0.63	0.64
10	63.4383493	-150.28355	Qcol	962	20.0	148.4	1242	0.016	-0.64	0.71
11	63.440717	-150.27207	Qcol	464	9.0	135.1	1190	0.339	-0.70	0.51
12	63.4422691	-150.26787	Qcol	1455	16.0	163.6	1194	0.357	-0.70	0.51
13	63.4433033	-150.26631	Qcol	3002	19.7	125.8	1208	0.045	-0.70	0.51
14	63.4528373	-150.22501	TRn	1100	24.8	307.2	1194	0.409	0.94	-0.51
15	63.456009	-150.23216	Qgm	681	14.8	226.1	1147	0.273	1.57	-0.28
16	63.4574033	-150.22761	Qgm	298	11.4	316.4	1186	-0.792	1.50	-0.41
17	63.4582022	-150.22953	Qgm	2365	18.1	306.1	1152	-0.014	1.57	-0.28
18	63.458561	-150.22652	Qgm	2011	21.2	299.0	1180	-0.616	1.51	-0.40
19	63.4589053	-150.22497	Qgm	3506	14.7	270.4	1194	-0.504	1.51	-0.40
20	63.4604931	-150.22244	Qgm	319	16.3	315.1	1196	-0.068	0.90	-0.99
22	63.4601391	-150.21782	Qgm	2010	12.7	11.7	1211	0.172	1.44	-0.55
23	63.4608931	-150.21384	Qgm	1104	14.8	29.7	1182	-0.637	0.90	-0.99
24	63.4607885	-150.215	Qgm	827	16.5	10.0	1190	-0.450	1.44	-0.56
25	63.4628625	-150.22041	Qgm	1494	10.3	116.5	1182	0.141	0.90	-1.00
26	63.4675617	-150.22042	TRn	6374	35.7	42.2	1254	-0.803	0.86	-0.72
27	63.4829808	-150.11635	Qmw	3242	15.1	279.8	1113	0.047	0.98	-0.30
28	63.4847649	-150.11385	Qmw	198	18.9	318.2	1110	1.010	1.00	-0.34
29	63.4858862	-150.12187	Qg	1812	12.6	137.0	1163	-0.480	0.97	-0.43
30	63.4863497	-150.1211	Qg	289	20.6	31.1	1156	-1.254	0.97	-0.43
31	63.4863515	-150.11925	Qg	436	23.7	72.8	1133	1.584	0.97	-0.43

ID	Latitude	Longitude	Unit	Area	Slope	Aspect	Elev	Curv	ALT	MDGT
32	63.4866622	-150.12383	Qg	3861	12.6	78.0	1186	1.512	0.97	-0.43
34	63.4877433	-150.11608	Qmw	1344	18.2	163.8	1129	1.029	1.00	-0.34
35	63.4876557	-150.12412	Qg	456	15.1	84.9	1169	0.534	0.97	-0.44
36	63.4879368	-150.11502	Qmw	995	13.4	82.6	1121	-0.037	1.00	-0.35
38	63.4883002	-150.1222	Qal	374	3.4	111.8	1154	-0.105	0.97	-0.44
39	63.489233	-150.11578	Qmw	8178	18.2	264.1	1144	1.235	1.00	-0.35
40	63.4902614	-150.11291	Qmw	1772	13.8	351.9	1135	-0.431	1.00	-0.35
41	63.4905782	-150.11204	Qmw	951	24.4	1.0	1127	0.956	1.00	-0.35
42	63.4917933	-150.08749	Qmw	109	27.5	3.0	1058	-0.632	1.01	-0.26
43	63.4916531	-150.08913	Qmw	1790	34.0	300.4	1054	0.584	1.01	-0.26
44	63.4919954	-150.08351	Qmw	2340	26.8	339.3	1079	-0.164	1.00	-0.12
45	63.4921448	-150.0853	Qmw	6603	10.1	319.7	1060	-0.331	1.01	-0.26
46	63.4931741	-150.12218	Qmw	6411	26.2	143.8	1203	0.184	0.97	-0.44
47	63.4937926	-150.08166	Qmw	2203	19.5	7.2	1044	-0.879	1.00	-0.12
48	63.4978643	-150.11146	Qmw	1169	27.8	83.5	1170	-1.052	1.00	-0.36
49	63.4981041	-150.0837	Qg	659	14.7	134.6	1046	0.081	1.02	-0.14
50	63.498128	-150.11648	Qmw	12573	18.5	171.3	1190	-1.260	0.97	-0.44
51	63.4981711	-150.11206	Qmw	391	24.4	25.6	1179	0.216	1.00	-0.36
52	63.4983839	-150.08773	Qg	739	23.2	178.2	1095	0.046	0.97	-0.50
53	63.5120722	-149.96791	Qmw	20129	23.9	131.9	1049	-1.145	1.01	-0.57
54	63.5128914	-149.99357	Qcol	4907	7.4	187.6	974	-0.139	1.01	-0.49
55	63.5132524	-149.97869	Kc	2105	11.3	255.4	1018	-0.022	0.97	-0.60
56	63.5135453	-149.94172	Ttb	2933	2.7	311.5	1084	0.457	0.94	-0.67
57	63.5161041	-150.0047	Qcol	1043	25.3	214.7	972	0.541	1.05	-0.44
58	63.5180648	-150.01288	TRn	2918	39.5	191.0	974	1.019	1.00	-0.15
59	63.5239376	-149.93744	Kc	2920	16.5	151.3	1198	-0.013	1.79	-0.24
60	63.5270287	-149.89955	Qcol	11171	12.5	141.4	1130	-0.656	1.89	-0.01
61	63.535006	-149.84879	Kc	943	30.2	126.6	1227	0.506	0.91	-0.34
62	63.5353102	-149.83034	Ttr	2059	22.0	172.7	1131	-0.009	0.93	-0.24
63	63.5356821	-149.8285	Ttr	4252	10.7	177.2	1132	-1.030	0.95	-0.14
64	63.5370461	-149.81498	Ttr	2690	32.7	200.6	1176	2.984	0.95	-0.14
65	63.538767	-149.81691	Ttr	107723	20.1	227.2	1224	0.829	0.93	-0.19
66	63.5389854	-149.82187	Ttb	4325	37.0	248.2	1141	0.769	0.93	-0.19
67	63.5407119	-149.80515	Ttr	48204	17.8	147.6	1048	0.031	0.91	-0.31
68	63.5503074	-149.73169	Tu	12170	28.0	311.6	1089	1.992	0.91	-0.22
69	63.5531829	-149.80284	Ttr	641	17.8	109.9	1095	0.116	0.97	-0.04
70	63.5535166	-149.80046	Ttr	606	24.0	156.9	1088	-0.368	0.97	-0.05
71	63.5546184	-149.76611	Qgo	803	31.9	5.3	995	0.617	-0.77	0.03
72	63.5546915	-149.7664	Qgo	803	26.7	9.0	993	-0.438	-0.77	0.03

ID	Latitude	Longitude	Unit	Area	Slope	Aspect	Elev	Curv	ALT	MDGT
73	63.5555927	-149.66278	Tta	2896	16.4	160.4	1216	0.074	1.55	-0.51
74	63.5584924	-149.79973	Ttr	6124	38.4	65.0	998	1.027	0.97	-0.04
75	63.5635365	-149.63702	Ttb	71	28.6	285.4	1127	1.265	0.92	-0.20
76	63.5646119	-149.6459	Tta	164	34.3	356.8	1151	1.710	-1.41	0.07
77	63.5647349	-149.64502	Tta	3888	31.1	64.2	1130	-0.262	-1.41	0.07
78	63.5706376	-149.62478	Tta	3142	33.1	248.6	1111	1.345	0.95	-0.09
79	63.5713671	-149.62211	Tta	2633	33.0	265.0	1172	-1.031	0.00	0.00
80	63.5813374	-149.6163	Kc	281	26.8	3.5	1041	-0.324	0.94	-0.19
81	63.5839982	-149.61709	Qcol	578	30.2	279.8	992	0.638	0.99	-0.01
82	63.5854032	-149.6165	Qcol	412	25.5	295.0	989	-1.267	0.99	-0.02
83	63.591776	-149.60522	Qcol	505	28.5	285.4	1085	-0.951	-0.84	0.01
84	63.5953912	-149.60257	Qcol	1278	20.5	324.3	1011	0.043	-0.82	0.05
85	63.5953344	-149.60033	Qcol	9482	31.8	311.2	1058	0.763	-0.84	0.04
88	63.4925812	-150.12643	Qmw	10	21.9	144.9	1222	-1.636	0.97	-0.44
89	63.4639743	-150.20751	Qgm	10	20.6	44.8	1104	-0.292	0.94	-0.85

APPENDIX B: PXRF ANALYSIS OF CLAY MINERALS FROM LANDSLIDES IN DENALI NATIONAL PARK

Thirteen clay samples were collected from mapped landslides where a significant volume of clay material was exposed in the scarp or within the landslide deposit. Clay samples were then dried and analyzed for mineral assemblage and chemical composition using multispectral mineral analyzer and portable X-ray fluorescent analyzer (pXRF). Concentrations of nine representative rock samples of mapped lithologies were also analyzed with the pXRF, including the Nikolai Formation, Teklanika Rhyolite, Teklanika Andesite, Teklanika Basalt, Mount Galen Andesite, and Mount Galen Rhyolite. These samples were assumed to be representative of the lithologic unit over the scale of the map area

For nine clay samples where the parent lithology could be assumed with confidence from field observation, normalized ratios (*Y*) of elemental concentrations were calculated using the formula:

$$Y = \frac{b_i - a_i}{a_i}$$

Where:

b_i = the concentration of element i in one of the nine clay samples and

a_i = the average concentration of element i in the most likely parent unit of that sample

Positive values indicate enrichment of a particular element in a clay sample relative to the concentration in the parent lithology, and negative values indicate a depletion in the clay sample. Elements for which more than three samples contained concentrations below the detection limit

of the pXRF were excluded from this analysis. Where up to three samples contained elemental concentrations below the detectable limit, the unknown value was assumed to be half of the minimum value measured in the sample set. This analysis assumes that regional variability of chemical composition within mapped units is minor, and that the measured chemical composition of rock samples of a given unit is representative of the parent material before alteration. Further, the assumption is made that clay minerals are secondary chemical weathering products of parent materials.

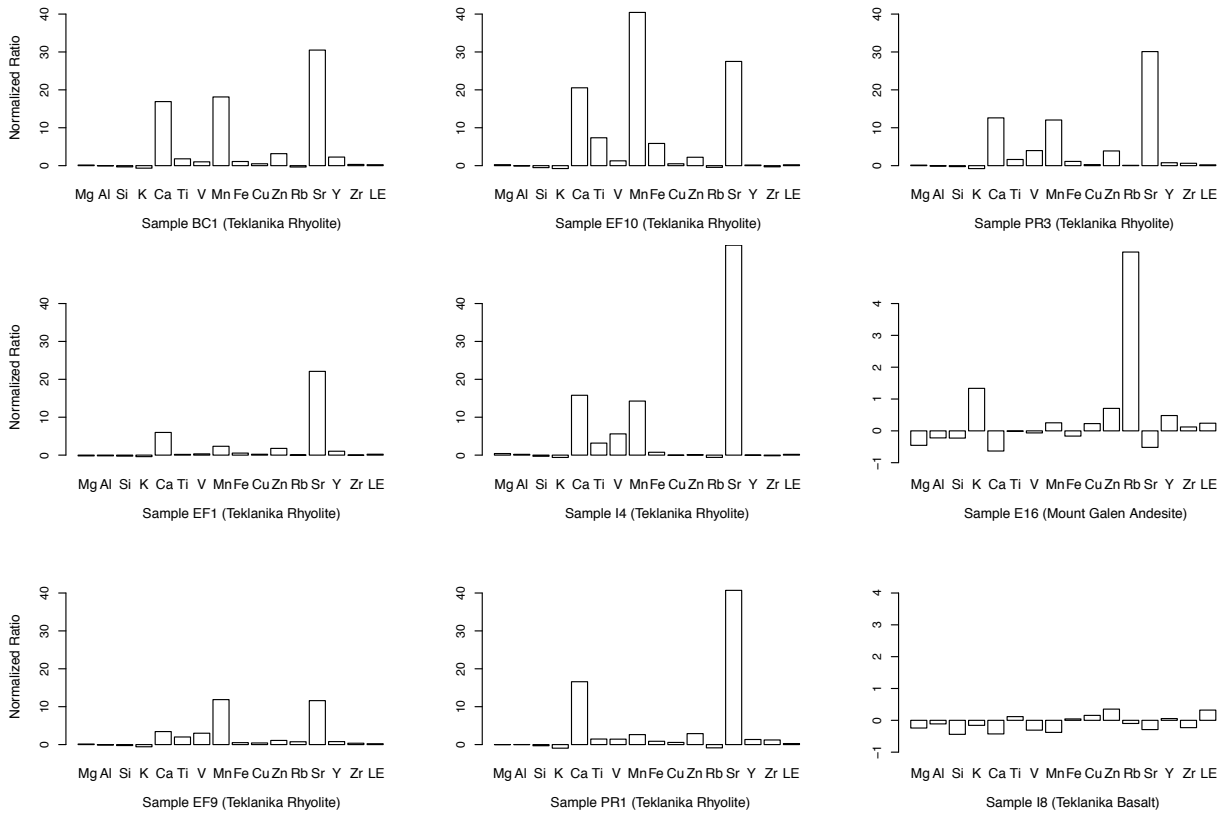

Figure B1. Barplot showing a normalized ratio of elemental concentrations in clay samples relative to their most likely parent unit. Assuming that rock sample chemistry is representative of the parent material, positive values indicate higher concentrations of an element in the clay sample relative to the parent material and negative values indicate lower concentrations in the clay sample. The calculation of the normalized ratio is described above.

Clay samples demonstrate a high degree of alteration relative to their original parent lithology. Relative chemical compositions of clay samples and the parent material indicate retention and/or addition of significant Ca, Sr, and Mn in the rhyolite-derived samples. This relative enrichment of Ca, Sr, and Mn indicates the influence of groundwater in the evolution of clay minerals weathered from rhyolite parent rocks. Ca, Sr, and Mn are readily water soluble (Bourg and Berlin, 1994; Elango and Kannan, 2007; Apollaro et al., 2009; Carling et al., 2015) and high concentrations of these cations can interact with existing clay minerals and influence overall clay composition (Elango and Kannan, 2007). At face value, these comparisons assume that the modern rock samples are representative of the original parent material. However, the rock samples used in this analysis have also undergone weathering processes, either low-temperature metamorphism at shallow depths or weathering at the earth surface.

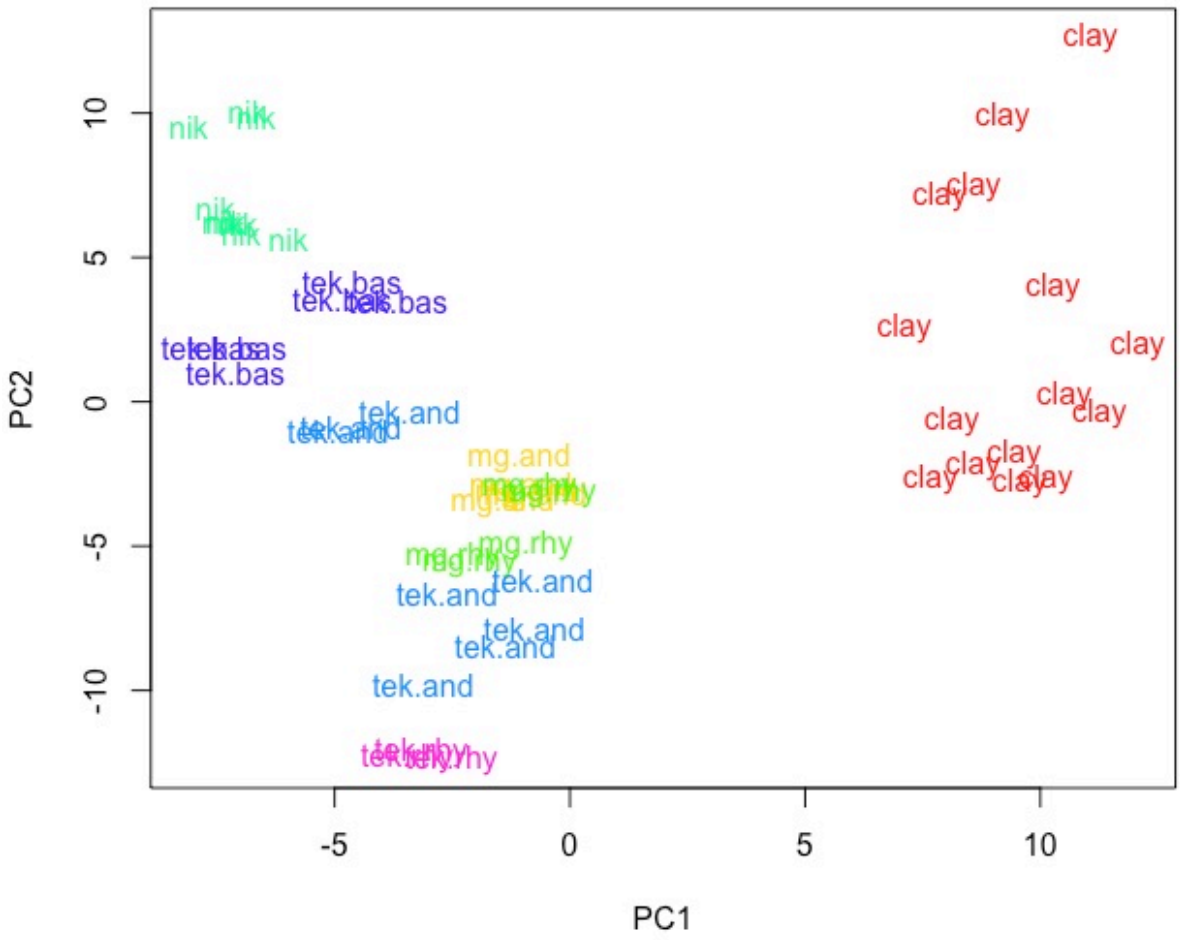

Figure B2. Principal components scores based on pXRF concentrations. PC1 and PC2 separate analyzed samples according to unit.

Table B1. Element concentrations (ppm) and reported error for the 13 clay samples and 9 rock samples. I collected three readings of visually homogenous rock samples and five readings of visually heterogenous rock samples.

Reading	sample	unit	Mg	Mg err	Al	Al err	Si	Si err
2	T3	tek.bas	4.28	0.17	7.77	0.07	24.33	0.1
3	T3	tek.bas	3.96	0.17	7.93	0.07	24.82	0.1
4	T3	tek.bas	3.72	0.16	7.75	0.07	24.64	0.1
5	EF8	tek.rhy	1.21	0.11	6.3	0.06	37.72	0.11
6	EF8	tek.rhy	1.17	0.11	6.38	0.06	37.91	0.11
7	EF8	tek.rhy	1.08	0.1	6.46	0.06	37.67	0.11
8	PC2	tek.and	2.7	0.14	8.92	0.07	28.77	0.1
9	PC2	tek.and	2.49	0.13	8.69	0.07	27.96	0.1
11	PC2	tek.and	2.52	0.14	8.95	0.07	28.61	0.1
12	S1	nik	2.95	0.15	9.6	0.07	23.46	0.09
13	S1	nik	2.77	0.15	10.72	0.08	23.34	0.09
14	S1	nik	2.79	0.15	10.57	0.08	23.13	0.09
15	S1	nik	3.34	0.16	10.36	0.08	22.84	0.09
16	S1	nik	2.44	0.14	11.35	0.08	23.1	0.09
17	E10	nik	8.94	0.22	5.87	0.06	20.54	0.09
18	E10	nik	9.27	0.22	5.76	0.06	20.62	0.09
19	E10	nik	9.35	0.22	5.55	0.06	21.2	0.09
20	E4b	mg.and	2.57	0.13	7.81	0.06	30.62	0.1
21	E4b	mg.and	2.45	0.13	8.74	0.07	30.21	0.1
22	E4b	mg.and	2.98	0.14	7.86	0.06	29.57	0.1
23	E4b	mg.and	2.33	0.13	8.6	0.07	30.77	0.1
24	E4b	mg.and	2.6	0.13	8.02	0.06	30.52	0.1
25	S1	nik	2.93	0.15	9.67	0.07	23.36	0.09
26	E1	mg.rhy	2.06	0.12	7.41	0.06	32.63	0.11
27	E1	mg.rhy	2.13	0.12	7.1	0.06	30.3	0.1
28	E1	mg.rhy	1.73	0.12	7.55	0.06	30.15	0.1
29	E1	mg.rhy	1.93	0.12	7.33	0.06	32.69	0.1
30	E1	mg.rhy	1.73	0.11	7.5	0.06	31.94	0.1
31	I11	tek.and	1.42	0.11	6.9	0.06	35.96	0.11
32	I11	tek.and	1.09	0.11	6.69	0.06	32.4	0.11
33	I11	tek.and	1.28	0.11	7.65	0.06	32.69	0.11
34	I11	tek.and	1.22	0.11	5.97	0.06	34.7	0.11
35	I11	tek.and	1.26	0.11	6.39	0.06	33.84	0.11
36	EF7	tek.bas	1.88	0.13	7.66	0.07	27.26	0.1
37	EF7	tek.bas	1.81	0.13	7.64	0.07	27.41	0.1
38	EF7	tek.bas	1.6	0.13	7.81	0.07	27.9	0.1
39	EF1	clay	0.92	0.12	5.17	0.06	27.93	0.11
40	PR3	clay	1.27	0.12	5.69	0.06	28.28	0.11
41	PR3	clay	1.27	0.12	5.48	0.06	27.77	0.11
42	PR3	clay	1.39	0.13	5.84	0.06	28.87	0.11
43	E16	clay	1.41	0.13	6.39	0.06	23.45	0.1
44	BC1	clay	1.34	0.13	6.09	0.06	25.42	0.1
45	PR1	clay	1.14	0.12	6.42	0.06	26.17	0.1
46	C1	clay	1.52	0.13	6.43	0.06	22.05	0.09
47	EF10	clay	1.45	0.14	5.92	0.06	18.15	0.08
48	EF5	clay	1.69	0.14	6.19	0.06	19.9	0.09
49	I8	clay	2.18	0.16	6.89	0.07	14.59	0.07
50	HP2	clay	1.83	0.14	7.71	0.07	23.9	0.1
51	I4	clay	1.63	0.13	7.7	0.07	26.29	0.1
52	I9	clay	1.61	0.13	8.61	0.07	19.09	0.08
53	EF9	clay	1.32	0.12	5.61	0.06	28.24	0.1

Reading	sample	K	K err	Ca	Ca err	Ti	Ti err	V	V err
2	T3	0.9637	0.0064	4.8044	0.019	1.0597	0.0131	0.0427	0.0046
3	T3	1.0174	0.0066	5.0493	0.0198	1.0588	0.0134	0.0481	0.0047
4	T3	1.1394	0.0069	4.5836	0.0181	1.0063	0.0128	0.0455	0.0046
5	EF8	4.1038	0.0149	0.0493	0.061	0.0846	0.0063	0.0123	0.0246
6	EF8	4.1872	0.0151	0.0493	0.0605	0.0786	0.0063	0.0122	0.0244
7	EF8	4.1839	0.0151	0.0493	0.0584	0.0801	0.0063	0.0121	0.0242
8	PC2	1.0782	0.0068	4.8249	0.0179	0.5065	0.0101	0.0431	0.0042
9	PC2	1.0531	0.0066	4.5814	0.0171	0.5185	0.01	0.043	0.0041
11	PC2	1.0828	0.0068	4.9247	0.0182	0.4876	0.01	0.0452	0.0042
12	S1	0.21515	0.0375	7.9343	0.0285	0.9974	0.013	0.0512	0.0047
13	S1	0.21515	0.0405	8.3398	0.0298	0.7556	0.0118	0.0397	0.0044
14	S1	0.21515	0.0397	8.5748	0.0306	0.7643	0.0118	0.0228	0.0043
15	S1	0.21515	0.0397	8.1709	0.0294	0.7423	0.0114	0.0348	0.0043
16	S1	0.21515	0.0408	8.8311	0.0309	0.5336	0.0103	0.0254	0.004
17	E10	0.21515	0.0444	5.6563	0.0235	0.6662	0.0104	0.0266	0.0038
18	E10	0.21515	0.0458	5.701	0.0237	0.6188	0.0101	0.0262	0.0038
19	E10	0.21515	0.0415	6.8327	0.0278	0.6095	0.0102	0.0235	0.0038
20	E4b	0.5866	0.0054	3.2008	0.0128	0.3897	0.009	0.0446	0.004
21	E4b	0.4303	0.005	3.7612	0.0144	0.3494	0.0089	0.0335	0.0039
22	E4b	0.4629	0.0049	3.3605	0.0133	0.4181	0.0092	0.0387	0.0039
23	E4b	0.5085	0.0053	3.8713	0.0147	0.3866	0.0092	0.0302	0.004
24	E4b	0.5719	0.0054	3.2697	0.0131	0.4159	0.0094	0.0432	0.0041
25	S1	0.21515	0.038	8.1087	0.0288	0.9675	0.0126	0.0389	0.0045
26	E1	1.2699	0.0072	3.1204	0.0123	0.4134	0.0093	0.039	0.004
27	E1	1.2621	0.0069	3.0383	0.012	0.659	0.0108	0.0289	0.0041
28	E1	1.2645	0.007	3.6294	0.0138	0.4482	0.0094	0.0352	0.0039
29	E1	1.384	0.0074	3.1991	0.0124	0.4093	0.0092	0.0318	0.0039
30	E1	1.2635	0.0071	3.1717	0.0124	0.3025	0.0083	0.0332	0.0038
31	I11	3.7879	0.0145	0.3064	0.0062	0.2168	0.0079	0.0426	0.004
32	I11	3.405	0.0133	1.0358	0.0072	0.2099	0.0075	0.0388	0.0037
33	I11	4.1732	0.0158	1.5127	0.0087	0.3729	0.0094	0.0612	0.0045
34	I11	3.0531	0.0123	1.4394	0.0081	0.3212	0.0087	0.0474	0.0041
35	I11	3.521	0.0138	0.9543	0.0072	0.2322	0.0079	0.0444	0.004
36	EF7	1.5851	0.0083	4.0371	0.0159	0.9753	0.0126	0.0536	0.0046
37	EF7	1.5764	0.0083	4.0764	0.0161	0.9754	0.0127	0.0589	0.0047
38	EF7	1.6596	0.0086	4.1242	0.0161	1.0478	0.0132	0.0547	0.0048
39	EF1	2.5075	0.0116	0.3442	0.0052	0.0963	0.0064	0.0162	0.0034
40	PR3	0.883	0.0062	0.6931	0.0056	0.2202	0.0075	0.0587	0.004
41	PR3	0.9892	0.0065	0.6115	0.0054	0.2069	0.0074	0.0603	0.004
42	PR3	0.86	0.0061	0.7078	0.0057	0.2121	0.0075	0.0631	0.0041
43	E16	1.1959	0.0071	1.2814	0.0074	0.385	0.0089	0.0356	0.0039
44	BC1	1.406	0.0079	0.8827	0.0062	0.2271	0.0075	0.0245	0.0036
45	PR1	0.21515	0.0673	0.8672	0.0059	0.1999	0.0072	0.0297	0.0036
46	C1	2.2922	0.0111	0.3592	0.0048	0.5968	0.0101	0.0304	0.0039
47	EF10	0.9884	0.0063	1.0621	0.0065	0.6777	0.0096	0.0277	0.0035
48	EF5	1.1213	0.0069	1.5779	0.0085	0.9721	0.0123	0.026	0.0042
49	I8	1.1148	0.0069	2.5481	0.0125	1.1395	0.0129	0.035	0.0042
50	HP2	2.0712	0.0102	0.0986	0.0046	0.458	0.0091	0.0478	0.0039
51	I4	1.6037	0.0085	0.8278	0.0063	0.3385	0.0088	0.0806	0.0045
52	I9	2.0333	0.0098	3.7525	0.0158	0.7641	0.0114	0.032	0.0042
53	EF9	1.7735	0.0087	0.2186	0.0045	0.2438	0.0075	0.0488	0.0038

Reading	sample	Mn	Mn err	Fe	Fe err	Cu	Cu err	Zn	Zn err
2	T3	0.0651	0.002	8.4804	0.0337	0.0029	0.0004	0.0116	0.0004
3	T3	0.0647	0.0021	8.0476	0.0322	0.0029	0.0004	0.01	0.0003
4	T3	0.0647	0.002	7.8701	0.0313	0.0031	0.0004	0.0114	0.0003
5	EF8	0.0045	0.0011	1.9051	0.0099	0.0019	0.0003	0.0077	0.0003
6	EF8	0.00225	0.2	1.9114	0.0099	0.0016	0.0003	0.0086	0.0003
7	EF8	0.00225	0.2	1.272	0.0077	0.0009	0.0003	0.0102	0.0003
8	PC2	0.1011	0.0024	5.5049	0.0222	0.002	0.0003	0.0071	0.0003
9	PC2	0.1097	0.0024	5.5858	0.0223	0.002	0.0003	0.0075	0.0003
11	PC2	0.1055	0.0024	5.4673	0.0221	0.0012	0.0003	0.0076	0.0003
12	S1	0.0906	0.0023	9.5823	0.0361	0.0304	0.0008	0.0078	0.0003
13	S1	0.0874	0.0023	8.2507	0.0319	0.0205	0.0006	0.0072	0.0003
14	S1	0.0899	0.0024	8.6325	0.0332	0.016	0.0006	0.0068	0.0003
15	S1	0.0906	0.0023	9.2331	0.0351	0.0171	0.0006	0.0073	0.0003
16	S1	0.00225	-0.0016	7.0147	0.0275	0.0149	0.0006	0.0057	0.0003
17	E10	0.1256	0.0026	12.41	0.05	0.0187	0.0007	0.0096	0.0004
18	E10	0.1246	0.0026	11.9534	0.0493	0.0141	0.0006	0.0086	0.0003
19	E10	0.1293	0.0027	11.6267	0.0478	0.0158	0.0007	0.0085	0.0003
20	E4b	0.0554	0.0018	4.0256	0.0172	0.0013	0.0003	0.0066	0.0003
21	E4b	0.0441	0.0017	3.5586	0.0157	0.001	0.0003	0.0064	0.0003
22	E4b	0.0742	0.0021	4.8192	0.0199	0.0013	0.0003	0.0084	0.0003
23	E4b	0.0374	0.0016	3.4057	0.0151	0.0012	0.0003	0.0061	0.0002
24	E4b	0.049	0.0018	4.0001	0.0172	0.0009	0.0003	0.0065	0.0003
25	S1	0.0912	0.0023	9.1427	0.0344	0.0288	0.0007	0.0076	0.0003
26	E1	0.0752	0.0021	3.8858	0.0164	0.00045	0.0046	0.0048	0.0002
27	E1	0.0878	0.0022	4.3422	0.0178	0.00045	0.0044	0.005	0.0002
28	E1	0.0825	0.0021	4.3531	0.0179	0.00045	0.0045	0.0044	0.0002
29	E1	0.0714	0.002	3.5165	0.015	0.0012	0.0003	0.0063	0.0002
30	E1	0.066	0.002	3.3869	0.0147	0.00045	0.0046	0.0035	0.0002
31	I11	0.0179	0.0014	3.0302	0.0138	0.0014	0.0003	0.0142	0.0004
32	I11	0.0364	0.0016	4.1482	0.0172	0.0016	0.0003	0.0159	0.0004
33	I11	0.0246	0.0015	3.401	0.0152	0.0014	0.0003	0.0161	0.0004
34	I11	0.0175	0.0014	2.9635	0.0135	0.0011	0.0003	0.014	0.0003
35	I11	0.0266	0.0015	3.0075	0.0138	0.002	0.0003	0.0136	0.0003
36	EF7	0.1781	0.003	10.5505	0.039	0.0023	0.0004	0.0147	0.0004
37	EF7	0.1915	0.0032	10.9527	0.0405	0.003	0.0004	0.0147	0.0004
38	EF7	0.1541	0.0029	9.8782	0.0367	0.0019	0.0004	0.0148	0.0004
39	EF1	0.01	0.0012	2.6035	0.0133	0.0018	0.0003	0.0245	0.0004
40	PR3	0.0389	0.0016	3.6144	0.0167	0.0017	0.0003	0.0452	0.0006
41	PR3	0.0411	0.0017	3.5085	0.0165	0.0018	0.0003	0.0411	0.0006
42	PR3	0.0374	0.0016	3.6347	0.0169	0.0021	0.0003	0.043	0.0006
43	E16	0.0652	0.0019	3.3118	0.016	0.0014	0.0003	0.0116	0.0003
44	BC1	0.0574	0.0019	3.5531	0.0167	0.0022	0.0003	0.0368	0.0005
45	PR1	0.0109	0.0012	3.1752	0.0152	0.0023	0.0003	0.0344	0.0005
46	C1	0.0329	0.0016	6.0718	0.0266	0.0037	0.0004	0.016	0.0004
47	EF10	0.1243	0.0024	11.63	0.05	0.0022	0.0004	0.0284	0.0005
48	EF5	0.1459	0.0027	8.9872	0.0396	0.0026	0.0004	0.0244	0.0005
49	I8	0.0743	0.0021	9.7052	0.0438	0.0031	0.0004	0.0174	0.0004
50	HP2	0.0604	0.0019	6.3582	0.027	0.0062	0.0004	0.0131	0.0004
51	I4	0.0458	0.0017	2.9743	0.0145	0.0014	0.0003	0.0099	0.0003
52	I9	0.0773	0.0021	5.5282	0.024	0.0022	0.0003	0.0099	0.0003
53	EF9	0.0386	0.0016	2.5594	0.0124	0.0021	0.0003	0.0185	0.0004

Reading	sample	Sr	Sr err	Y	Y err	Zr	Zr err	LE	LE err
2	T3	0.0424	0.0003	0.003	0.0001	0.0278	0.0002	47.78	0.18
3	T3	0.042	0.0003	0.0026	0.0001	0.0282	0.0002	47.6	0.18
4	T3	0.0419	0.0003	0.0034	0.0001	0.0296	0.0002	48.66	0.18
5	EF8	0.0003	0	0.0049	0.0001	0.0314	0.0002	48.59	0.14
6	EF8	0.0004	0	0.0039	0.0001	0.0308	0.0002	48.29	0.14
7	EF8	0.0003	0	0.0026	0.0001	0.0301	0.0002	49.18	0.14
8	PC2	0.0839	0.0004	0.0016	0.0001	0.0127	0.0002	47.28	0.16
9	PC2	0.0807	0.0004	0.0017	0.0001	0.0126	0.0002	48.74	0.16
11	PC2	0.0843	0.0004	0.0013	0.0001	0.0125	0.0002	47.56	0.16
12	S1	0.0239	0.0002	0.0023	0.0001	0.0111	0.0002	45.19	0.17
13	S1	0.0298	0.0002	0.0016	0.0001	0.0084	0.0002	45.61	0.17
14	S1	0.0306	0.0002	0.0017	0.0001	0.008	0.0002	45.33	0.17
15	S1	0.0301	0.0002	0.0016	0.0001	0.0081	0.0002	45.08	0.17
16	S1	0.0379	0.0003	0.001	0.0001	0.0054	0.0001	46.63	0.17
17	E10	0.0251	0.0002	0.0016	0.0001	0.0091	0.0002	45.54	0.2
18	E10	0.0208	0.0002	0.0014	0.0001	0.0085	0.0002	45.72	0.2
19	E10	0.024	0.0002	0.0014	0.0001	0.0086	0.0002	44.47	0.19
20	E4b	0.0536	0.0003	0.0012	0.0001	0.0112	0.0002	50.58	0.16
21	E4b	0.0636	0.0003	0.0011	0.0001	0.0101	0.0002	50.34	0.16
22	E4b	0.0518	0.0003	0.0012	0.0001	0.0109	0.0002	50.28	0.16
23	E4b	0.06	0.0003	0.0009	0.0001	0.0106	0.0002	49.96	0.16
24	E4b	0.0567	0.0003	0.001	0.0001	0.0111	0.0002	50.4	0.16
25	S1	0.0246	0.0002	0.0022	0.0001	0.0105	0.0002	45.54	0.17
26	E1	0.0476	0.0003	0.001	0.0001	0.0081	0.0001	49.03	0.15
27	E1	0.0447	0.0003	0.0009	0.0001	0.0079	0.0001	50.97	0.15
28	E1	0.0456	0.0003	0.0009	0.0001	0.007	0.0001	50.65	0.15
29	E1	0.0471	0.0003	0.0008	0.0001	0.008	0.0001	49.36	0.15
30	E1	0.0495	0.0003	0.0006	0.0001	0.0068	0.0001	50.54	0.15
31	I11	0.0099	0.0001	0.0049	0.0001	0.0538	0.0003	48.2	0.15
32	I11	0.012	0.0001	0.005	0.0001	0.0503	0.0003	50.83	0.15
33	I11	0.0159	0.0001	0.0058	0.0001	0.06	0.0003	48.7	0.15
34	I11	0.0088	0.0001	0.0052	0.0001	0.0501	0.0003	50.16	0.15
35	I11	0.0105	0.0001	0.0054	0.0001	0.0543	0.0003	50.61	0.15
36	EF7	0.0354	0.0003	0.0041	0.0001	0.0288	0.0002	45.34	0.17
37	EF7	0.0357	0.0003	0.0043	0.0001	0.0295	0.0002	44.83	0.18
38	EF7	0.036	0.0003	0.0042	0.0001	0.0298	0.0002	45.29	0.17
39	EF1	0.0077	0.0001	0.0077	0.0001	0.0303	0.0002	60.3	0.16
40	PR3	0.0107	0.0001	0.0067	0.0001	0.0513	0.0003	59.09	0.16
41	PR3	0.01	0.0001	0.0067	0.0001	0.0482	0.0003	59.91	0.16
42	PR3	0.0104	0.0001	0.0068	0.0001	0.0504	0.0003	58.22	0.16
43	E16	0.0275	0.0002	0.0016	0.0001	0.0121	0.0002	62.41	0.16
44	BC1	0.0105	0.0001	0.0124	0.0001	0.0405	0.0003	60.87	0.16
45	PR1	0.0139	0.0001	0.0089	0.0001	0.0682	0.0004	61.81	0.16
46	C1	0.0126	0.0001	0.0057	0.0001	0.0605	0.0003	60.39	0.17
47	EF10	0.0095	0.0001	0.0044	0.0001	0.0212	0.0002	59.79	0.18
48	EF5	0.0213	0.0002	0.0058	0.0001	0.0348	0.0003	59.1	0.18
49	I8	0.0276	0.0002	0.0038	0.0001	0.0223	0.0002	61.57	0.18
50	HP2	0.0105	0.0001	0.0022	0.0001	0.0178	0.0002	57.34	0.17
51	I4	0.0188	0.0002	0.0037	0.0001	0.0256	0.0002	58.43	0.16
52	I9	0.017	0.0002	0.0038	0.0001	0.0279	0.0002	58.38	0.16
53	EF9	0.0042	0.0001	0.0068	0.0001	0.0418	0.0002	59.82	0.15

APPENDIX B REFERENCES

Bourg, A., and Berlin, C., 1994, Seasonal and Spatial Trends in Manganese Solubility in an Alluvial Aquifer: Environmental Science and Technology, v. 28, p. 868-876.

Elango, L., and Kannan, R., 2007, Rock-water interaction and its control on chemical composition of groundwater *in* Developments in Environmental Science, Sarkar, D., Datta, R., Hannigan, R. (Eds.), Academic Press.

Apollaro, C., Accornero, M., Marini, L., Barca, D., De Rosa, D., 2009, The impact of dolomite and plagioclase weathering on the chemistry of shallow groundwaters circulating in a granodiorite-dominated catchment of the Sila Massif (Calabria, Southern Italy): Applied Geochemistry, v. 24, p. 957-979.

Carling et al., 2015, Evaluating natural and anthropogenic trace element inputs along an alpine to urban gradient in the Provo River, Utah, USA: Applied Geochemistry, v. 63, p. 398-412.

APPENDIX C: GROUND-PENETRATING RADAR AT PTARMIGAN ALD

Figure C1. Example radargram and radar transect lines at the Ptarmigan ALD. GPR lines are overlain on a slope map derived from a TLS survey of the landslide conducted in summer 2018.

APPENDIX D: SOIL CARBON CONCENTRATION IN LANDSLIDES

Using soil samples collected in August 2017, I estimated carbon (C) concentration from disturbed and undisturbed soils in Denali National Park. Soils samples were dried and burned using a muffle furnace to calculate Loss on Ignition (LOI). Landslide site names refer to the same sites referenced in Chapter 4, as well as a site near Stony Pass referred to as "Borehole 16."

Table D1. Carbon concentrations estimated using LOI.

sample #	site name	landslide/ undisturbed	wet sample wt (g)	dried sample wt (g)	water lost (g)	% H2O lost	burned wt (g)	C lost (g)	% C lost
BH 16-01-A	Borehole 16	U	51.2498	39.1525	12.1	23.60	36.2978	2.85	7.29
BH 16-01-B	Borehole 16	U	73.1462	58.5767	14.6	19.92	56.1022	2.47	4.22
BH 16-01-C	Borehole 16	U	57.1935	48.1175	9.1	15.87	46.4866	1.63	3.39
BH 16-02-A	Borehole 16	LS	47.2469	42.4281	4.8	10.20	41.3784	1.05	2.47
E-01-A	Eielson	U	57.9554	43.3736	14.6	25.16	40.1258	3.25	7.49
E-01-B	Eielson	U	47.4475	35.9694	11.5	24.19	33.414	2.56	7.10
E-02-A	Eielson	LS	58.3476	51.6166	6.7	11.54	50.4701	1.15	2.22
E-03-A	Eielson	LS	51.2757	41.4248	9.9	19.21	39.2853	2.14	5.16
SP-01-A	Stony Pass Slump	U	51.571	31.7391	19.8	38.46	27.8262	3.91	12.33
SP-01-B	Stony Pass Slump	U	67.8806	54.3944	13.5	19.87	52.3978	2.00	3.67
SP-01-C	Stony Pass Slump	U	71.3763	55.6961	15.7	21.97	53.3767	2.32	4.16
SP-01-D	Stony Pass Slump	U	80.6292	64.831	15.8	19.59	62.5026	2.33	3.59
SP-02-A	Stony Pass Slump	LS	69.5964	54.5001	15.1	21.69	51.7924	2.71	4.97
SP-02-B	Stony Pass Slump	LS	52.4613	38.7924	13.7	26.06	35.7952	3.00	7.73
SP-02-C	Stony Pass Slump	LS	52.7541	37.648	15.1	28.63	33.97	3.68	9.77
PT-01-A	Ptarmigan	U	16.3157	6.0353	10.3	63.01	3.0196	3.02	49.97
PT-01-B	Ptarmigan	U	37.4103	13.301	24.1	64.45	7.7702	5.53	41.58
PT-02-A	Ptarmigan	LS	71.308	58.9545	12.4	17.32	55.9418	3.01	5.11
PT-02-B	Ptarmigan	LS	20.2308	9.0511	11.2	55.26	6.6881	2.36	26.11
PT-02-C	Ptarmigan	LS	66.7094	46.023	20.7	31.01	41.5327	4.49	9.76
PT-03-A	Ptarmigan	LS	65.4872	54.8201	10.7	16.29	51.6706	3.15	5.75
PT-03-B	Ptarmigan	LS	70.5894	52.3418	18.2	25.85	48.5297	3.81	7.28
PT-04-A	Ptarmigan	LS	52.0659	36.0339	16.0	30.79	30.9176	5.12	14.20
PT-04-B	Ptarmigan	LS	36.3959	26.6242	9.8	26.85	23.3687	13.03	48.93